



HAL
open science

Molecular catalysis of CO₂ light-driven reduction with Co complexes in homogeneous and supported conditions

Bing Ma

► **To cite this version:**

Bing Ma. Molecular catalysis of CO₂ light-driven reduction with Co complexes in homogeneous and supported conditions. Other. Université Paris Cité, 2020. English. NNT : 2020UNIP7006 . tel-03154151

HAL Id: tel-03154151

<https://theses.hal.science/tel-03154151>

Submitted on 27 Feb 2021

HAL is a multi-disciplinary open access archive for the deposit and dissemination of scientific research documents, whether they are published or not. The documents may come from teaching and research institutions in France or abroad, or from public or private research centers.

L'archive ouverte pluridisciplinaire **HAL**, est destinée au dépôt et à la diffusion de documents scientifiques de niveau recherche, publiés ou non, émanant des établissements d'enseignement et de recherche français ou étrangers, des laboratoires publics ou privés.



UNIVERSITÉ DE PARIS

LABORATOIRE D'ELECTROCHIMIE MOLECULAIRE

École doctorale 388

Chimie Physique et de Chimie Analytique de Paris Centre

THESE DE DOCTORAT

PRESENTEE PAR **BING MA**

**Catalyse moléculaire de la réduction photochimique du CO₂ à l'aide
de complexes de cobalt en conditions homogène et supportée**

Thèse soutenue publiquement le 4 Décembre 2020 devant le jury composé de :

Rapportrice : Caroline MELLOTT-DRAZNIIEKS, Directrice de Recherche, Collège de France

Rapportrice : Marie-Noëlle COLLOMB, Directrice de Recherche, Université Grenoble-Alpes

Examineur : Junwang TANG, Professeur, University College London

Examineur : Alexander COWAN, Professeur, University of Liverpool

Directeurs de thèse : Julien BONIN, Maître de Conférences, Université de Paris

Marc ROBERT, Professeur, Université de Paris

Résumé

La production photocatalytique de carburants solaires est un moyen efficace de stockage chimique de l'énergie solaire et offre une option potentiellement fructueuse pour parvenir à un système énergétique à zéro émission de carbone. La pierre angulaire d'un processus pratique de production de carburant solaire est de concevoir et d'optimiser des photocatalyseurs stables, efficaces et déployables à grande échelle, et comprenant un matériau semi-conducteur permettant l'absorption de photons, la génération efficace de porteurs de charge, leur transport jusqu'à la réalisation de réactions catalytiques.

La catalyse moléculaire joue un rôle essentiel dans la photosynthèse naturelle et artificielle. Dans ce travail de doctorat, j'ai étudié (i) un complexe bimétallique pour la réduction sélective du CO₂, illustrant le fait que la catalyse moléculaire est l'un des moyens prometteurs pour mettre en oeuvre la coopérativité des métaux avec des activités intrinsèques exceptionnelles ; (ii) des matériaux inorganiques (nitrure de carbone semi-conducteur et acide graphitique) pouvant être fonctionnalisés par une molécule (complexe quaterpyridine de cobalt) par le biais d'une liaison amide covalente. Une hétérogénéisation efficace des deux composants a été réalisée. Ces systèmes hybrides ont montré des performances catalytiques élevées vis-à-vis de la photoréduction au CO₂. Ils illustrent que le développement de catalyseurs moléculaires vaut la peine d'être exploré afin de parvenir à des systèmes catalytiques évolutifs qui sont nécessaires pour la production pratique de carburant solaire à grande échelle. Dans le mécanisme de fonctionnement des catalyseurs moléculaires supportés par des matériaux, des défis subsistent en ce qui concerne à la fois la stabilité de l'unité moléculaire, les techniques d'hétérogénéisation et le contrôle de l'interaction électronique entre les composants.

Mots-clés: réduction du CO₂, catalyse photochimique, catalyse supportée, systèmes hybrides, catalyseur moléculaire bimétallique, complexes de cobalt.

Abstract

Photocatalytic solar fuel production is an effective means of chemical storage for solar energy and it provides a potential fruitful option for achieving a zero-emissions energy system. The cornerstone of a practical solar fuel production process is to design and optimize stable, efficient, and scalable photocatalysts, including a semiconductor material that accommodates photon absorption, efficient charge carriers generation, transport, and then catalytic reactions.

Molecular catalysis plays an essential role in both natural and artificial photosynthesis. In this doctoral work, I have (i) investigated a bimetallic complex for selective CO₂ reduction, illustrating that molecular catalysis is one of the promising way to activate metal cooperativity with outstanding intrinsic activities; (ii) synthesized inorganic material (semiconductive carbon nitride and graphitic acid) able to be functionalized with a molecular molecule (cobalt quaterpyridine) through a covalent amide bond. Effective heterogenization of the two components was thoroughly accessed. These hybrid sstems showed high catalytic performance towards CO₂ photoreduction. They illustrate that the development of molecular catalysts is worth to be explored for the invention of scalable catalytic systems that are needed for large scale, practical solar fuel production. In the mechanism of material-supported molecule catalysts, challenges still remain regarding both to molecular stability, heterogenization techniques, and control of the electronic interaction between these components.

Keywords: CO₂ reduction reaction, photochemical catalysis, supported catalysis, hybrid systems, bimetallic molecular catalysts, cobalt complexes.

Table of contents

Résumé.....	2
Abstract.....	3
Table of contents.....	4
Chapter 1 - Introduction	7
1.1 Development of artificial photosynthesis systems inspired by Nature	7
1.2 Research and development for CO ₂ reduction with molecular catalysts	8
1.2.1 Molecular catalysts	8
1.2.2 Theoretical concepts	10
1.3 Homogeneous photocatalytic systems involving transition-metal-based molecular catalysts for 2-electron CO ₂ reduction	13
1.3.1 Molecular-based photocatalytic system for CO ₂ -to-CO or to-HCOO ⁻ conversion.....	13
1.3.2 Molecular dyads photocatalysts for CO ₂ reduction	24
1.4 CO ₂ photoreduction with bi-metallic catalysts.....	28
1.5 Supported molecules CO ₂ reduction catalysts	30
1.5.1 Hybrid catalysts assembled by non-covalent effect.....	32
1.5.2 Hybrid catalysts assembled by covalent bonds.....	33
1.6 Motivation and outline of the thesis	35
Chapter 2 - Homogeneous photochemical reduction of CO₂ under visible light with dinuclear complexes	37
2.1 Quaterpyridine complexes in homogeneous conditions.....	38
2.2 Quaterpyridine complexes in supported conditions	39
2.3 Selective reduction of CO ₂ -to-CO or to-formate through metal synergy	39
2.3.1 Photocatalytic performance for CO ₂ reduction.....	40
2.3.2 Investigation of Co ₂ biqpy by electrochemistry.....	49
2.3.3 Proposed pathway for CO and formate production	57
2.4 Sub-conclusion and sub-perspectives for bimetallic catalytic system	60

Chapter 3 - Heterogeneous photochemical reduction of CO₂ with covalently bonded molecular catalysts	61
3.1 Photochemical reduction of CO ₂ -to-CO with Coqpy covalently grafted on mesoporous graphic carbon nitride (“Coqpy@mpg-C ₃ N ₄ ”).....	61
3.1.1 Synthesis and characterization of Coqpy@mpg-C ₃ N ₄	61
3.1.2 Catalytic performance for CO ₂ reduction under visible-light.....	69
3.1.3 Investigation of the photoinduced electron transfer mechanism	73
3.1.4 Stability of the catalytic system	78
3.2 Selective reduction of CO ₂ to CO or HCOO ⁻ under visible light with Coqpy covalently grafted on a graphene material (Coqpy@GA).....	83
3.2.1 Synthesis and characterization of Coqpy@GA	83
3.2.2 Characterization of GA and GA-Coqpy	85
3.2.3 Catalytic performance for CO ₂ reduction under visible-light.....	92
3.2.4 Stability of the catalytic system	100
3.2.5 Proposed pathway for CO and formate production	104
3.3 Conclusions and perspectives.....	106
Chapter 4 - New approach towards strong conjugation of molecular catalysts with (semi)conductive support	107
4.1 Electrochemical reduction of CO ₂ through strong electronic coupling of Coqpy to graphitic electrode	107
4.1.1 Synthesis of CoLCl ₂ (L = 2,9-di(pyridin-2-yl)-1,10-phenanthroline-5,6-diamine) 109	
4.1.2 Synthesis of graphite-conjugated-Coqpy (GC-Coqpy).....	112
4.1.3 Characterization of GC-Coqpy electrode.....	113
4.1.4 Cyclic voltammetry characterization of GCC-Coqpy electrode	115
4.2 Perspectives	116
Chapter 5 - General conclusions and perspectives	117
5.1 General conclusions	117
5.2 Future perspectives.....	120
Chapter 6 - Experiments and methods	122
6.1 Chemicals and Synthesis	122
6.1.1 Commercial chemicals.....	122
6.1.2 Synthesis and purifications	123
6.2 Characterization Methods	129

6.2.1	UV-visible spectroscopy	129
6.2.2	Solar simulator	129
6.2.3	Fluorescence spectroscopy.....	130
6.2.4	Transient absorption spectroscopy.....	130
6.2.5	Frontier Infrared (FT-IR) spectroscopy	131
6.2.6	Nuclear magnetic resonance (NMR) spectroscopy.....	131
6.2.7	Gas chromatography (GC) and Gas chromatography-Mass (GC-MS).....	131
6.2.8	Ionic chromatography (IC)	132
6.2.9	pH measurements.....	132
6.2.10	Cyclic voltammetry.....	132
6.2.11	X-ray photoelectron spectroscopy (XPS)	133
6.2.12	Inductively Coupled Plasma - Optical Emission Spectroscopy (ICP-OES). 133	
6.2.13	Photochemical experiments setup.....	133
6.2.14	X-ray powder diffraction (XRD).....	134
6.2.15	Electrochemical and photoelectrochemical measurements	134
6.2.16	Scanning Electron Microscope (SEM)	134
6.2.17	X-ray Absorption Spectroscopy (XAS).....	135
	Notations	136
	Terms and Abbreviations	137
	Acknowledgements.....	139
	Bibliography	140

Chapter 1 - Introduction

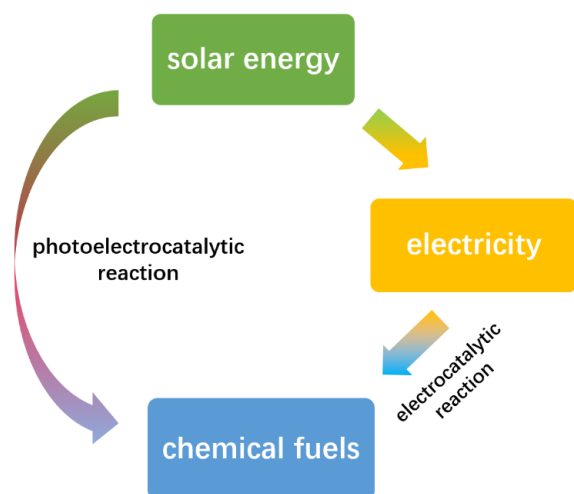
1.1 Development of artificial photosynthesis systems inspired by Nature

With industrial progress and economic development, more than 80% of global energy consumption comes from fossil energy, an source that has insufficient reserves, is unequally available and emits pollutants.¹ This requires us to find clean and renewable alternative resources and corresponding carbon-neutral technologies.

The most abundant renewable energy source available on the planet is solar energy: solar illumination on Earth every hour is greater than the worldwide energy consumption for a whole year.² The intrinsic carrier of solar energy is a photon traveling at light speed. It is only by efficiently collecting these energy carriers, then producing separated electrons-holes (*i.e.* achieving charge separation) to achieve its conversion into “electronic” energy that solar energy can be used on a larger scale.

the most common method to utilize solar energy for generating electricity is through photovoltaic cells in which photogenerated electrons and holes can be collected to produce potential and current, *i.e.* the harvested solar energy is directly converted into electricity. However, electricity cannot readily be stored on a massive scale, is not easy to transport without important lossess and cannot realize a complete replacement of fossil fuels, because the energy density of batteries is far below that of chemical fuels regarding both weight and volume.³ Therefore, electricity is not an ideal energy source for applications such as large oversea vessels and long-distance air transport at present.

Another strategy is to take inspiration from photosynthesis in Nature which can complete the conversion of solar energy to chemical energy in the form of chemical bonds and which can produce energy containing compounds such as carbohydrates. In this way, solar energy can be directly converted into chemical fuels *via* photoelectrocatalytic reactions, or it can be converted into fuels indirectly by using the electricity generated from solar energy to drive electrocatalytic reactions (Scheme 1.1).



Scheme 1.1 Two routes for solar energy-to-chemical fuels conversion.

However, it is impossible and quite unnecessary to completely replicate natural photosynthesis in living organisms, so the concept of artificial photosynthesis (AP), a multi-step reaction process, was suggested.

Specifically, current researches mostly imitate only a part of the photosynthetic reaction, namely water decomposition, CO₂ reduction, nitrogen fixation and oxygen reduction. Generally speaking, artificial photosynthesis mainly includes four steps: photon absorption (possibly through a dedicated agent called photosensitizer); charge separation; electron transfer from the photoabsorber to the catalytic site; and finally catalytic reactions. Light absorber and catalyst are the two most important parts of an artificial photosynthetic system. The former requires light absorption, a long-lived excited state and a high current-carrying ability. The latter requires high catalytic activity and stability. Most reactions involve the transfer of multiple electrons and protons, which slows the reaction kinetics and requires large overpotentials. Thus, it is required that the catalyst can overcome high reaction energy barrier by lowering the overpotential and thus accelerating the reaction.

1.2 Research and development for CO₂ reduction with molecular catalysts

1.2.1 Molecular catalysts

Molecules have attracted wide attention because of their well-defined properties, controllable synthesis, and tunable structures. As a consequence current researches on AP

systems and devices involving molecular catalysts advocate that they indeed are promising candidates in the development of efficient AP systems.⁴

Molecular complexes can work as efficient catalysts because the electronic structure of their metal cores can be precisely tuned by the coordination environments created by the ligands. Thus, a molecular catalyst usually comprises an active metal center and specific ligands which favor controlling the electronic structure of the active site. Thanks to this configuration, molecular catalysts possess several advantages regarding their use in AP:

a. Identifying active site and improving structure

Resolved structures of molecules are essential for studying catalytic activity and unraveling catalytic mechanisms. FT-IR spectroscopy, XRD spectroscopy as well as X-ray crystallography have revealed many molecular catalysts with their active sites and coordination structures. With the help of spectroelectrochemistry, stopped-flow UV-vis spectroscopy, *in situ* NMR spectroscopy, *in situ* IR spectroscopy, *in situ* Raman spectroscopy and *in situ* mass spectrometry, several catalytic mechanisms implying molecular catalysts have been proposed. As a consequence, the electronic structures and steric configuration can be adjusted by ligand modification. All these studies can further contribute to the researches on catalytic mechanisms. Because of the easy-to-identify and adjustable active sites in molecular catalysts, the product selectivity for CO₂-reduction reaction and other reactions can be improved and tuned.

b. Adjustable intrinsic activity

Catalytic performance of catalysts in AP systems can be enhanced either by increasing the number of active sites or by improving the intrinsic activity of each active site.⁵ The increase of active sites density can be achieved through higher loading of catalysts or by designing catalyst structures to expose more active sites per gram (Fig. 1.1). Nevertheless, these two ways are physically limited by the influence of other processes, such as charge and mass transport or catalyst aggregation.⁵ Therefore, a plateau effect is usually obtained in practice with a high loading of molecules. In contrast, the improvement in the intrinsic activity of catalysts boosts the catalytic performance, avoiding transport issues resulting from high loadings. Additionally, the difference between high loadings and low loadings usually is one

to three orders of magnitude, whereas the difference between “good” and “poor” catalysts can reach more than ten orders of magnitude.⁶

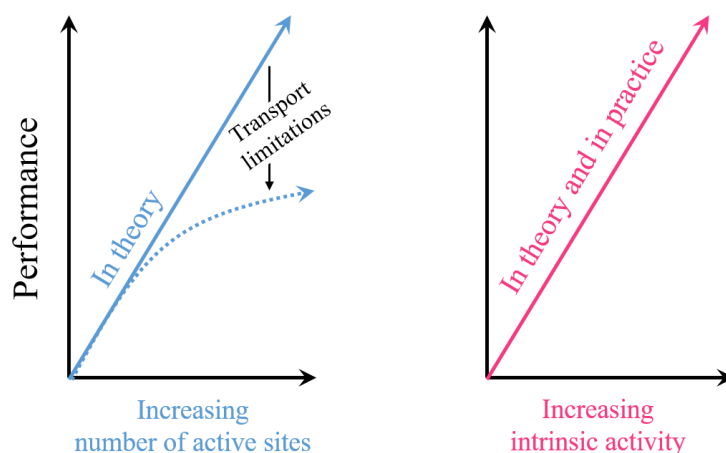


Fig. 1.1 Enhancement of catalytic performance by increasing the number of active sites (left) and/or increasing the intrinsic activity of each active site (right). Adapted with permission from ref. 5. Copyright 2017 American Association for the Advancement of Science (AAAS).

c. Metal-atom economy

From the perspective of practical applications, the efficient use of metal ions is necessary, especially the use of some precious/toxic metals should be avoided as much as possible. Molecular catalysts are undoubtedly more advantageous than inorganic materials. In homogeneous catalysis, most of the metal atoms are theoretically accessible to work as active sites. In contrast, in nanostructures, only metal sites present on the surface, edges, corners, or heterojunctions can successfully catalyze reactions.

After working on large and localized nanostructures, material scientists have started investigating single-atom catalysts.^{7, 8} At the same time, bi-metallic heterogeneous catalysts have also been reported.⁹ The development of catalytic materials and systems is now more and more focused on the molecular level, one major difference between homogeneous and heterogeneous catalysts being that the active site coordination environment is a molecular ligand in the former case and an anchoring matrix in the latter.

1.2.2 Theoretical concepts

a. Molecule-based photocatalytic cycles

Photocatalytic molecular systems for CO₂ reduction comprise three components, *i.e.* a catalyst (CAT), a redox photosensitizer (PS), and a sacrificial electron donor (SD). The metal complex serves as a catalyst capable of accumulating multiple electrons needed to reduce CO₂. Light-driven catalytic routes can be classified as oxidative (Fig. 1.2a) or reductive quenching (Fig. 1.2b.) according to the quenching reaction of the photosensitizer. After excitation (Fig. 1.2a, step (1)), the lowest excited state of the PS (PS*) is a strong reductant and gives an electron to the electron acceptor (EA, being the CAT or an electron mediator). Emission of PS* (Fig. 1.2a, step (2)) is oxidatively quenched to give rise to the corresponding one electron-oxidized form PS⁺ (Fig. 1.2a, step (3)). When the standard redox potential of SD^{•+}/SD is more negative than that of PS⁺/PS, one electron can be donated to PS⁺ (Scheme Fig. 1.2a, step (4)) to recover PS. Alternative possibility involves the reductive quenching of PS* (Fig. 1.2b). In this case, PS* accepts an electron directly from SD (Fig. 1.2b, step (3)). The one-electron-reduced form PS⁻ is thus produced. PS is regenerated through electron transfer from PS⁻ to EA (Fig. 1.2b, step (4)). Favorable conditions for oxidative quenching include long lifetime and high reducing power of PS* as well as high concentration of EA because electron transfer between PS* (PS⁻) and EA is a bimolecular reaction. Quantum yield (QY) and turnover number (TON) are typically employed to evaluate CO₂ reduction efficiency.

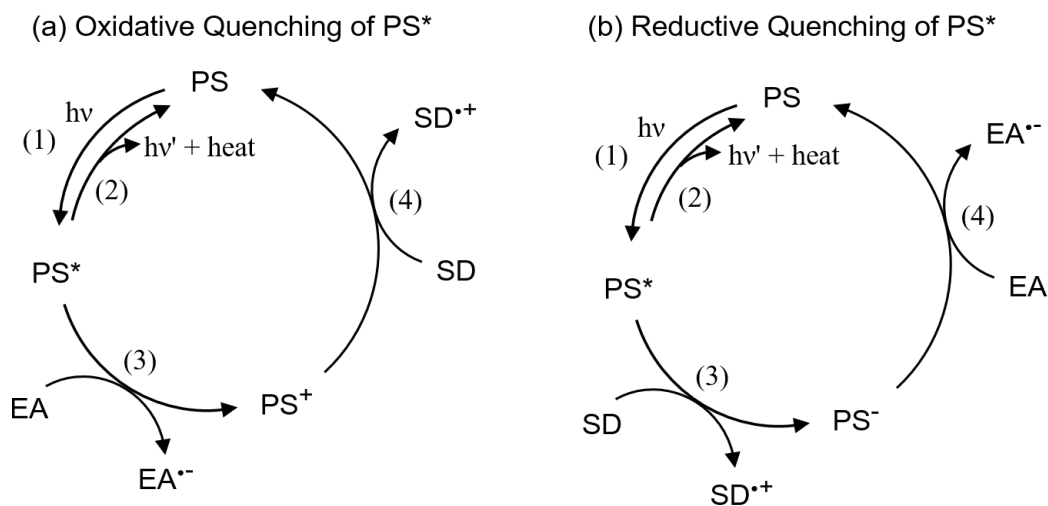


Fig. 1.2 Photosensitizer (PS) emission quenching pathways. EA: electron acceptor (catalyst or electron mediator), SD: sacrificial electron donor. Adapted with permission from ref.10¹⁰ copyright 2020 The Royal Society of Chemistry.

b. Quantum yield

Quantum yield includes internal quantum yield (IQY) and apparent quantum yield (AQY), which are crucial parameters for assessing the performance of a photocatalyst or a photocatalytic system. IQY is calculated as the ratio between the moles amount of product multiplied by the number of electrons necessary for the product formation and the moles amount of adsorbed photons (Equation 1.1), while AQY is calculated relatively to the molar number of incident photons (Equation 1.2).¹¹ Back electron transfer (BET) may decrease quantum yield. For example, in the case of oxidative quenching of PS* (Fig 1.2a), the reduced acceptor EA⁻ may quickly transfer back an electron to the oxidized photosensitizer (PS⁺) since the reaction is endowed with a large driving force. A large concentration of donor (SD) may help fighting BET.

$$IQY (\%) = \frac{\text{mol number of product} \times \text{number of electrons per product}}{\text{mol number of absorbed photons}} \times 100 \quad (\text{Eq. 1.1})$$

$$AQY (\%) = \frac{\text{mol number of product} \times \text{number of electrons per product}}{\text{mol number of incident photons}} \times 100 \quad (\text{Eq. 1.2})$$

Irradiation intensity and area, the concentration of CO₂, photocatalyst and sacrificial donor (SD), as well as the difference of standard redox potential between PS and SD may significantly influence the product yield.

c. Turnover number (TON)

Turnover number (TON) is defined by the ratio between the moles amount of product and catalyst once the reaction has stopped. In some cases, high turnover numbers have been obtained at a very low concentration of catalyst (nM range), leading to a very low absolute yield of CO₂ reduction products. In such cases, not only the real nature of the catalyst becomes doubtful but also performances may be overestimated.

The number of active sites number is a crucial parameter in evaluating the catalytic efficiency. In the case of molecular-supported systems, it will depend on the catalyst loading and active sites accessibility. A crude estimation of the catalyst content in supported systems can be made by calculating the amount of catalyst used in the synthesis process. Control of

the remaining catalyst left in solution after preparation (through UV-Vis spectroscopy for example) can help to refine the previous estimation. Inductively coupled plasma atomic emission spectroscopy (ICP-OES, after treatment of the material with a strong acid solution) and X-ray photoelectron spectroscopy (XPS) can be employed to more precisely quantify the amount of active species.

1.3 Homogeneous photocatalytic systems involving transition-metal-based molecular catalysts for 2-electron CO₂ reduction

The homogeneous catalysts we discuss here refer to molecular complexes that are homogeneously dispersed in solution. Common homogeneous catalysts for CO₂ reduction include metal-complexes, small organic molecules or enzymes.

1.3.1 Molecular-based photocatalytic system for CO₂-to-CO or to-HCOO⁻ conversion

Transition metal-based complexes have been gradually discovered in recent decades to photocatalyze the reduction of carbon dioxide. Fe-, Co-based cyclams, polypyridines, porphyrins, phthalocyanines, corroles, and others have been studied in the reduction of CO₂. While studying their catalytic activity, corresponding catalytic mechanism, have been gradually revealed. Regarding CO₂-to-formate conversion, a classical mechanism is that the reduced catalyst center generates a hydride that can nucleophilically attack CO₂ to produce a metal-formyl complex. The reduction of CO₂ to CO also faces the challenge of inhibiting the kinetic and thermodynamic competitive hydrogen evolution reaction (HER), which can be achieved upon fastbinding CO₂ in the presence of a proton source whose acidity is sufficient to promote subsequent C-O bond cleavage.

In the following paragraphs, I will describe a few examples of molecular CO₂ reduction photocatalysts. Table 1.1 and 1.2 provide an overview of the most efficient catalysts based Ni, Co and Fe, to date.

In ascorbic acid-containing aqueous solutions, Tinnemans *et al.* used Ni and Co cyclams (**Co1**, **Co2** and **Ni1**, Figs. 1.3 and 1.4) as catalysts for the visible-light-driven CO₂ reduction. With Ru(bpy)₃²⁺ (**PS1**, Fig. 1.5) as a photosensitizer, CO was produced with maximum

selectivity of 32% (Table 1.1, entry 1-4).¹² Moderate selectivity (57%) with a Ni^{II} cyclam (**Ni2**, Fig. 1.4.) has been reported in similar aqueous conditions, while its corresponding dimer (**Ni1**, Fig. 1.7) showed 89% selectivity and a TON 6 times higher than the monomer (Table 1.1, entry 5).¹³

At the same time, Brunschwig and Fujita *et al.* have tried to unveil possible intermediates during the photocatalysis with Co cyclams (**Co3-Co5**, **Co7**, Fig. 1.3).¹⁴⁻¹⁶ By employing transient absorption spectroscopy, Fourier-transform infrared spectroscopy (FTIR) and X-ray absorption near edge structure (XANES) analysis, a 5-coordinated CO₂ adduct intermediate [Co^{III}L(CO₂²⁻)]⁺ (in which L stands for the cyclam type ligand) was identified for the four studied cyclams, with CO₂ being stabilized by the NH protons on the macrocycle ligand. In solution, an intermediate [(CH₃CN)Co^{III}L(CO₂²⁻)]⁺ can form with the solvent molecule (CH₃CN in this case) coordinated with the metal center, which led to a more stable adduct by internal charge transfer from the metal center to the CO₂. The six-coordinated intermediate is then further reduced, with assistance of a proton or another CO₂ molecule, to afford CO.^{17, 18}

The catalytic mechanism for CO₂ reduction has thus been studied through a series of Co-based cyclams (**Co3-Co8**, Fig. 1.3) with interesting performances that led to mechanistic studies, including the identification of some reaction intermediates involved in the processes. Some aromatic organic molecules were applied as photosensitizers. The main catalytic product is CO with p-terphenyl (**PS2**, Fig. 1.5 and Table 1.1, entries 6-13)^{19, 20} while it changes to formate with phenazine (**PS3**, Fig. 1.5. and Table 1.1, entry 14).²¹ The reason for this difference is that phenazine can donate both electron and proton during catalysis. The formation of a Co–H hydride species is enhanced by proton transfer from the phenazine sensitizer, which was proposed to lead to formate upon CO₂ insertion. Different selective reduction has also been found with molecular catalysts containing different metals.²² Two complexes with cobalt and iron, (Co9, Fe1, Figs. 1.3 and 1.4) exhibits selectivity towards CO and formate production respectively (Table 1.1, entries 15-17, 18-20) due to a slower C-O bond cleavage in the catalytic process of Feqpy, resulting in higher basicity of the bonded carbon atoms.

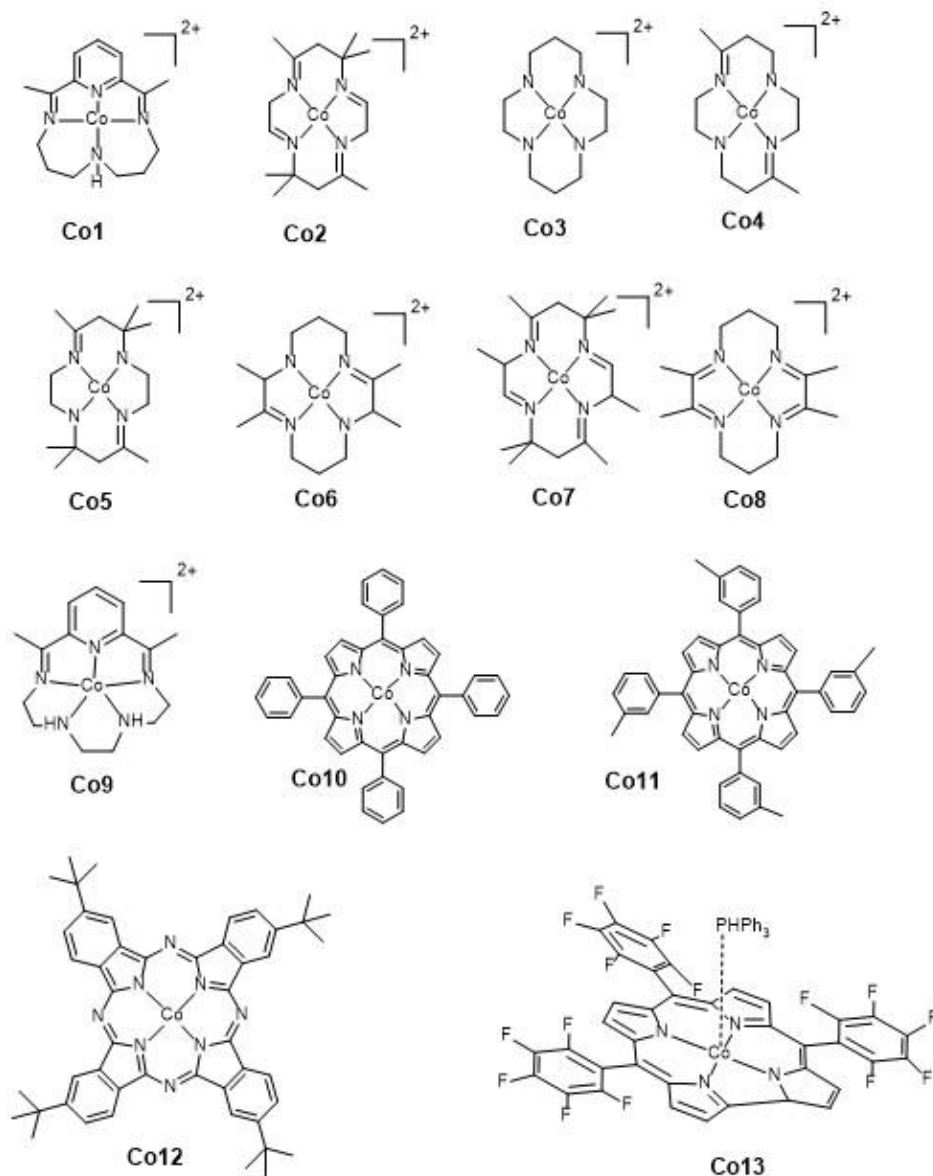
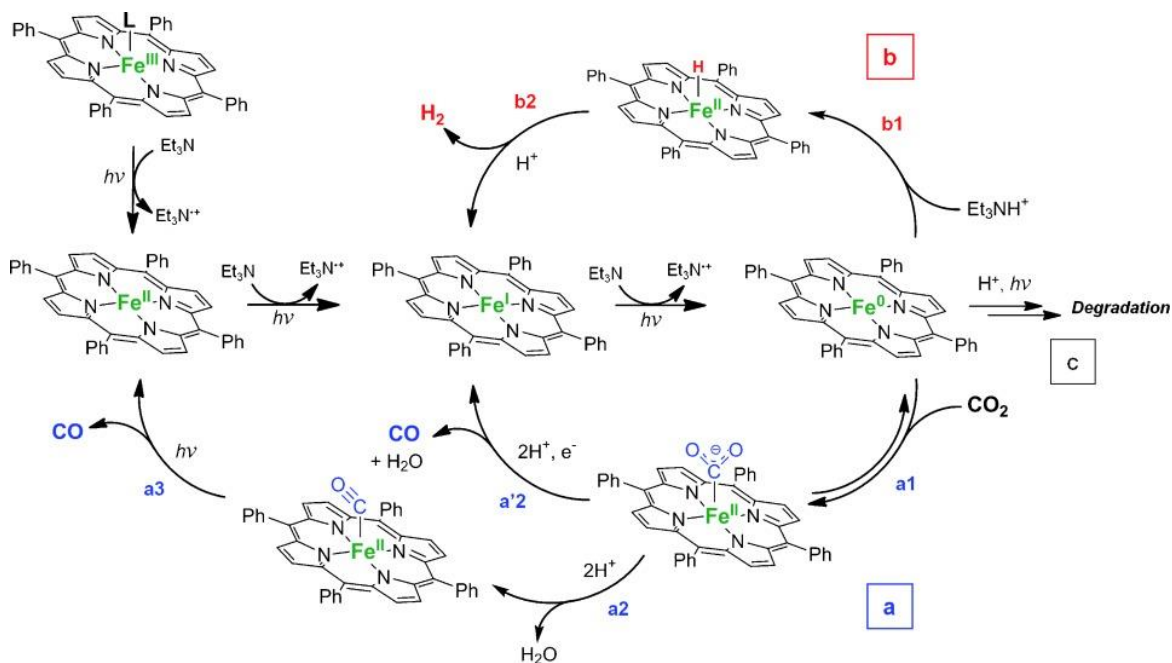


Fig. 1.3 Cobalt-based complexes.

Fe-, Co-porphyrin, and their derivatives (**Fe2** **Fe3** in Fig. 1.4,²³ **Co10**,²⁴ **Co11**²⁵ in Fig. 1.3.) were also found to be active CO₂ catalysts (Table 1.1, entries 21-23). **Fe3** (Fig. 1.4) was first used for the photoreduction of CO₂ in 1997 (Table 1.1, entries 24, 25).^{26, 27} With the exploration of the catalytic activity, its possible mechanism has been gradually revealed. In a DMF/TEA solution of **Fe3** (Fig. 1.4), photoinduced ligand-to-metal charge transfer generated Fe^{II} from initial Fe^{III} species. Fe^{II} was further converted to Fe^I upon light excitation and

reductive quenching by TEA. Finally, the catalytically active species “Fe⁰” was proposed to be formed by the disproportionation of two Fe^I species (see Scheme 1.2).



Scheme 1.2 Proposed mechanism for the photochemical catalytic reduction of CO₂ to a) CO and b) H₂ with Fe porphyrin catalysts (L = Cl). For CO formation, subpathway **a1–a2–a3** is followed in the case of FeTPP whereas subpathway **a1–a'2** is followed in the case of both **Fe7** and **Fe8** (see Fig. 1.4). Adapted with permission from ref. 27²⁷. Copyright 2014 WILEY-VCH Verlag GmbH & Co. KGaA, Weinheim.

The structural optimization of iron porphyrin led to catalytic activity in recent years. A modified Fe simple tetraphenyl porphyrin with OH groups in all ortho, ortho' positions of the four phenyl groups (**Fe7**, Table 1.1, entry 32) were studied by electrochemical methods.²⁷ Electrochemistry confirmed that the hydroxyl group is versatile in the porphyrin molecule. On the one hand, the —OH stabilizes the Fe-CO₂ adduct through hydrogen bond. At the same time, the —OH acts as a transfer station for protons to accelerate the cleavage of the C-O bond.²⁸

This complex exhibits interesting activity in the photocatalytic reduction of carbon dioxide. A good selectivity for CO (85%) was already obtained with **Fe7** without the aid of photosensitizer, significantly higher than that with **Fe8**. In the presence of an organic sensitizer (9-CNA, **PS5**, Fig. 1.5) and a strongly reducing Ir complex (Ir(ppy)₃³⁺, **PS6**, Fig.

1.5), higher CO selectivities were further obtained, reaching 93% and 100%, respectively (Table 1.1, entries 33-34).²⁹

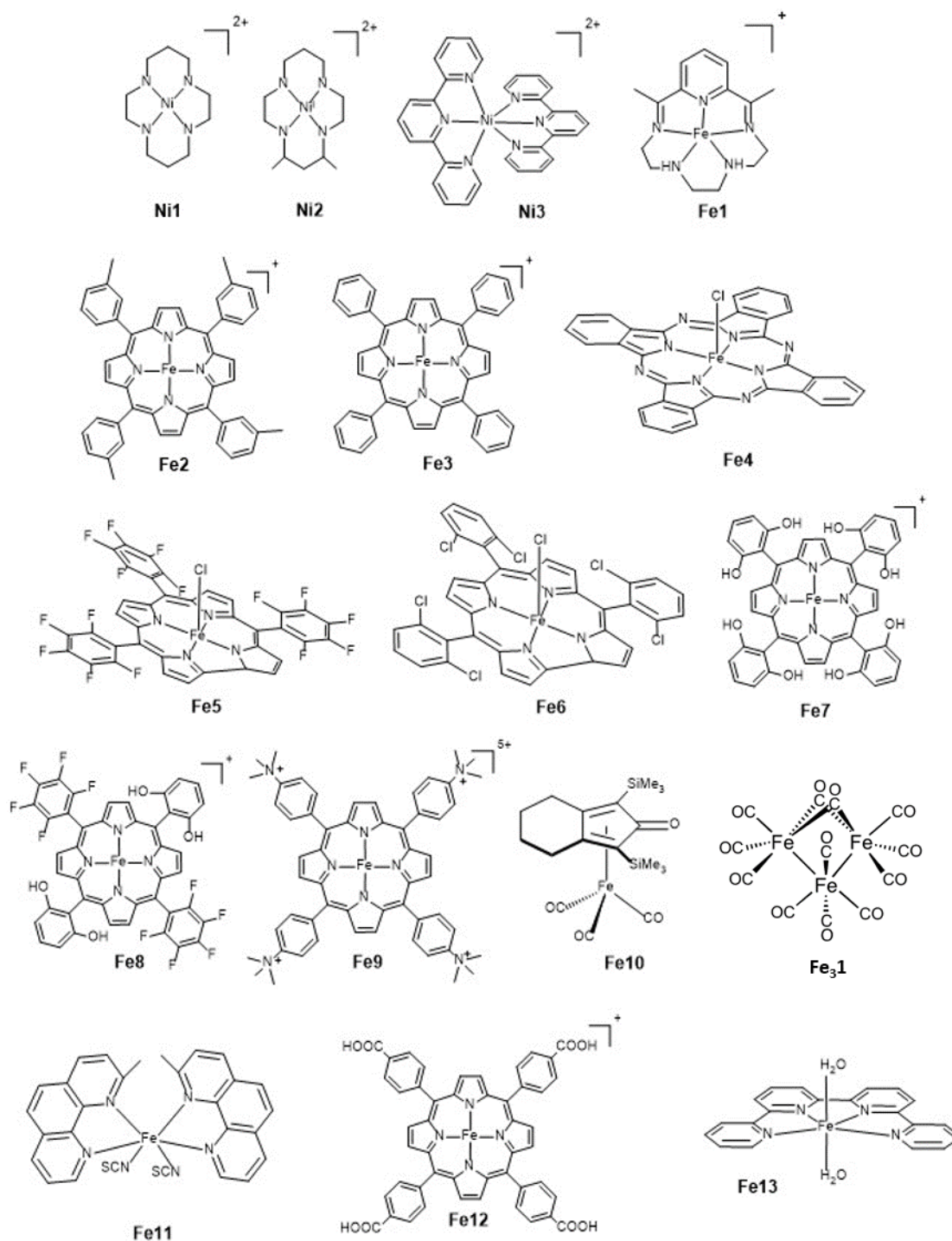


Fig. 1.4 Nickel- and iron-based molecular complexes.

In addition to —OH, porphyrins have also been modified with trimethylamine (**Fe9**), four positively charged trimethylammonium groups equipped at all para positions of each phenyl rings of the porphyrin. Under similar conditions with **Fe7**, BIH was employed as sacrificial donor for a non-sensitized CO₂ reduction with **Fe9**, showing an enhanced efficiency and selectivity (100%) towards CO evolution (Table 1.1, entry 35).³⁰ Moreover, the catalyst was able to convert CO₂ to CO in aqueous solutions (Table 1.1, entry 36).³¹ Replacing purpurin with Ir(ppy)₃ as a sensitizer, **Fe9** can trigger the reduction of CO₂ to CH₄ production in a CH₃CN solution containing up to 70% H₂O (Table 1.1, entries 37, 38).^{32, 33} This is of great significance for using iron-based molecular complexes to reduce CO₂ to CO and then to CH₄ under mild conditions in visible-light-derived systems.

Fe- and Co-based phthalocyanines (**Fe4**, **Co12**, Figs. 1.3 and 1.4 and Table 1.1, entries 26-28)²³ and corroles (**Co13**, **Fe5**, **Fe6**, Table 1.1, entries 29-31)³⁴ have also been introduced in photocatalytic reduction of CO₂. The Fe- and Co- phthalocyanines, sensitized by p-terphenyl, can reach comparative TON_{CO} to those of porphyrin analogs, such as **Fe3** and **Co10**.²⁵ The high activity indicates the unlimited potentiality of these catalysts in the catalytic reduction of CO₂.

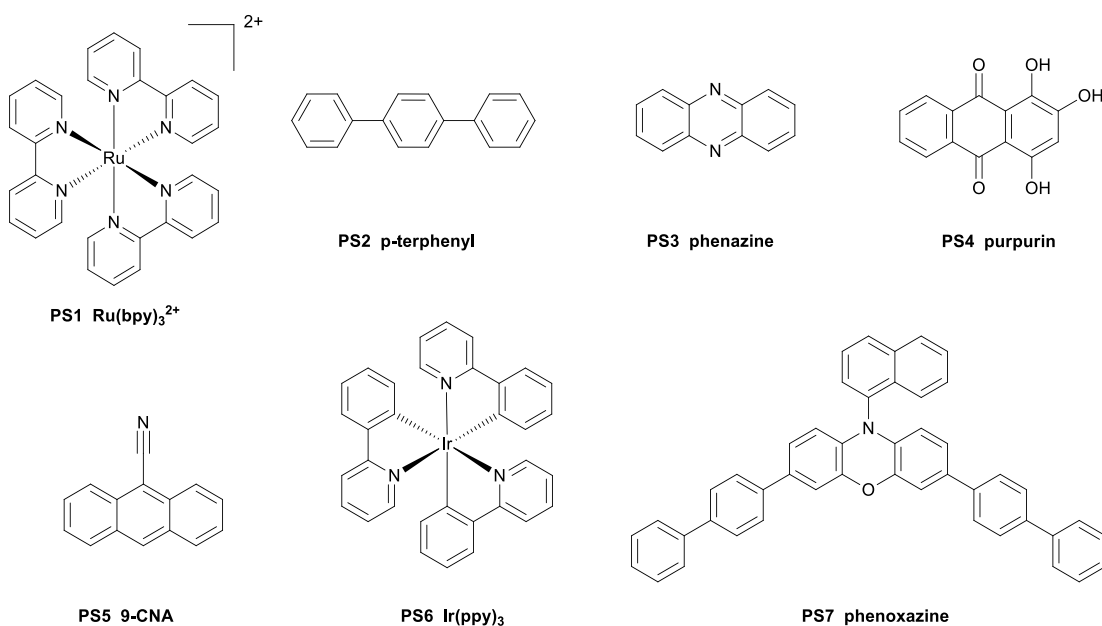


Fig. 1.5 Typical molecular photosensitizers including metal-based (Ru, Ir) complexes and organic aromatic molecules.

In addition, a series of Fe-carboxyl complexes also show catalytic activity in the reduction of CO₂. Fe-carboxyl complexes are also active catalysts for CO₂ reduction to CO and formate. Applying Ir(ppy)₃ and TEOA to N-methyl-2-pyrrolidone (NMP) solution, a commercially Fe₃(CO)₁₂ (**Fe31**, Fig. 1.4) was reported to produce CO with a 50% selectivity and TON *ca.* 100 (Table 1.1, entry 39).³⁵ Subsequently, the same group reported another carboxyl complex, (cyclopentadienone)iron-tricarbonyl (Fe(cpd)(CO)₃, **Fe10**, Fig. 1.4), that could accomplish CO₂ reduction with a TON_{CO} of 600 and selectivity of 50% in 1 hour (Table 1.1, entry 40).³⁶ Further, with a Cu complex as sensitizer and BIH as the sacrificial donor, CO could be obtained in an enhanced selectivity of 99% with a high quantum yield of 13.3% (Table 1.1, entry 41).³⁷

It is also worth mentioning that Ishitani *et al.* have reported a Cu-based complex sensitized efficient photocatalytic system using a Fe-containing complex as the catalyst in which the metal is chelated by two di-methyl 1,10-phenanthroline molecules (Fe(dmp)₂(NCS)₂, **Fe11**, Fig. 1.4). The visible-light-driven photocatalytic reduction can convert CO₂ to CO with a TON of 273 and a quantum yield of 6.7% (Table 1.1, entry 42).³⁸

Table 1.1 Photocatalytic CO₂ reduction using non-noble metal complexes.

Entry	CRC	PS	Conditions	Illumination	Irrad. time	Product (TON)	Selectivity	QY(%)	Ref
1	Co1 0.08 mM	[Ru(bpy) ₃] ²⁺ 0.5 mM	0.5/0.5 M H ₂ A/HA ⁻ H ₂ O (pH=4)	Daylight lamp	18 h	CO (1.2)	< 1% (CO)	-	12
2	Co2 0.08 mM	[Ru(bpy) ₃] ²⁺ 0.5 mM	0.5/0.5 M H ₂ A /HA ⁻ H ₂ O (pH=4)	Daylight lamp	18 h	CO (28.7)	32% (CO)	-	12
3	Ni1 2 mM	[Ru(bpy) ₃] ²⁺ 0.5 mM	H ₂ A H ₂ O (pH=5)	Xe lamp 1000 W, λ=440 nm	24 h	CO (0.1)	-	0.06% (CO) 0.003% (HCOO ⁻)	13
4	Ni1 0.1 mM	[Ru(bpy) ₃] ²⁺ 0.5 mM	H ₂ A H ₂ O (pH=4)	Xe lamp 1000 W 340 <λ <600 nm	8 h	CO (4.8)	12% (CO) 88% (H ₂)	-	13
5	Ni ₂ 1 0.25 mM	[Ru(bpy) ₃] ²⁺ 0.5 mM	H ₂ A H ₂ O (pH=4)	Hg lamp 460 W, λ=435 nm	1 h	CO (4.4)	89%	-	13
6	Co12 1.7 mM	p-terphenyl 2 mM	TEOA in CH ₃ CN/ CH ₃ OH (4:1 v:v)	Hg lamp 500 W high-pressure λ > 290 nm	1 h	CO (10.2) HCOO ⁻ (6.7)	-	15 (CO) 10 (HCOO ⁻) λ=313 nm	19, 20
7	Co3 1.7 mM	p-terphenyl 2 mM	TEA in CH ₃ CN/ CH ₃ OH (4:1 v:v)	Hg lamp 500 W high-pressure λ > 290 nm	1 h	CO (4.7) HCOO ⁻ (2.3)	60.5% (CO) 31.8% (HCOO ⁻)	-	19, 20
8	Co13 1.7 mM	p-terphenyl 2 mM	TEOA in CH ₃ CN/ CH ₃ OH (4:1 v:v)	Hg lamp 500 W high-pressure λ > 290 nm	1 h	CO (5.3) HCOO ⁻ (3.5)	51.6% (CO) 34.4% (HCOO ⁻)	-	19, 20
9	Co14 1.7 mM	p-terphenyl 2 mM	TEOA in CH ₃ CN/ CH ₃ OH (4:1 v:v)	Hg lamp 500 W high-pressure λ > 290 nm	1 h	CO (2.0) HCOO ⁻ (0.3)	52.4% (CO) 7.9% (HCOO ⁻)	-	19, 20
10	Co15 1.7 mM	p-terphenyl 2 mM	TEOA in CH ₃ CN/ CH ₃ OH (4:1 v:v)	Hg lamp 500 W high-pressure λ > 290 nm	1 h	CO (4.9) HCOO ⁻ (2.5)	58.5% (CO) 30.4% (HCOO ⁻)	-	20

11	Co11 1.7 mM	p-terphenyl 2 mM	TEOA in CH ₃ CN/ CH ₃ OH (4:1 v:v)	Hg lamp 500 W high-pressure $\lambda > 290$ nm	1 h	CO (1.0)	44% (CO)	-	20
12	Co16 1.7 mM	p-terphenyl 2 mM	TEOA in CH ₃ CN/ CH ₃ OH (4:1 v:v)	Hg lamp 500 W high-pressure $\lambda > 290$ nm	1 h	CO (2.7) HCOO ⁻ (0.4)	30.3% (CO) 4.8% (HCOO ⁻)	-	20
13	Co17 1.7 mM	p-terphenyl 2 mM	TEOA in CH ₃ CN/ CH ₃ OH (4:1 v:v)	Hg lamp 500 W high-pressure $\lambda > 290$ nm	1 h	-	-	-	20
14	Co12 10 mM	phenazine	TEA in CH ₃ CN/ CH ₃ OH/TEA (2:1:1, v:v:v)	Hg lamp 500 W high-pressure $\lambda > 290$ nm	1 h	CO (0.08) HCOO ⁻ (1.1)	92.2% (HCOO ⁻) 7.12% (CO)	-	21
15	Co9 0.005 mM	[Ru(bpy) ₃] ²⁺ 0.3 mM	BIH in CH ₃ CN/0.5 M TEOA	LED $\lambda=460$ nm	80 min	CO (2660)	98% (CO)	-	22
16	Co9 0.005 mM	[Ru(bpy) ₃] ²⁺ 0.3 mM	BIH in CH ₃ CN/0.5 M TEOA	LED $\lambda=460$ nm	80 min	CO (497) HCOO ⁻ (5) H ₂ (3)	98% (CO)	2.8 (CO)	22
17	Co9 0.005 mM	purpurin 2 mM	BIH in DMF	LED $\lambda=460$ nm	11 h	CO (790)	95% (CO)	0.8 (CO)	22
18	Fe1 0.005 mM	[Ru(bpy) ₃] ²⁺ 0.3 mM	BIH in CH ₃ CN/TEOA (4:1 v:v)	LED $\lambda=460$ nm	3 h	CO (3844) HCOO ⁻ (534) H ₂ (118)	85% (CO)	1.45 (CO) first 45 min	22
19	Fe1 0.005 mM	[Ru(bpy) ₃] ²⁺ 0.3 mM	BIH in CH ₃ CN/TEOA (4:1 v:v)	LED $\lambda=460$ nm	3 h	CO (1879) HCOO ⁻ (48) H ₂ (45)	97% (CO)	8.8 (CO)	22
20	Fe1 0.005 mM	purpurin 2 mM	BIH in DMF	LED $\lambda=460$ nm	12 h	CO (1365)	92% (CO)	1.1 (CO)	22
21	Co10 10 μ M	-	TEA in CH ₃ CN	Xe lamp $\lambda > 320$ nm	20 h	HCOO ⁻ /CO (300)	-	-	24
22	Co11 0.05 mM	p-terphenyl 3 mM	TEA in CH ₃ CN	Xe lamp $\lambda > 320$ nm	20 h	CO (62)	-	-	25
23	Fe2 0.034 mM	p-terphenyl 3 mM	TEA in CH ₃ CN	Xe lamp 300W, $\lambda > 320$ nm	20 h	CO (61.8)	-	-	39

24	Fe4 0.01 mM	-	TEA in CH ₃ CN	Xe lamp 300W	15 min	CO (70)	-	5	26
25	Fe4 0.01 mM	-	TEA in CH ₃ CN	VIS light (BG40-type optical filter)	10 h	CO (17)	8% (CO) in 1h	-	27
26	Fe4 0.15 mM	-	TEA in CH ₃ CN	Xe lamp $\lambda > 310$ nm	6 h	CO (9)	-	-	23
27	Fe4 0.15 mM	p-terphenyl 3 mM	TEA in CH ₃ CN	Xe lamp $\lambda > 310$ nm	6 h	CO (90)	-	-	23
28	Co12 0.15 mM	p-terphenyl 3 mM	TEA in CH ₃ CN	Xe lamp $\lambda > 310$ nm	6 h	CO (47.5)	-	-	23
29	Co13 0.042 mM	p-terphenyl 3 mM	TEA in CH ₃ CN	Xe lamp $\lambda > 310$ nm	6 h	CO (86)	-	-	34
30	Fe5 0.048 mM	p-terphenyl 3 mM	TEA in CH ₃ CN	Xe lamp $\lambda > 310$ nm	6 h	CO (43.8)	-	-	34
31	Fe6 0.045 mM	p-terphenyl 3 mM	TEA in CH ₃ CN	Xe lamp $\lambda > 310$ nm	6 h	CO (51.1)	-	-	34
32	Fe7 0.01-0.05 mM	-	TEA in CH ₃ CN	VIS light BG40 filter	10 h	CO (28)	93% (CO) in 1h	-	27
33	Fe7 2 μ M	9-CNA 0.2 mM	TEA in CH ₃ CN	Xe lamp $\lambda > 420$ nm	45 h	CO (40-60)	100% (CO)	0.08 (CO)	29
34	Fe7 2 μ M	fac-Ir(ppy) ₃ 0.2 mM	TEA in CH ₃ CN	Xe lamp $\lambda > 420$ nm	55 h	CO (140)	93% (CO)	0.13 (CO)	29
35	Fe9 2 μ M	-	BIH 20 mM in CH ₃ CN	Solar simulator $\lambda > 420$ nm	47 h	CO (63)	100% (CO)	-	30
36	Fe9 2 μ M	purpurin 2 mM	TEA, NaHCO ₃ in CH ₃ CN/H ₂ O (1:9 v:v)	Solar simulator $\lambda > 420$ nm	47 h	CO (60), H ₂ (5)	95% (CO)	-	31
37	Fe9 2 μ M	fac-Ir(ppy) ₃ 0.2 mM	TEA in CH ₃ CN	Solar simulator $\lambda > 420$ nm	102 h	CO (367) CH ₄ (79) H ₂ (26)	17% (CO) 78% (CH ₄) 5% (H ₂)	-	32

38	Fe9 2 μ M	fac-Ir(ppy) ₃ 0.2 mM	TEA in CH ₃ CN/H ₂ O (3:7 v:v)	Solar simulator $\lambda > 420$ nm	47 h	CO (24), CH ₄ (3) H ₂ (5)	9% (CO) 75% (CH ₄) 16% (H ₂)	-	33
39	Fe ₃ 1 3-6 μ M	Ir(ppy) ₃ 0.025 mM	TEOA in (N-methyl- 2-pyrrolidone) NMP	Hg lamp 2.5 W 400 < λ < 700 nm	5 h	CO (100)	50% (CO)	-	35
40	Fe10 5 μ M	Ir(ppy) ₃ 1.67 mM	TEOA in NMP/TEOA (5:1, v:v)	Hg lamp 2.5 W 400 < λ < 700 nm	1 h	CO (600)	50% (CO)	-	36
41	Fe10 1 μ M	[Cu(CH ₃ CN) ₄] PF ₆ 5 μ M	BIH in NMP/TEOA (5:1, v:v)	Hg lamp 1.5 W 400 < λ < 700 nm	5 h	CO (487)	99% (CO)	13	37
42	Fe11 0.05 mM	Cu-PS 0.25 mM	BIH in CH ₃ CN/TEOA (5:1 v:v)	Hg lamp $\lambda = 435.8$ nm	12 h	CO (273)	78% (CO)	6.7	38
43	Fe23 0.05 mM	Ru(phen) ₃ ²⁺ 0.2 mM	BIH in CH ₃ CN/H ₂ O (1:1 v:v)	LED $\lambda = 460$ nm	68 h	CO (14095)	98% (CO)	0.8 (in 24 h)	40
44	Fe4 10 μ M	PS7 1 mM	TEA 0.1 M in DMF	Solar simulator $\lambda > 435$ nm	102 h	H ₂ (23) CO (140) CH ₄ (29)	12% (H ₂) 73% (CO) 15% (CH ₄)	-	41

CRC: CO₂ reduction catalyst

PS: photosensitizer

Irra. time: irradiation time

QY: quantum yield

1.3.2 Molecular dyads photocatalysts for CO₂ reduction

To further improve the catalytic efficiency of the reduction of CO₂, a new idea has been put forward. Some efforts have been indeed devoted to the combination of catalysts and photosensitizers into supramolecular assemblies (which are usually known as dyads) through covalent linkage, to pursuing facility energy/electron transfer between subunits.

The first try was reported by Kimura *et al.* in 1992. They combined a Ru(phen)₃²⁺ (phen=1,10-phenanthroline) as sensitizer unit and [Ni(cyclam)]²⁺ as catalyst together, and afforded a supramolecule (Ru(phen)₂[phen-Ni(cyclam)](ClO₄)₄, **RuNi1**, Fig. 1.6). However, the **RuNi1** only showed a TON_{CO} < 1, indicating the inactivity of the reaction. A mixed system of Ni(cyclam)²⁺ and Ru(phen)₃²⁺ showed even better catalytic performance for CO production (Table 1.2, entry 4).⁴²

The failed attempt did not depress the researchers. Another dyad **RuNi2** was synthesized successfully by Aukauloo *et al.*, including a ruthenium trisbipyridyl-like unit covalently attached to a nickel cyclam *via* a triazole ring. In aqueous ascorbate solution, **RuNi2** was able to afford CO with a small TON_{CO} of 5.2 under 450 nm illumination, as a sacrificial donor under 450 nm illumination with a few TON (Table 1.2, entry 5).⁴³

Instead of nickel, cobalt-based catalysts were also linked to ruthenium photosensitizer for CO₂ reduction (**RuCo1** and **RuCo2**, Fig. 1.6). While the mixed sample of [Co-tris(bpy)]²⁺ and [Ru(bpy)₃]²⁺ show a promising catalytic results (TON_{CO} = 9, TON_{formate} = 28, TON_{H₂} = 16, Table 1.2, entry 8), these dyads show improved selectivity of formate production. In the mixed DMF:H₂O:TEOA (3:1:1) solution, TON_{CO} = 3, TON_{formate} = 31, TON_{H₂} = 1 were obtained with **RuCo1**; TON_{CO} = 5, TON_{formate} = 34, TON_{H₂} = 1 were obtained with **RuCo2** (Table 1.2, entries 6, 7).⁴⁴

Moreover, **RuCo3**, **RuCo4**, **RuCo5** (Fig. 1.6) have been synthesized gradually. With BIH as a sacrificial donor, the three catalysts can generate CO in CO₂ saturated CH₃CN/TEOA (5:1 v:v) with a selectivity ranging from 67% to 87% using under Xe lamp irradiation ($\lambda > 415$ nm, Table 1.2, entries 9-11).⁴⁵

All investigations illustrate that conjugation between the PS center and catalyst can promote catalytic performances due to the desirable electronic interaction during the subunits, which is possible to generate higher selectivity and better stability of CO₂ reduction system.

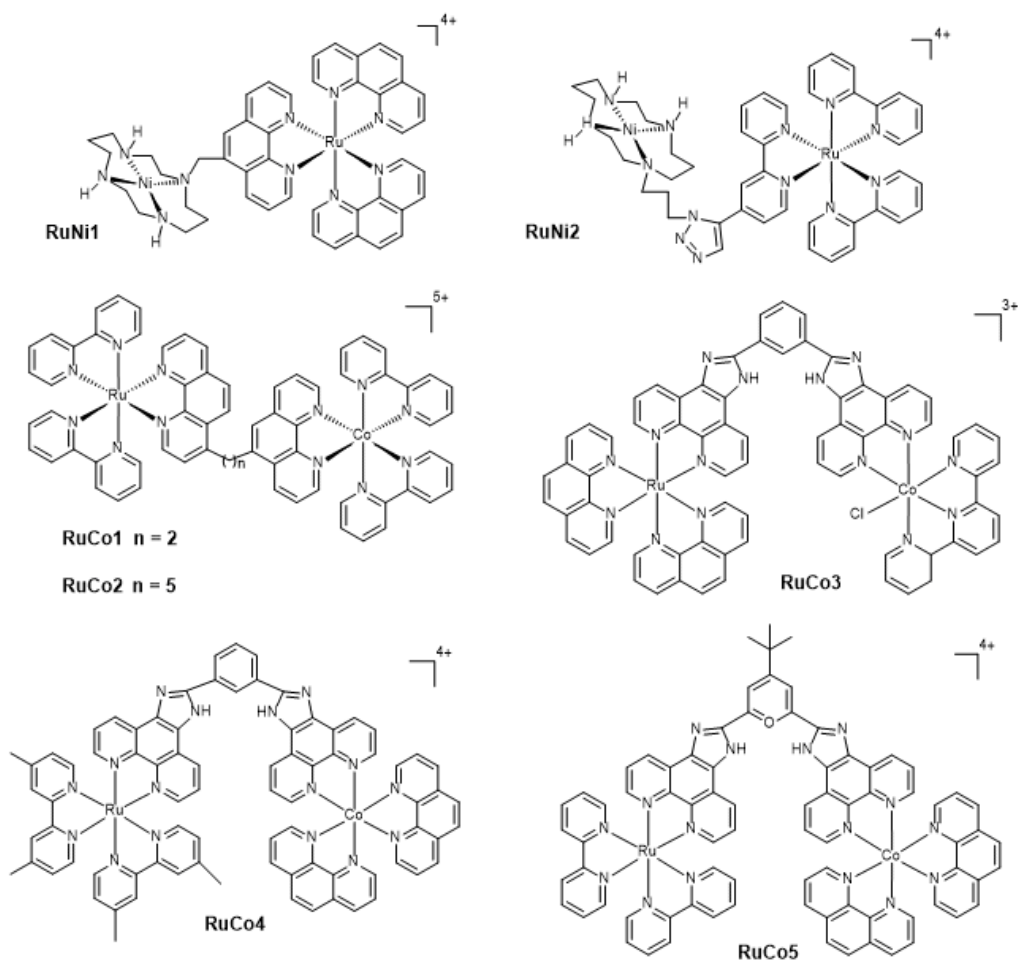


Fig. 1.6 Molecular structures of sensitizer-catalyst dyads.

Table 1.2 Photocatalytic CO₂ reduction using molecular dyads and bimetallic complexes.

Entry	CRC	PS	conditions	illumination	Irrad. time	Product (TON)	Selectivity	QY(%)	Ref
1	Ni2 0.25 mM	[Ru(bpy) ₃] ²⁺ 0.5 mM	H ₂ A in H ₂ O (pH=4)	Hg lamp 460 W	1 h	CO (0.7)	-	-	13
2	Ni ₂ 2 0.25 mM	[Ru(bpy) ₃] ²⁺ 0.5 mM	H ₂ A in H ₂ O (pH=4)	Hg lamp 460 W	1 h	CO (4.4)	94% CO	-	13
3	Co ₂ 1 10 μM	fac-Ir(ppy) ₃ 0.4 mM	TEA in CH ₃ CN/H ₂ O (5:1 v:v)	LED λ = 450 nm	60 h	CO (56.9) HCOO ⁻ (64.2) H ₂ (181.6)	18.8% CO 21.2% HCOO ⁻ 60% H ₂	-	46
4	RuNi1 0.5 mM	-	H ₂ A in H ₂ O (pH=4)	Xe lamp 500 W λ > 450 nm	44 h	CO (<1)	72% CO	-	42
5	RuNi2 0.035 mM	-	H ₂ A in H ₂ O (pH=6.5)	Xe lamp 500 W λ > 450 nm	60 h	CO (5.2) H ₂ (2)	-	-	43
6	RuCo1 0.5 mM)	-	TEOA in DMF:H ₂ O (3:1 v:v)	Xe lamp 500 W 400 < λ < 750 nm	29 h	CO (3) HCOO ⁻ (31) H ₂ (1)	9.3% CO	-	44
7	RuCo2 0.5 mM	-	TEOA in DMF:H ₂ O (3:1 v:v)	Xe lamp 500 W 400 < λ < 750 nm	29 h	CO (5) HCOO ⁻ (34) H ₂ (1)	12.7% CO	-	44
8	[Co(bpy) ₃] ³⁺ 0.5 mM	[Ru(bpy) ₃] ²⁺ 0.5 mM	TEOA in DMF:H ₂ O (3:1 v:v)	Xe lamp 500 W 400 < λ < 750 nm	29 h	CO (9) HCOO ⁻ (28) H ₂ (16)	17% CO	-	44
9	RuCo3 0.1 mM	-	BIH in CH ₃ CN:TEOA (3:1 v:v)	Xe lamp 300 W λ > 415 nm	8 h	CO (51) H ₂ (13)	79.6% CO	-	45
10	RuCo4 0.1 mM	-	BIH in CH ₃ CN:TEOA (3:1 v:v)	Xe lamp 300 W λ > 415 nm	8 h	CO (54) H ₂ (8)	87.2% CO	-	45
11	RuCo5 0.1 mM	-	BIH in CH ₃ CN:TEOA (3:1 v:v)	Xe lamp 300 W λ > 415 nm	8 h	CO (70) H ₂ (39)	64.3% CO	-	45
12	Co ₂ 2 0.025 μM	[Ru(phen) ₃] ²⁺ 0.4 mM	TEOA in CH ₃ CN:TEOA (4:1 v:v)	LED λ = 450 nm	10 h	CO (16896)	98% CO	0.04% CO	47
13	CoZn1 0.025 μM	[Ru(phen) ₃] ²⁺ 0.4 mM	TEOA in CH ₃ CN:TEOA (4:1 v:v)	LED λ = 450 nm	10 h	CO (65000)	98% CO	0.15% CO	48

14	Co ₂ 3 0.05 mM	[Ru(phen) ₃] ²⁺ 0.2 mM	TEOA/BIH in CH ₃ CN	LED λ=460 nm	60 h	CO (221)	20.4% CO	2.6% HCOO ⁻	49
						HCOO ⁻ (821)	75.9% HCOO ⁻		
						H ₂ (40)	3.7% H ₂		
15	Co ₂ 3 0.05 mM	[Ru(phen) ₃] ²⁺ 0.2 mM	PhOH/BIH in CH ₃ CN	LED λ=460 nm	1 h	CO (829)	96% CO	-	49
						HCOO ⁻ (12)	1.5% HCOO ⁻		
						H ₂ (22)	2.5% H ₂		

CRC: CO₂ reduction catalyst

PS: photosensitizer

Irra. time: irradiation time

QY: quantum yield

1.4 CO₂ photoreduction with bi-metallic catalysts

Ni–Fe carbon monoxide dehydrogenase (CODH) is a natural metalloenzyme that can reversibly convert CO₂ into CO. CO₂ binds to both metal centers, with the C atom interacting with the Ni^I nucleophilic site and one of the O atoms bound to the Fe^{II} electrophilic site.

The homodimeric Ni–Fe carbon monoxide dehydrogenase (CODH) is a natural metalloenzyme from the anaerobic bacterium *Carboxydotherrmus hydrogenoformans* that can reversibly catalyze the reduction of CO₂ to CO.⁵⁰ The prototype structure for CODH from anaerobic bacteria and archaea contains five metal clusters. And their integral Ni ion, which is the likely site of CO₂ reduction, is coordinated by four sulfur ligands with square planar geometry. In the catalysis of CO₂ reduction, CO₂ bind to Fe and Co, with one of the O atoms bound to the Fe^{II} electrophilic site and the C atom interacting with the Ni^I nucleophilic site. In this way, the Fe center and Ni center can work synergistically to facilitate the cleavage of the C–O bond and achieve high selectivity. To mimic this sophisticated catalytic process, several bimetallic complexes have been synthesized.

Researches on dinuclear metallic complexes as catalysts to reduce CO₂ have been reported both in photocatalytic and electrocatalytic conditions. However, only a few of them are capable of reducing CO₂ with metal synergy.

A bimakrocyclic Ni(II) complex (**Ni21**, Fig. 1.7) was synthesized as catalyst in 1996. Two dicyclam units in the trans *III* form are linked equatorially with respect to the chair-form six-membered chelate ring. In ascorbic acid aqueous solution (pH = 4), CO was generated with a turnover number of 0.4.

Another similar bimakrocyclic Ni(II) complex (**Ni22**, Fig. 1.7) was synthesized with two dimethylcyclam units. The most remarkable feature, different from the case of corresponding monocyclic complex (**Ni2**, Fig. 1.4 and Table 1.2, entry 1), is the configuration of methyl groups which occupy the axial positions of the six-membered

chelate rings. Such structure reduces the capability for accepting axially coordinating water molecules. The dimerized Ni-cyclam **Ni₂** shows enhanced efficiency and selectivity in CO₂ to CO conversion with a TON of 4.4 in aqueous solution at pH 4 (Table 1.2, entry 2), while the **Ni₂** only show a negligible CO production with TON of 0.7.

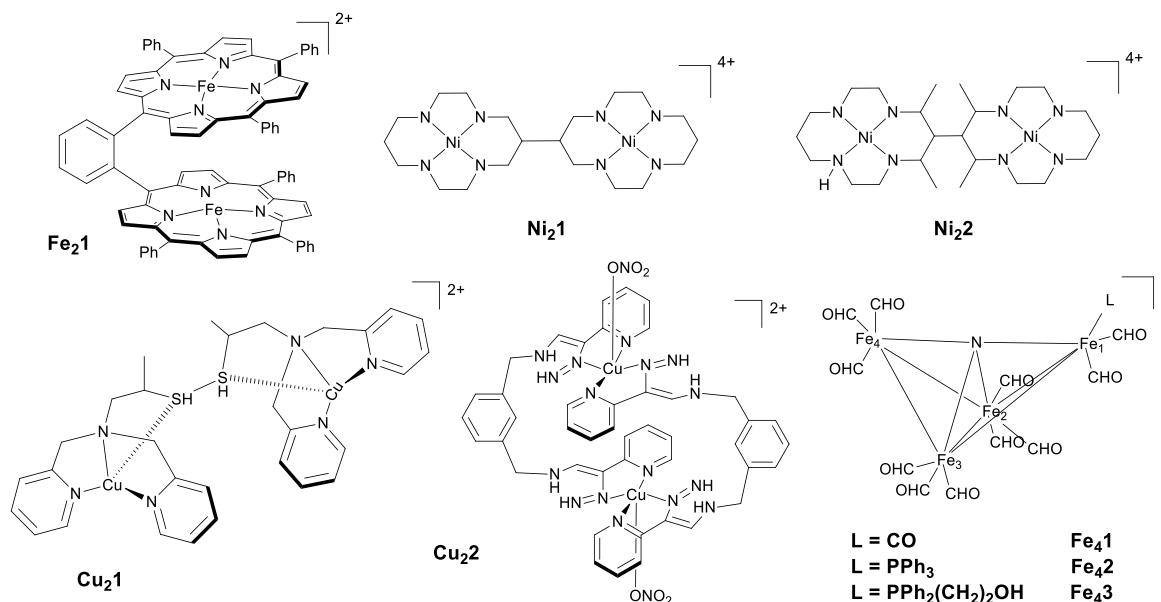


Fig. 1.7 Molecular structures of various bi- and multi-metallic complexes.

Recently, a dinuclear Co complex **Co₂1** (Fig. 1.8) was synthesized by Zhu *et al.*, which contains an oxygen atom at the *cis*-coordination site.⁴⁶ In CH₃CN/H₂O (5:1) solution with TEA as a sacrificial donor, promising catalytic results towards CO₂ reduction can be obtained with **Co₂1**. Under 450 nm irradiation, CO and formate were generated with TON of 57 and 64, respectively (Table 1.2, entry 3). However, the dominant products was H₂ (TON = 182).

Binuclear cobalt complexes have also been reported, showing remarkable catalytic ability. Lu *et al.* have synthesized a binuclear cobalt cryptate catalyst [Co₂(OH)L](ClO₄)₃ (L=N[(CH₂)₂NHCH₂(*m*-C₆H₄)CH₂NH(CH₂)₂]₃N, **Co₂2** (Fig. 1.8) that affords CO with TON of 16896 and TOF of 0.47 s⁻¹ under 450 nm LED light irradiation for 10 hours (Table 1.2, entry 12).⁴⁷ Compared with the corresponding monomer which gave a turnover number for CO and selectivity of 1600 and 85%, respectively, in 10 hours, a possible

explanation has been brought up according to experimental data and DFT calculations. It has been concluded that the two cobalt atoms work synergistically in the photocatalytic process, where one Co acts as the catalytic center to remove OH group.

Then, a related dinuclear complex obtained from replacing one of the Co centers by Zn ([CoZn(OH)L](ClO₄)₃ **CoZn1**, Fig. 1.8) was reported by the same group. The catalytic efficiency of this heterobimetallic complex (**CoZn1**) was significantly improved to a TON of 65000 and a TOF of 1.8 s⁻¹ (Table 1.2, entry 13).⁴⁸ The superior photocatalytic performance can be ascribed to enhanced dinuclear metal synergistic catalysis effect between Co^{II} and Zn^{II}. With a stronger binding affinity to OH⁻, Zn^{II} can facilitate the cleavage of C–O in O=C–OH intermediate, Reducing the activation barrier.

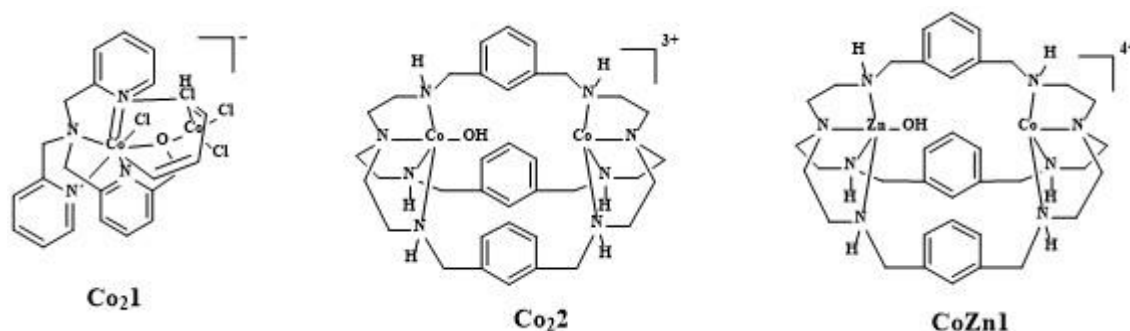


Fig. 1.8 Molecular structures of cobalt-containing dinuclear complexes.

In addition, some multimetallic complexes such as **Fe₂1**, **Cu₂1**, **Cu₂2**, and **Fe₄1-Fe₄3** (Fig. 1.7) also exhibit good activity in electrochemical catalytic carbon dioxide reduction reactions.

1.5 Supported molecules CO₂ reduction catalysts

Compared to inorganic materials, molecular catalysts are usually characterized by a relatively mediocre stability, non-recyclability, and the need for both electron donors and photosensitizers limit their practical applications.⁵¹

Appending molecular catalysts to inorganic matrices has recently become a research hotspot since it may overcome the above shortcomings, at least partially. For example,

these supported molecular catalysts show promising activity in photocatalytic reduction of CO₂.⁵² It is worth mentioning that recently some inorganic materials with atomically dispersed catalytic metal sites have been synthesized.⁵³ Such systems share with appended molecular catalysts the possibility to fine tune the environment at the metal-binding site, but with a higher degree of electronic conjugation between the metal and the supporting matrix.

Supported molecular catalysts can be obtained through a variety of linkage strategies. A first type is through non-covalent grafting, which mainly includes simple physical mixing and *in-situ* growth of complexes on matrices. A second type is through covalent grafting *via* a covalent bond between the inorganic material and the molecular catalyst. This can also be extended to conjugated grafting which utilizes aromatic structures with faster electron transport.

The selection of supporting substrate also requires careful consideration to minimize undesirable characteristics of the hybrid, such as resistive electron transfer towards the catalyst, occurrence of side reactions, and instability of the heterogeneous catalyst in different reaction conditions. On one hand, semiconductors, including carbon-based materials as well as metal chalcogenides and metal oxides (TiO₂ and ZrO₂),⁵⁴⁻⁵⁷ have been extensively used in constructing heterogeneous electro- and photocatalysts. In these catalytic systems, the semiconductor works as photosensitizer, as co-catalyst and/or as an electronic conductor. On another hand, scaffolds such as inorganic materials (metal-organic frameworks (MOFs), covalent organic frameworks (COFs)) or carbon-based materials (*e.g.* single or multiwall carbon nanotubes, graphene or fullerene), can be used both as conductive support and as platform for molecular immobilization.

In general, supported molecule catalysts can be divided into three parts: (i) the catalytic center — molecular complex, (ii) the anchoring group on the surface of the material which can achieve the chemisorption of molecules, and (iii) a linker to permit electron transfer. During the catalysis, the size and the electronic inductive effect

(electron-withdrawing or -donating) of the ligand linker will both affect spatial and electronic properties of the catalyst by adjusting electron transfer kinetics, which may trigger significant changes in the overpotential required in catalytic activity. Because the electron transfer between the surface and the catalyst proceeds either “through-bond” (*via* the linker orbitals) or “through-space” (*via* direct orbital overlap or superexchange).⁵⁸

1.5.1 Hybrid catalysts assembled by non-covalent effect

The simplest approach to modify inorganic material is absorbing or grafting molecules to scaffold matrices, such as silicon, zeolite, kaolin. One strategy successfully combined $[\text{Mn}(\text{CO})_5\text{Br}]$ with bipyridyl-containing periodic mesoporous silica (**bpy-PMO**, Fig. 1.9), while Mn-carbonyl centers coordinated to the bipydine functionalities. With the help of $[\text{Ru}(\text{bpy})_3]\text{Cl}_2$ and BIH, the obtained hybrids catalyst triggered a CO_2 reduction towards CO with a TON of 239 or towards formate with a TON of 484, respectively.⁵⁹

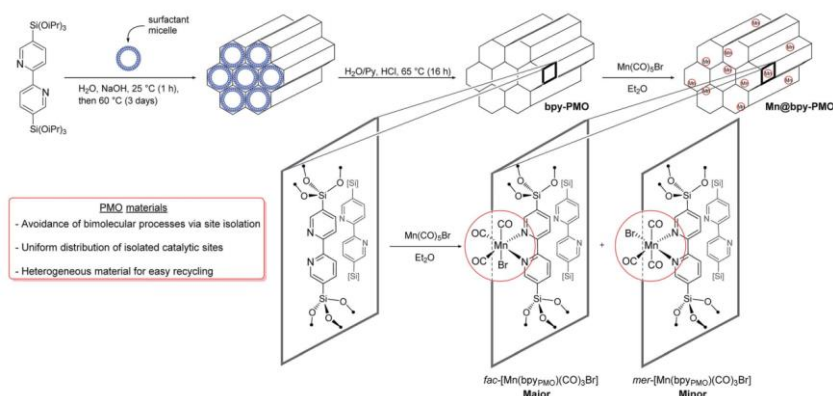


Fig. 1.9 Synthetic pathway to $[\text{Mn}(\text{bpyPMO})(\text{CO})_3\text{Br}]$. Reproduced from ref.59⁵⁹ with permission from The Royal Society of Chemistry.

In the case of carbon material derivatives, noncovalent strategies are mainly employed in carbon materials through π - π stacking or hydrophobic interactions, allowing the intrinsic properties of the substrate to be maintained during the chemical synthetic process.⁶⁰⁻⁶⁴

In another example, a polymeric cobalt phthalocyanine (**Co6**, CoPPc) was coupled with mesoporous carbon nitride (mpg- CN_x) through *in situ* polymerization (Fig. 1.10).⁶⁵ In CH_3CN solution with TEOA as electron donor, CO was generated with a TON of 84

and a selectivity of 85% under full solar spectrum irradiation (> 300 nm), whereas under visible light, $\text{TON}_{\text{CO}} = 51$ and selectivity decreased to 76% with identical catalyst loading.

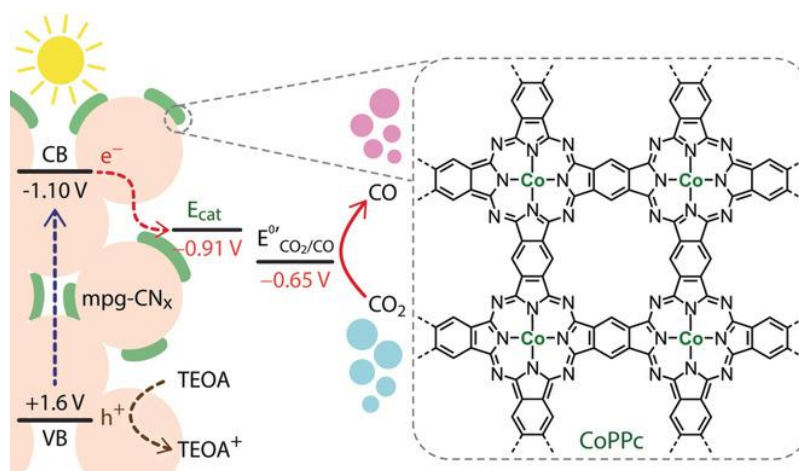


Fig. 1.10 Schematic illustration of light-driven CO_2 reduction catalyzed by $\text{mpg-CN}_x|\text{CoPPc}$ hybrid (potentials reported vs. NHE; VB and CB denote valence and conduction band, respectively). Adapted with permission from ref. 65, copyright © 2019 The Authors. Published by Wiley-VCH Verlag GmbH & Co. KGaA.

1.5.2 Hybrid catalysts assembled by covalent bonds

As discussed above, the hybridization of carbon materials is usually achieved derivatization sp^2 carbon on the surface before hybridizing with molecules. One of the functionalizing method is to generate reactive functional groups by applying strongly chemically or electrochemically oxidation to create ketones, quinones, or carboxylic acid groups.⁶⁶⁻⁶⁹ For example, surface carboxyl groups and *ortho*-quinone can be linked to molecules through amide/ester bonds and the formation of pyrazine, respectively. However, Control of the oxidation process is difficult and it may lead to unexpected changes in the physical properties (such as conductivity and stability) of the material due to the formation of defects.

Reisner et al. have used a nickel terpyridine and phosphonic acid-functionalized Ni (cyclam) (**Ni1**, Figure 1.4) to garft with CdS QDs and ZnSe QDs, respectively. And these molecule supported catalyst can convert CO_2 to CO in aqueous solution, although with a low selectivity and modest stability ($\text{TON}_{\text{CO}} = 121$, selectivity 8% after 20 hours)⁷⁰

An interesting strategy associating polymeric carbon nitride (PCN) with cobalt bipyridine [$\text{Co}(\text{bpy})_3^{2+}$] was followed through the formation of in molecular junctions with 2,2' -biisonicotinic acid (BINA), and it led to interfacial electron transfer (Fig. 1.12).⁷¹ The binary photocatalyst [$\text{Co}(\text{bpy})_3^{2+}/\text{BINA}_2\text{-CN}$] showed photocatalytic activity for H_2 and CO_2 reduction with a rate of $8.8 \mu\text{molh}^{-1}$ and $8.1 \mu\text{molh}^{-1}$, respectively. While the rates with samples obtained by physical mixing of $\text{Co}(\text{bpy})_3^{2+}$ and PCN were 12.5 and 16 times smaller than that of binary photocatalysts, respectively.

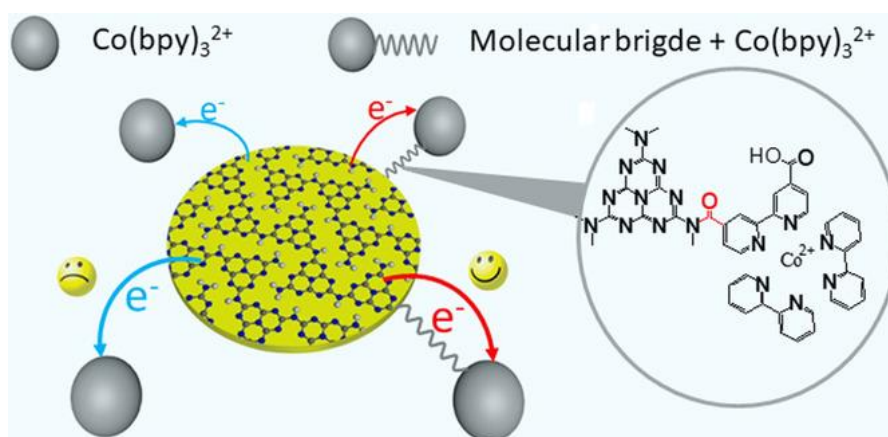


Fig 1.12 Schematic representation of the two different interfacial ET methods in the PCN and $\text{Co}(\text{bpy})_3^{2+}$ system connected by a covalent linker (2,2' -biisonicotinic acid, BINA). Adapted with permission of ref. 71. Copyright © 2020 The Authors. Published by Wiley-VCH Verlag GmbH & Co. KGaA.

Surendranath *et al.* reported a supported catalyst made of cobalt porphyrins strongly electronically coupled to carbon electrodes by condensing diaminoporphyrin derivatives onto o-quinone moieties native to graphitic carbon surfaces (Fig. 1.13). Probing the material for O_2 reduction reaction (ORR), it was found that the graphite-conjugated Co porphyrin, GCC-CoTPP, displays an onset current density of $10 \mu\text{A}/\text{cm}^2$ at 0.72 V vs. RHE , whereas a nonconjugated amide linked Co porphyrin gives an onset at 0.66 V vs. RHE , which illustrates that conjugation significantly enhances the rate of catalysis.⁷²

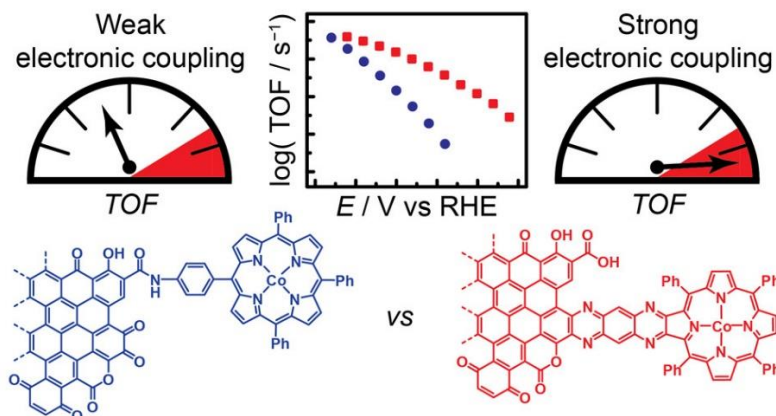


Figure 1.13 Scheme of two different graphite-conjugation porphyrin system. Adapted with permission of ref. 72. Copyright © 2019, American Chemical Society.

These observation highlights the importance of controlling the connection between solid materials and molecular catalysts to accelerate the interfacial charge-carrier mobility and, consequently, improve the photocatalytic activity.

1.6 Motivation and outline of the thesis

Unlike hydrogen production which has been widely studied, there is still a long way to go in the research on CO₂ reduction into useful compounds. Molecular catalysts have significant advantages in terms of activity and selectivity, which are worth digging deeply. In particular, the photocatalytic CO₂ reduction with molecular catalysts takes its inspiration from natural photosynthesis to give rise to an artificial analog. Studying the activity and mechanisms of the processes generating energy-rich substances is a crucial step for the development of an alternative to fossil energy.

Few work has been devoted to multimetallic complexes. In addition, hybrid systems, combing active molecular catalysts and absorbing photo materials have been equally barely investigated, although such systems would be interesting in view of developing devices. My work aims to contribute filling in these two gaps.

Chapter 2 will describe a new bimetallic (Co-Co) biquaterpyridine complex for the photoreduction of CO₂ towards CO or formate. We will show that metal cooperativity is a key to the reactivity.

Chapter 3 will describe two Cobalt-quaterpyridine supported photocatalysts grafted on semiconducting carbon nitride and graphitic acid, respectively.

Chapter 4 will discuss preliminary results obtained preliminary studies on a graphite-conjugated cobalt catalyst for electrochemical carbon dioxide reduction.

Chapter 5 will give a brief summary of the completed work, with an overview of ongoing projects.

Chapter 6 will describe the experimental methods including chemicals, material synthesis and various characterization techniques.

Chapter 2 - Homogeneous photochemical reduction of CO₂ under visible light with dinuclear complexes

Multi-metallic complexes as catalytic centres of metalloenzymes ubiquitously exist in nature, which inspiring us to design of bimetallic complexes as catalysts for CO₂ reduction. One prominent example is the Ni–Fe-based carbon monoxide dehydrogenases (CODHs) that reversibly transform CO₂ into CO. In these enzymes, a Ni^I centre binds to the C atom of the CO₂ while a Fe^{II} binds to one O atom, playing the role of a Lewis acid to assist cleavage of the C–O bond.^{73, 74} Previous studies have fully demonstrated that the two metals act in synergy for high selectivity. However, only a few reported examples of molecular multimetallic catalysts can efficiently mimic the enzymatic CO₂ reduction.^{47, 75, 76}

Since the 1996 report from Constable about the successful synthesis of 2, 2':6,2''-quaterpyridine (qpy) ligand,⁷⁷ transition metal complexes with this ligand as molecular catalysts have been extensively studied.^{78, 79} For CO₂ reduction reaction, both homogeneous and heterogeneous catalysis in photocatalysis and electrocatalysis have been reported.^{22, 80, 81}

In this chapter, we will report a binuclear cobalt complex bearing a bi-quaterpyridine ligand which can selectively reduce CO₂ to formate or CO under visible light in ACN solution. Sensitized by a ruthenium complex, by an organic compound, or by carbon nitride, electron transport from PS to CAT can be completed and result in high product selectivity. In basic ACN solution, the selectivity of formate evolution can reach a maximum of 97% with a TON of up to 821. Replacing a base (such as TEOA) with a weak acid (such as phenol), CO becomes the dominant product with high selectivity (maximum of 99%) and a maximum TON of 829. Applying cyclic voltammetry, spectro-electrochemistry (SEC), together with DFT calculations, a catalytic mechanism has been proposed, highlighting that the two cobalt in the binuclear complex are not completely

independent but act synergistically to complete the conversion of CO₂-to-CO or CO₂-to-formic acid, and the reactivity can be steered towards the desired product by simply changing the acid co-substrate.

2.1 Quaterpyridine complexes in homogeneous conditions

The complex was first reported in a homogeneous solution for the visible-light-driven photocatalytic CO₂ reduction reaction. In a mixed solution of acetonitrile and TEOA, using BIH as sacrificial donor and Ru(bpy)₃²⁺ as photosensitizer, iron quaterpyridine was shown to catalyze the reduction of CO₂ to CO with a TON_{CO} of 2660 and a selectivity of 98%.⁸² Copper quaterpyridine exhibited even higher catalytic activity. In the same conditions than the previous example, with the addition of 3% (v/v) water, a high TON_{CO} of 12400 has been reached with a selectivity of 97%.⁸⁰ When the photosensitizer is replaced by organic dye purpurin, Feqpy and Coqpy can reach TON_{CO} of 1365 (92%) and 790 (95%) in DMF solution, respectively.

Besides reduction of CO₂, Coqpy can also serve as visible-light-driven catalysts for both water reduction (*e.g.* hydrogen evolving reaction, HER) and oxidation (*e.g.* oxygen evolving reaction, OER). Under monochromatic visible-light irradiation ($\lambda = 457$ nm), Coqpy can complete OER in aqueous solution of Ru(bpy)₃²⁺ and S₂O₈²⁻ (pH = 8), with a TON_{O₂} of 335. While under larger visible-light irradiation ($\lambda > 420$ nm), Coqpy can catalyze HER in mixed solution of H₂O/ACN with [Ir^{III}(dF(CF₃)ppy)₂(dtbbpy)]⁺ / TEOA with a max TON_{H₂} of 1730.⁷⁹

Fe- and Co- quaterpyridine complexes can also achieve electrochemical CO₂-to-CO conversion in the presence of weak Brønsted acids. For example with phenol, CO₂ reduction occurs at an overpotential as low as 140 mV with Coqpy, while the catalyst keeps active over hours of bulk electrolysis.⁸³ In the case of Feqpy, CO can be afforded in the presence of phenol with a selectivity of 95% at an overpotential of 240 mV. Although the molecular catalyst is not stable after hours of bulk electrolysis, cyclic voltammetry studies, spectroelectrochemistry, controlled-potential electrolysis as well as

DFT calculations have been employed to unveil the catalytic mechanisms. Based on these studies, Robert *et al.* speculated the contrasting catalytic pathways and gave a prediction on the modification direction of the ligand and the promising catalytic performance.

2.2 Quaterpyridine complexes in supported conditions

Cometto *et al.* have employed Feqpy for heterogeneous photocatalysis together with semiconductor mesoporous carbon nitride as light absorber. In a mixed solution of acetonitrile and TEOA, a TON of 155 for CO evolution has been achieved with 97% selectivity and an apparent quantum yield of *ca.* 4.2%.⁸⁴

Wang *et al.* have reported a Co(qpy) appended at the surface of multi-walled carbon nanotubes, which can convert CO₂ into CO in water at pH 7.3 with 100% catalytic selectivity and 100% faradaic efficiency, at low catalyst loading and at reduced overpotential. Electrolysis at 340 mV overpotential indeed showed a stable current density of 9.3 mAcm² and excellent catalytic performances (89095 catalytic cycles in 4.5 h).⁸¹

2.3 Selective reduction of CO₂-to-CO or to-formate through metal synergy

Known molecular catalysts include noble metal complexes such as Ru^{85, 86}, Ir⁸⁷ and Re⁸⁸ and earth-abundant metal complexes such as Co⁸⁹, Ni⁹⁰, Fe²⁹, Mn⁹¹ and Cu⁹². Among all earth-abundant molecular photocatalysts reported to date, most of them can obtain CO from CO₂ while few of them can produce HCOO⁻ with high yield, and there are even fewer examples of complexes which can generate hydrocarbons beyond these 2H⁺/2e⁻ reduction reactions.^{32, 33, 93} Even if CO is indeed a useful chemical, for example in the Fischer–Tropsch reaction, HCOOH has recently attracted some attention as a hydrogen storage substrate which can be employed in liquid formic acid fuel cells, or as feedstock for bacteria to produce alcohols as liquid fuels.⁹⁴

The mononuclear [Co(qpy)]²⁺ (qpy=2,2':6',2'':6'',2''':6''',2''''-quaterpyridine) has been shown as an efficient and selective catalyst for both photo- and electrocatalytic reduction of

CO₂.⁸² The product is predominately CO (selectivity > 98%), with only trace amounts of formate or H₂. Although other Co-based²⁰ and Fe-based²² molecular catalysts are able to generate formate, the selectivity or yield is very low. Mn-based diamine complexes have resulted in improved catalytic activity, together with a complex *fac*-Mn(bpy)(CO)₃Br (bpy=2,2'-bipyridine) which converts CO₂ to formic acid with a TON of 149 and a selectivity of 85% in DMF/TEOA with BIH as a sacrificial reductant.⁹⁵ A similar system catalyzed by *fac*-Mn(CN)(bpy)(CO)₃ illustrates that the product selectivity is related to the nature of solvent⁹¹. The HCOOH/CO ratio is 18 and 0.42 in DMF/TEOA and ACN/TEOA, respectively.

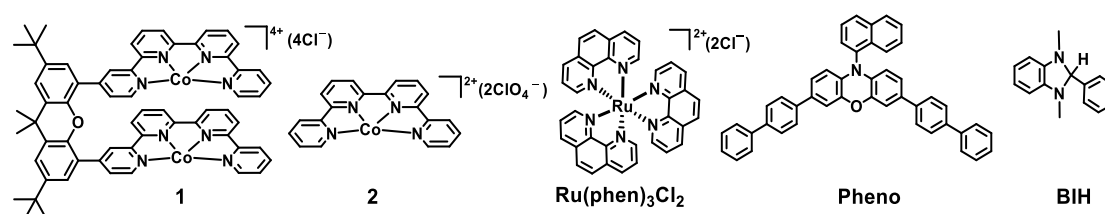


Fig. 2.1 Structure of compounds used in this chapter. Cobalt complexes [Co₂(biqpy)]⁴⁺ (**1**) and [Co(qpy)]²⁺ (**2**), molecular sensitizers ([Ru(phen)₃]²⁺, Pheno) and sacrificial reductant BIH.

2.3.1 Photocatalytic performance for CO₂ reduction

During the photochemical reduction of CO₂, formate could be selectively and efficiently produced in the absence of additional acid. Conversely, when phenol was used as a co-substrate, the selectivity is switched from formate to CO. It appears that [Co₂biqpy]⁴⁺ is a highly efficient and selective molecular catalyst for the visible-light-induced reduction of CO₂, with two cooperative metals controlling catalytic activity and selectivity.

a. Visible-light-driven reduction of CO₂ into formate.

Photocatalytic CO₂ reduction experiments were initially performed in a three-component system containing **1** (Fig. 2.1) as a catalyst, Ru(phen)₃Cl₂ (phen=1,10-phenanthroline) as photosensitizer, BIH as sacrificial donor and ACN as solvent. Ru(phen)₃Cl₂ was employed since of [Ru(phen)₂(H₂O)₂]²⁺ was photochemically inactive

due to the photolabilization of the phen ligand of $[\text{Ru}(\text{phen})_3]^{2+*}$. Note that $[\text{Ru}(\text{bpy})_2(\text{H}_2\text{O})_2]^{2+}$ originated from the decomposition of $[\text{Ru}(\text{bpy})_3]^{2+*}$ may be itself a catalyst for CO_2 reduction. Regarding the solvent, DMF was not used because it can produce some formate during photocatalysis through hydrolysis, especially in the presence of trace amounts of amine or water,^{96, 97} thus ACN was preferred.

Triethylamine (TEA) was first used as electron donor. In a typical run, a glass flask containing a mixture of 2 mL of CO_2 -saturated ACN, **1** (0.05 mM), $\text{Ru}(\text{phen})_3\text{Cl}_2$ (0.2 mM) and TEA (20% vol) was irradiated using a blue light-emitting diode (LED) strip (460 nm) at 24°C.

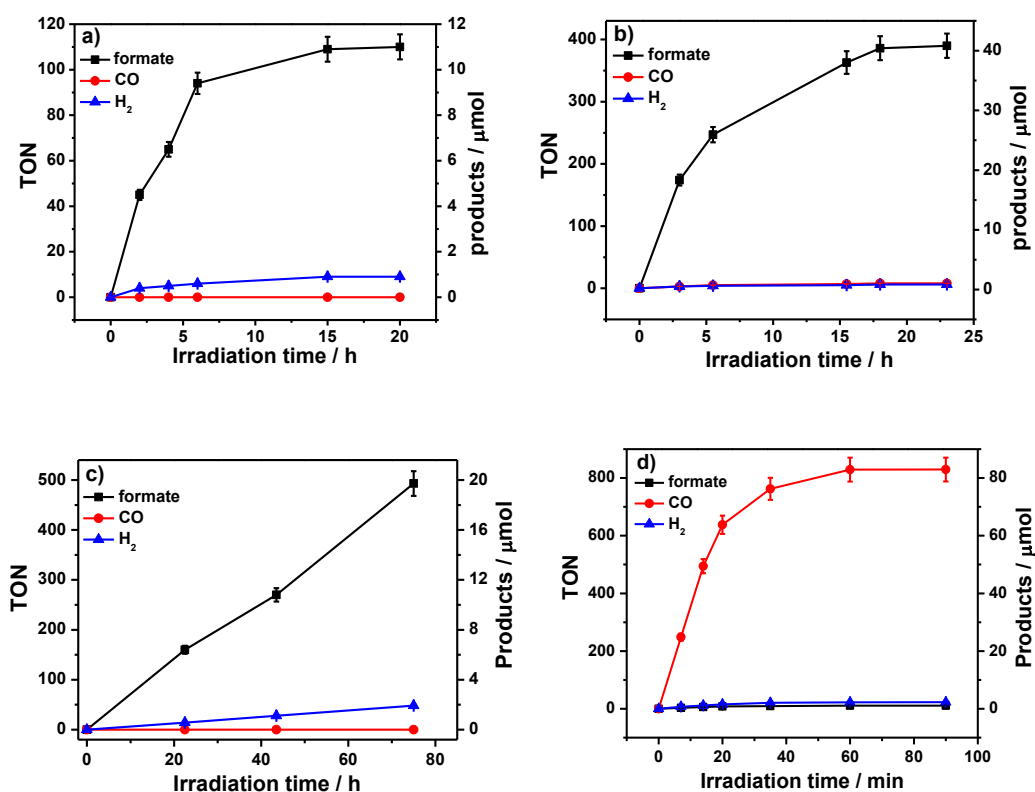


Fig. 2.2 Evolution with time of CO_2 reduction products during photochemical experiments. performed in a CO_2 -saturated ACN solution (a) in the absence and (b) presence of 0.025 M BIH for a solution containing 50 μM **1**, 0.2 mM $\text{Ru}(\text{phen})_3\text{Cl}_2$ and 20% TEA ($\lambda = 460$ nm); (c) with 20 μM **1**, 2.5 mg $g\text{-C}_3\text{N}_4$, 20% TEOA and 0.05 M BIH ($\lambda > 400$ nm); (d) with 50 μM **1**, 0.2 mM $\text{Ru}(\text{phen})_3\text{Cl}_2$, 0.1 M BIH and 1 M PhOH ($\lambda = 460$ nm). Adapted with permission from ref.⁴⁹ Copyright © 2019, Springer Nature.

Table 2.1 Photoinduced CO₂ catalytic reduction with catalyst **1** and [Ru(phen)₃]²⁺ or Pheno or g-C₃N₄ as photosensitizer.^a

Entry	Sensitizer	conditions	Time (h)	TON (selectivity, %)		
				HCOO ⁻	CO	H ₂
1	[Ru(phen) ₃] ²⁺	TEA	20	110 (92.4)	0 (0)	9 (7.6)
2	[Ru(phen) ₃] ²⁺	TEA+BIH	23	386 (96.5)	8 (2)	6 (1.5)
3	[Ru(phen) ₃] ²⁺	TEOA+BIH	60	821 (75.9)	221 (20.4)	40 (3.7)
4	g-C ₃ N ₄	TEOA+BIH	75	493 (91.1)	0 (0)	48 (8.9)
5	Pheno	TEOA+BIH	5	565 (58.3)	284 (29.3)	119 (12.4)
6	[Ru(phen) ₃] ²⁺	PhOH+BIH	1	12 (1.5)	829 (96)	22 (2.5)
7	Pheno	PhOH+BIH	2.5	0 (0)	518 (89.3)	62 (10.7)

^a in a typical run, 2 mL of CO₂-saturated ACN solution containing **1** (50 μM [entries 1, 2, 3, 6], 20 μM [entry 4], 15 μM [entries 5, 7]), Ru(phen)₃Cl₂ (0.2 mM) or Pheno (0.4 mM) or g-C₃N₄ (2.5 mg), TEA (20%, v%) or TEOA (20%, v%), BIH (0.025 M [entry 2], 0.05 M [entries 4, 5, 7], 0.1 M [entries 3,6]), PhOH (1 M) was irradiated using blue LED (460 nm, entries 1-3, 6) or with a lamp equipped with a 400 nm optical filter (Xe-Hg lamp for entry 4, solar simulator [entries 5, 7]). TON values are ± 5%.

As shown in Fig. 2.2 and Table 2.1 (entry 1), formate was produced with a TON of 110 and selectivity of 92% with traces of H₂ (TON of 9) obtained (Fig. 2.2a). Only H₂ (TON of 22) was generated under Ar, while no products were detected in the absence of catalyst (Table 2.2, entries 2 and 3) as well as when the non-metallated ligand was used instead of **1** (Table 2.2, entry 8). Note that the amount of formate using **2** as catalyst was only about one-third of that with **1** (Fig. 2.3 and Table 2.3, entry 1).

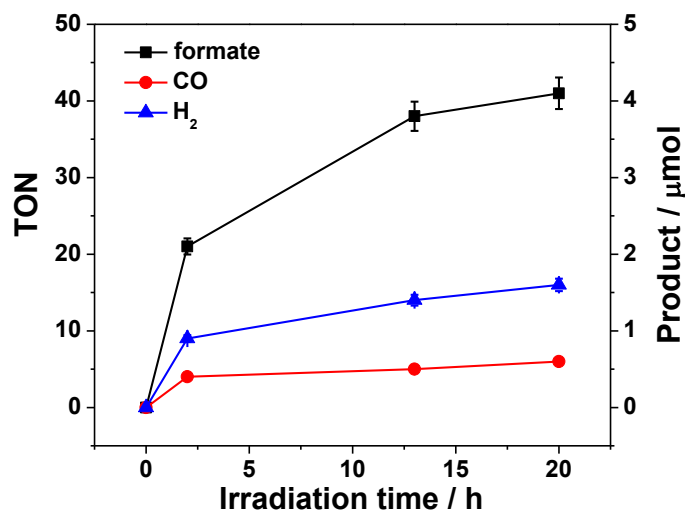


Fig. 2.3 Photocatalytic CO₂ reduction performance with time for the CO₂-saturated ACN solution containing 0.05 mM **2**, 0.2 mM Ru(phen)₃Cl₂ and 20 % (v %) TEA. The Data points are resulting from two to four runs, and error bars represent the standard error on the mean. Adapted with permission from ref. ⁴⁹

Copyright © 2019, Springer Nature.

When catalyst was replaced by a cobalt salt, namely CoCl₂, neither formate nor CO was detected after irradiation for 23 h (Table 2.2, entry 7), indicating that the catalytic activity is not result from demetallation of the Coqpy. With additional BIH as an efficient two-electron donor, catalytic performances could be optimized further. In the presence of 0.025 M BIH, the TON and selectivity for formate were boosted to 386 and 96.5% respectively (Fig. 2.2b and Table 1, entry 2). Only trace amounts of CO and H₂ were obtained (TONs of 8 and 6 for CO and H₂, respectively). Control experiments conducted under Ar only gave trace amounts of formate (TON of 7) and H₂ (TON of 1), while a negligible amount of formate was detected in the absence of catalyst. The TON for formate could be further increased to 821 when TEA/BIH was replaced by TEOA/BIH (Fig. 2.4 and Table 1, entry 3). However in this case the selectivity for formate then dropped to 75.9% while more CO and H₂ were produced (TON_{CO} of 221 and TON_{H₂} of 40).

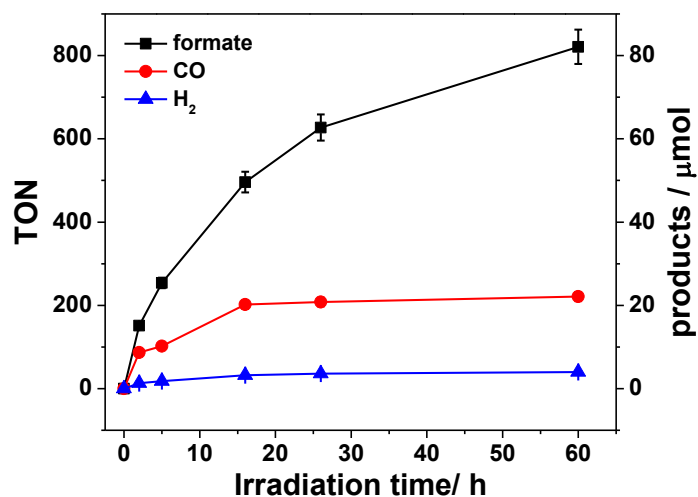


Fig. 2.4 Photocatalytic CO₂ reduction performance for CO₂-saturated ACN solution containing 0.05 mM **1**, 0.2 mM Ru(phen)₃Cl₂, 20 % (v/v) TEOA and 0.1 M BIH. Data points are resulting from two to four runs, and error bars represent the standard error on the mean. Adapted with permission from ref. ⁴⁹ Copyright © 2019, Springer Nature.

Table 2.2. Photoinduced CO₂ catalytic reduction with catalyst **1** and [Ru(phen)₃]²⁺ or Pheno or g-C₃N₄ as photosensitizer.^a

Entry	Sensitizer	Conditions	Time (h)	TON		
				HCOO ⁻	CO	H ₂
1	[Ru(phen) ₃] ²⁺	TEA	20	110	0	9
2 ^b	[Ru(phen) ₃] ²⁺	TEA	20	0	0	22
3 ^c	[Ru(phen) ₃] ²⁺	TEA	20	--	--	--
4	[Ru(phen) ₃] ²⁺	TEA+BIH	23	386	8	6
5 ^b	[Ru(phen) ₃] ²⁺	TEA+BIH	23	7	0	1
6 ^c	[Ru(phen) ₃] ²⁺	TEA+BIH	23	--	--	--
7 ^d	[Ru(phen) ₃] ²⁺	TEA+BIH	23	0	0	0
8 ^e	[Ru(phen) ₃] ²⁺	TEA+BIH	23	0	5	1
9	[Ru(phen) ₃] ²⁺	TEOA+BIH	60	821	221	40
10 ^b	[Ru(phen) ₃] ²⁺	TEOA+BIH	60	7	0	3
11 ^c	[Ru(phen) ₃] ²⁺	TEOA+BIH	60	--	--	--
12	Pheno	TEOA+BIH	5	565	284	119
13 ^b	Pheno	TEOA+BIH	5	0	0	34
14 ^c	Pheno	TEOA+BIH	5	0	0	--
15 ^d	Pheno	TEOA+BIH	5	0	15	95
16 ^f	Pheno	BIH	2.5	0	518	62
17 ^{b,f}	Pheno	BIH	2.5	0	0	59
18 ^{c,f}	Pheno	BIH	2.5	0	0	--
19 ^{d,f}	Pheno	BIH	2.5	0	0	0
20 ^{f,g}	Pheno	BIH	2.5	0	380	4
21 ^{b,f,g}	Pheno	BIH	2.5	0	0	29
22 ^{c,f,g}	Pheno	BIH	2.5	0	--	--
23 ^{d,f,g}	Pheno	BIH	2.5	0	27	0.2
24	g-C ₃ N ₄	TEOA	60	525	107	73
25 ^b	g-C ₃ N ₄	TEOA	60	0	0	3
26 ^c	g-C ₃ N ₄	TEOA	60	--	--	--
27 ^d	g-C ₃ N ₄	TEOA	60	0	0	1
28 ^e	g-C ₃ N ₄	TEOA	60	0	0	19
29	g-C ₃ N ₄	TEOA+BIH	75	493	0	48
30 ^b	g-C ₃ N ₄	TEOA+BIH	75	20	0	12.5
31 ^c	g-C ₃ N ₄	TEOA+BIH	75	--	0	--
32 ^d	g-C ₃ N ₄	TEOA+BIH	75	0	16	13
33	g-C ₃ N ₄	TEOA+BIH	84	67	0	6
34 ^f	Ru(phen) ₃ ²⁺	BIH	1	12	829	22
35 ^{b,f}	Ru(phen) ₃ ²⁺	BIH	1	0	0	100
36 ^{c,f}	Ru(phen) ₃ ²⁺	BIH	1	--	--	--
37	Ru(phen) ₃ ²⁺	BIH	4	4	88	1

^a in a typical run, in 2 mL of CO₂-saturated ACN solution containing **1** (50 μM [entries 1, 2, 4, 5, 9, 10, 34,35,37], 20 μM [entries 24, 25, 29, 30, 33], 15 μM [entries 12, 13, 16, 17, 20, 21]), Ru(phen)₃Cl₂ (0.2

mM) or Phen (0.4 mM in entries 12-19, 1 mM in entries 20-23) or g-C₃N₄ (2.5 mg), TEA (20%, v%) or TEOA (20%, v%), BIH (0.025 M [entries 4-8], 0.05 M [entries 29-33, 12-23], 0.1 M [entries 9-11, 34-37]) was irradiated using blue LED (460 nm, entries 1-11, 33, 34-36) or with a lamp equipped with a 400 nm optical filter (Xe-Hg lamp [entries 24-32], solar simulator [entries 12-23]). TON values are $\pm 5\%$.

^b: under Ar

^c: without catalyst

^d: CoCl₂ (0.05 mM for 7, 0.02 mM for 27 and 32, 0.015 mM for 15, 19, 23) as catalyst

^e: biqpy (0.05 mM for 8, 0.02 mM for 28) as catalyst

^f: in the presence of 1 M PhOH

^g: in DMF as solvent

Table 2.3 Photoinduced CO₂ catalytic reduction with catalyst **2** with Ru(phen)₃Cl₂ or g-C₃N₄ as photosensitizer.^a

Entry	Sensitizer	Electron donor	Time/h	TON (selectivity, %)			Yield (μmol)		
				HCOO ⁻	CO	H ₂	HCOO ⁻	CO	H ₂
1	[Ru(phen) ₃] ²⁺	TEA	20	41(65)	6(10)	16(25)	4.1	0.6	1.6
2	[Ru(phen) ₃] ²⁺	TEA+BIH	16	96(72)	33(25)	5(3)	9.6	3.3	0.5
3 ^b	[Ru(phen) ₃] ²⁺	TEA+BIH	16	5(71)	0	2(29)	0.5	0	0.2
4 ^c	[Ru(phen) ₃] ²⁺	TEA+BIH	23	--	--	--	0.2	0	0
5	[Ru(phen) ₃] ²⁺	TEOA+BIH	16	171(42)	166(41)	71(17)	17.1	16.6	7.1
6	g-C ₃ N ₄	TEOA	75	160(55)	54(19)	75(26)	6.4	2.2	3
7	g-C ₃ N ₄	TEOA+BIH	81	200(68)	52(18)	40(14)	8	2.1	1.6

^a In a typical run, 2 mL of CO₂-saturated ACN solution containing **2** (50 μM [entries 1-3, 5], 20 μM [entries 6-7]), Ru(phen)₃Cl₂ (0.2 mM) or g-C₃N₄ (2.5 mg), TEA (20%, v%) or TEOA (20%, v%), and BIH (0.025 M [entries 2-4], 0.1 M [entry 5], 0.05 M [entry 7]) was irradiated using blue LED (460 nm, entries 1-5) or 400 W Xe-Hg lamp equipped with a 400 nm optical filter (entries 6-7) at 24 °C. TON values are $\pm 5\%$.

^b: under Ar.

^c: without catalyst.

Under optimized photocatalytic conditions (Fig. 2.2), a dynamic light scattering (DLS) experiment ruled out the possibility of particle existence (Fig. 2.5), in line with a mercury poisoning test illustrating that the photocatalytic system is mainly homogeneous (Fig. 2.6). The ESI-MS spectrum of the product solution for isotope labelling experiments, *i.e.* when saturating the solution with ¹³CO₂, led to H¹³COO⁻ formation, verifying that formate is generated from CO₂ reduction exclusively (Fig. 2.7). As can be seen from Fig. 2.2b, catalysis stopped after 18 h. Upon re-addition of **1**, Ru(phen)₃Cl₂ or TEA to the inactive solution, only 5%, 21% and 22% of the catalytic activity was restored,

respectively. However, 91% of activity could be recovered on adding BIH, indicating that the loss of activity is mainly due to the consumption of the sacrificial agent BIH (Fig. 2.8). Finally, the quantum yield for formate production was determined to be 2.6% from ferrioxalate actinometry (at $\lambda = 460$ nm).

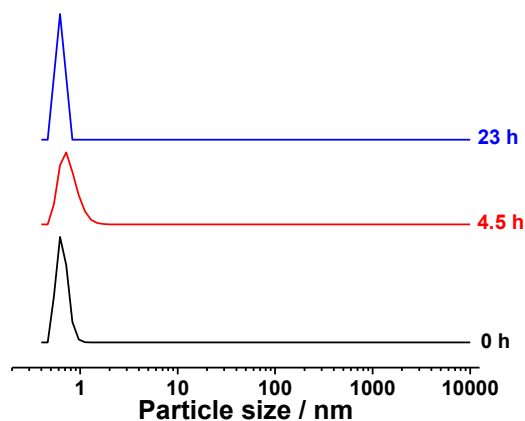


Fig. 2.5 Particle size distribution of CO₂-saturated ACN/TEA (4:1, v:v) solution containing 0.05 mM **1**, 0.2 mM Ru(phen)₃Cl₂ and 0.025 M BIH determined by DLS during irradiation by blue LED. Adapted with permission from ref. ⁴⁹ Copyright © 2019, Springer Nature.

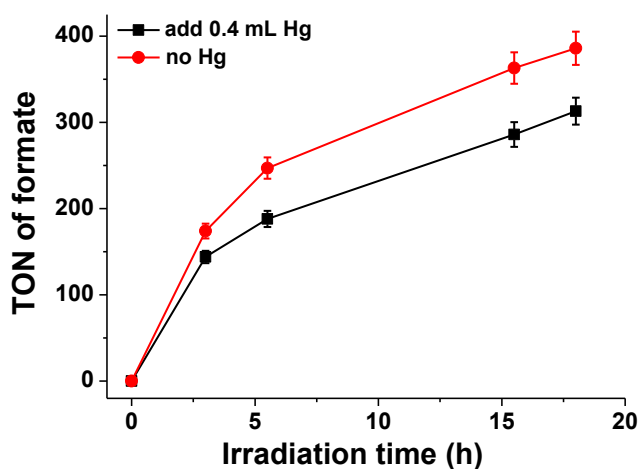


Fig. 2.6 Photocatalytic CO₂ reduction performance in the presence and absence of 0.4 mL Hg in CO₂-saturated ACN/TEA (4:1, v:v) solution containing 0.05 mM **1**, 0.2 mM Ru(phen)₃Cl₂ and 0.025 M BIH. The error bars represent the standard error on the mean, which was calculated from two to four runs. Adapted with permission from ref. ⁴⁹ Copyright © 2019, Springer Nature.

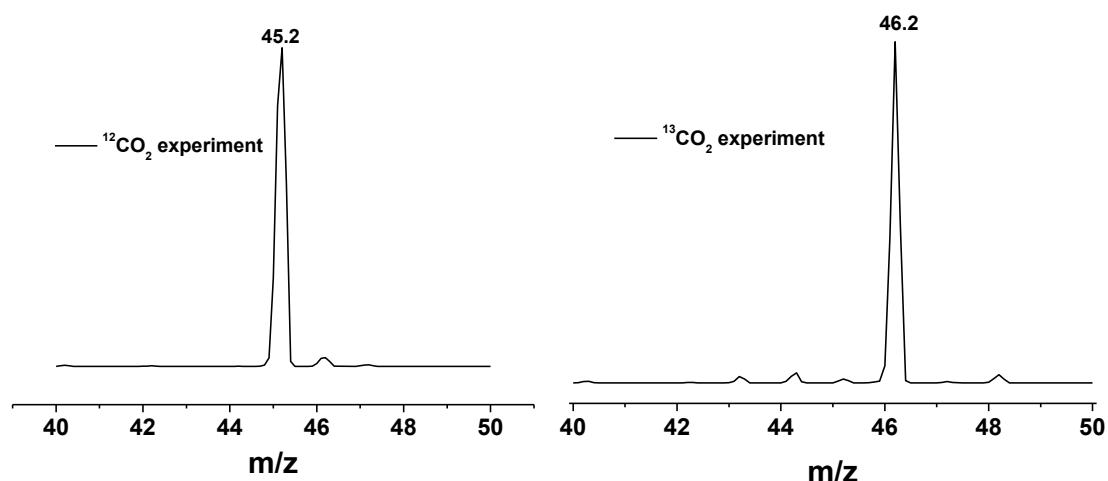


Fig. 2.7 ESI-MS of solution product for $^{12}\text{CO}_2$ or $^{13}\text{CO}_2$ -saturated ACN/TEA (4:1, v:v) solution containing 0.05 mM **1**, 0.2 mM $\text{Ru}(\text{phen})_3\text{Cl}_2$ and 0.025 M BIH. The peaks at m/z 45.2 and 46.2 are assigned to $\text{H}^{12}\text{COO}^-$ and $\text{H}^{13}\text{COO}^-$ respectively. Adapted with permission from ref. ⁴⁹ Copyright © 2019, Springer Nature.

b. Photochemical experiments with non-metallic sensitizers (Pheno, $g\text{-C}_3\text{N}_4$).

The expensive and rare Ru-based sensitizers could suitably be replaced by an organic dye as well as by the semiconducting $g\text{-C}_3\text{N}_4$. For example, the organic chromophore Pheno (Fig. 2.2), which is based on a phenoxazine motif, was used as a sensitizer thanks to its excellent photon absorption in the visible region, its high triplet quantum yield combined with a long triplet lifetime, as well as redox reversibility and strong reducing ability (the triplet state excited standard reduction potential $E^0(^2\text{Pheno}\bullet+/^3\text{Pheno}^*) = -1.80$ V vs. SCE in DMA)⁹⁸. In the general reaction conditions with 15 μM **1**, 0.4 mM Pheno, 20% TEOA and 0.05 M BIH, formate was obtained with a high TON of 565 (Table 1, entry 5).

$g\text{-C}_3\text{N}_4$ is a well-known semiconductor which has visible-light absorbability and negative conduction band energy able to transfer electrons to **1** (the estimated flat band potential is ~ -1.35 V vs. SCE)⁹⁹⁻¹⁰¹. With a system containing 20 μM **1**, 2.5 mg $g\text{-C}_3\text{N}_4$ and 20% TEOA + 0.025 M BIH, CO_2 was reduced to formate with a TON of 493 (Fig. 2.2c and Table 2.1, entry 4) and a selectivity of 91% (1.7% quantum yield). H_2 was

obtained as a minor product with a TON of 48. No CO and no hydrocarbons were detected. Similarly, when replacing catalyst **1** by CoCl₂ only obtained small amounts of H₂ and CO (Table 2.2, entries 30–32). With only TEOA as sacrificial donor, a similar result reached out with slightly lower formate selectivity (74.5%, Table 2.2, entries 24–28). This observation illustrates that an earth-abundant metal complex associated with g-C₃N₄ as photoabsorbing material can selectively trigger the reduction of CO₂ to formate.

c. Switching catalytic selectivity to CO

The addition of phenol (PhOH) can improve the reactivity and switch the selectivity for CO₂ reduction to CO, with a maximum TON of 829 and catalytic selectivity ranging from 90% to 99%, depending on the catalytic conditions. In the presence of 1 M PhOH, 0.1 M BIH, Ru(phen)₃²⁺ and **1**, CO was obtained with 96% catalytic selectivity (TON of 829) upon 1 h irradiation (Fig. 2.2d and Table 2.1, entry 6). In similar conditions, with Pheno as sensitizer, a TON of 518 (89.3% selectivity) in ACN (Table 2.1, entry 7) and a TON of 380 (99% selectivity) in a DMF solution were obtained (Table 2.2, entry 20). At the same time, the faster rate for CO production than that for HCOO⁻ formation suggest different catalytic pathways with the same catalyst (see for example entries 2–3 and 6 in Table 2.1).

2.3.2 Investigation of Co₂biqpy by electrochemistry

Electrochemical experiments including cyclic voltammetry (CV), electrolysis and spectro-electrochemistry as well as density functional theory (DFT) calculations were conducted to shed light on the catalytic mechanisms.

As shown in Fig. 2.8, the first CV reversible wave of **1** is observed at ~-0.65 V vs. SCE. It is a two-electron, metal-centered wave that can be assigned to [Co^ICo^IL]²⁺ formation. The second wave at -0.81 V vs. SCE results from the reduction of each ligand moiety, leading to [Co^ICo^IL²⁻]. Then the more negative waves may correspond to ligand-centered reaction.

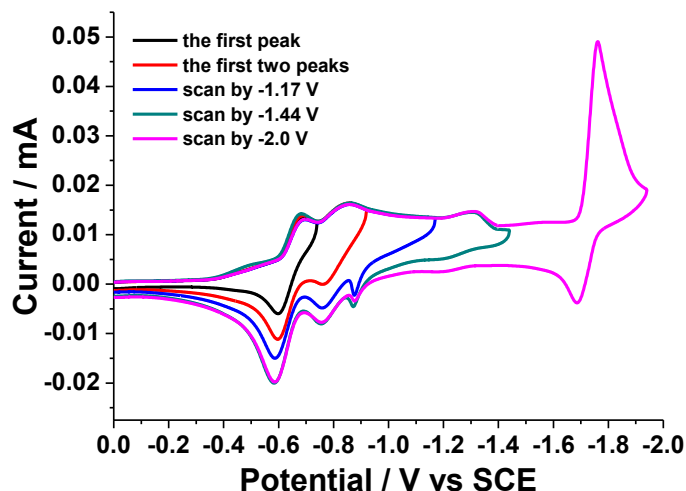


Fig. 2.8 CV of 0.5mM **1** in 0.1M $n\text{Bu}_4\text{NPF}_6$ ACN solution under Ar. $\nu = 0.1$ V/s. Adapted with permission from ref. ⁴⁹ Copyright © 2019, Springer Nature.

By comparing with the single-electron reversible wave of monomeric complex **2**, the number of electrons in each wave of **1** can be calculated (Fig. 2.9).^{81, 83, 102} In a CO_2 saturated solution, a multi-electronic catalytic wave occurred on the wave at -1.75 V vs. SCE (Fig. 2.13), while the other waves remain unchanged.

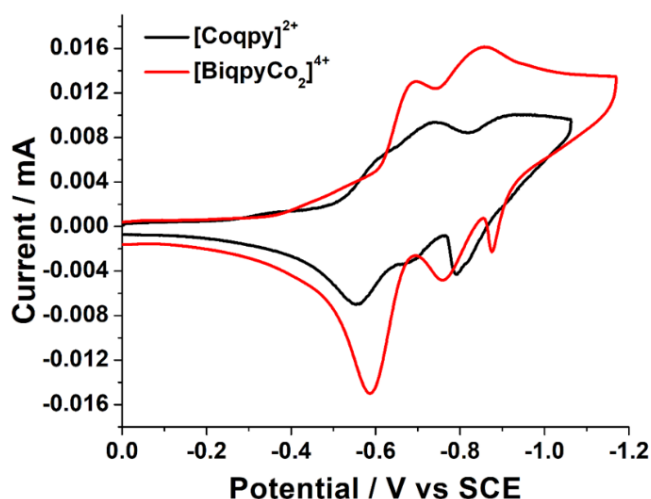


Fig. 2.9 CV of 0.5 mM $[\text{Coqpy}]^{2+}$ (black) and $[\text{BiqpyCo}_2]^{4+}$ (red) in 0.1 M $n\text{Bu}_4\text{NPF}_6$ ACN solution under Ar at scan rate of 100 mV/s. Adapted with permission from ref.⁴⁹ Copyright © 2019, Springer Nature.

When phenol is added into the solution, the catalytic wave is shifted positively showing an onset potential at ~ -1.25 V vs. SCE (Fig. 2.10); with 0.5 M PhOH, CO was obtained with a faradaic yield of 99.5% and trace H_2 during a bulk electrolysis at -1.4 V

vs. SCE for 3 hours (Fig. 2.11), in agreement with the results obtained in photochemical conditions (Table 2.1, entries 6 and 7).

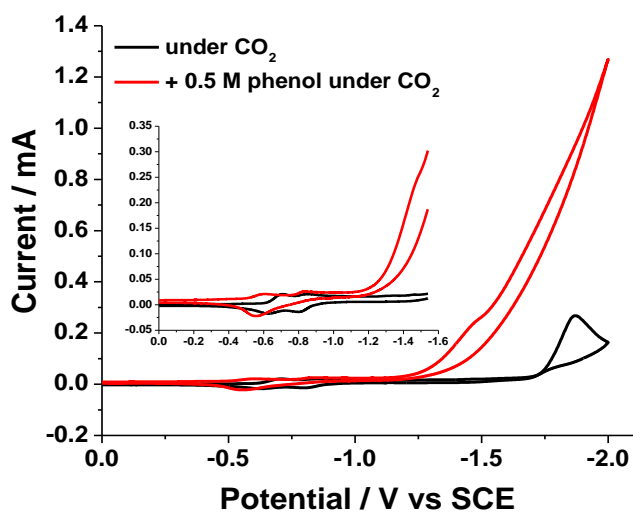


Fig. 2.10 CVs of 0.5 mM **1** in 0.1M ${}^n\text{Bu}_4\text{NPF}_6$ ACN solution in the presence (red) and absence (black) of 0.5 M PhOH under CO_2 at scan rate of 100 mV/s. Adapted with permission from ref. ⁴⁹ Copyright © 2019, Springer Nature.

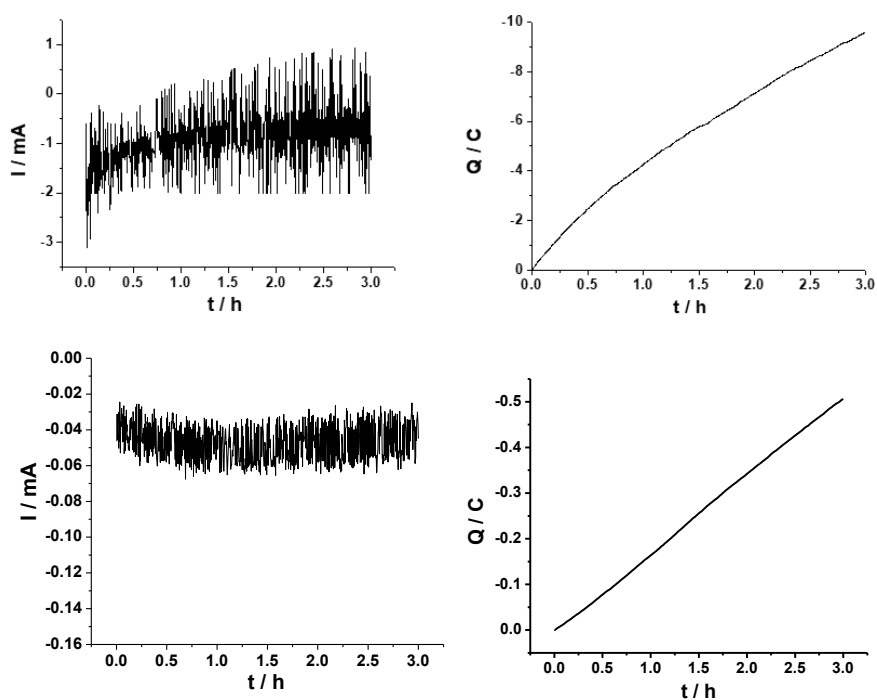


Fig. 2.11 Current (left) and charge (right) versus time curves for bulk electrolysis of CO_2 -saturated ACN solution containing: Top, 1 mM **1**, 0.5 M PhOH and 0.1 M ${}^n\text{Bu}_4\text{NPF}_6$ at -1.4 V vs. SCE; Bottom: 0.5 M phenol and 0.1 M ${}^n\text{Bu}_4\text{NPF}_6$ at -1.4 V vs. SCE (no CO or formate or H_2 was detected). Adapted with permission from ref. ⁴⁹ Copyright © 2019, Springer Nature.

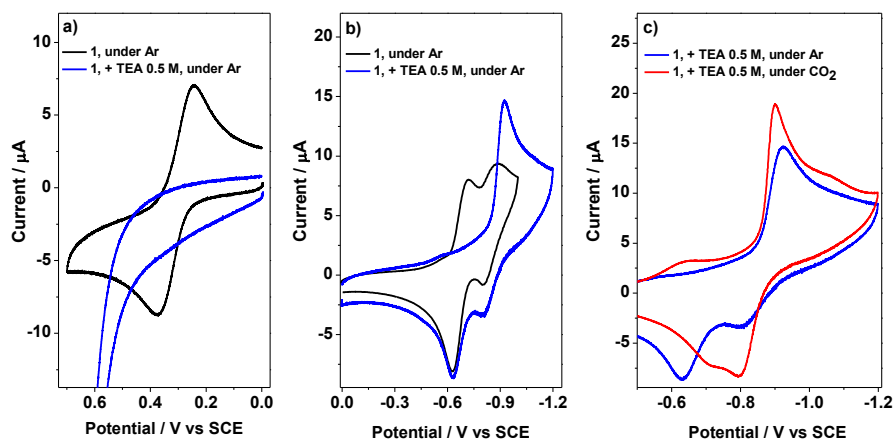


Fig. 2.12 CV of 0.3 mM **1** in 0.1M $n\text{Bu}_4\text{NPF}_6$ ACN solution in the presence (blue, red) and absence (black) of 0.5 M TEA: under Ar (a) upon oxidative scan, (b) upon reductive scan, and under CO_2 (c) (red trace). The glassy carbon diameter was 3 mm at scan rate of 100 mV/s. Adapted with permission from ref. ⁴⁹ Copyright © 2019, Springer Nature.

When performing CV under an Ar atmosphere in the presence of 0.5M TEA, the first two reduction waves merged into a single one at a more cathodic potential (-0.92 V vs. SCE, Fig. 2.12), suggesting TEA binding to the Co^{II} centres, which are then reduced with a C+E mechanism (a chemical reaction follow-up electrode electron transfer mechanism):

The binding of complex **1** to the amine may happen considering the disappearance of the $[\text{Co}^{\text{II}}\text{Co}^{\text{II}}(\text{L})]^{4+}$ oxidation wave of **1** (Fig. 2.12). Once CO_2 is introduced into the solution, a 24 mV shift towards positive potential occurs on the first reduction peak, indicative of binding to CO_2 (Fig. 2.12).



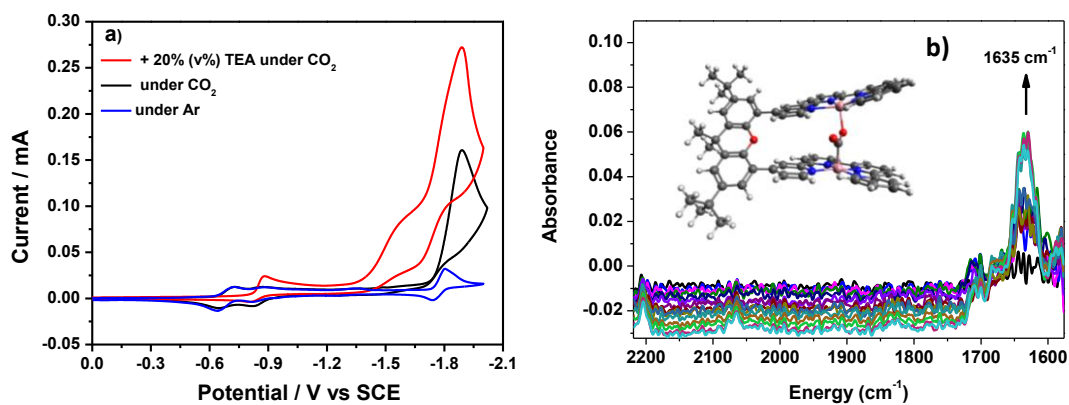
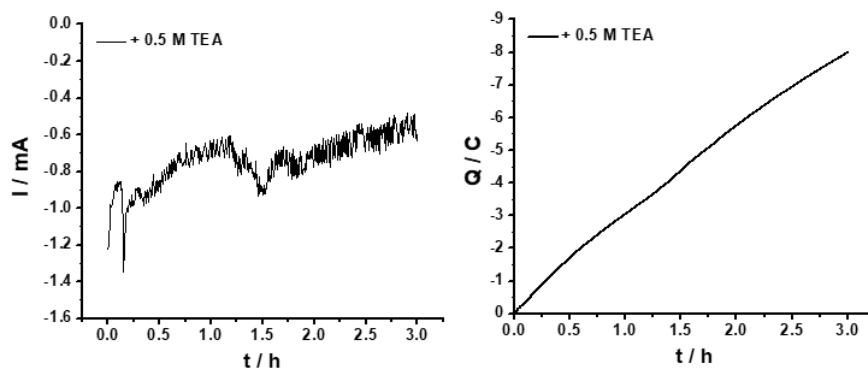


Fig. 2.13 Cyclic voltammograms and infrared spectroelectrochemistry spectra. (a). CVs in ACN solution containing 0.3 mM **1** and 0.1 M ⁿBu₄NPF₆ under Ar atmosphere (blue), in the absence (black) and presence (red) of 20% TEA under CO₂ saturation. (b). IR-SEC experiment on a 1 mM solution of **1** in ACN (0.1 M ⁿBu₄NPF₆, 0.5 M TEA) under CO₂; the potential was set at the first reduction wave (see text). Adapted with permission from ref. ⁴⁹ Copyright © 2019, Springer Nature.

The addition of TEA also encouraged a new catalytic wave at ~ -1.5 V vs. SCE (Fig. 2.13a), which corresponds to the CO₂-catalyst adduct reduction. Bulk electrolysis of the CO₂-saturated MeCN solution containing 0.5 mM **1**, 0.5 M TEA and 0.1 M ⁿBu₄NPF₆ at -1.5 V vs. SCE gave CO, formate and H₂ with faradaic yields of 90%, 7% and 0.5%, respectively (Fig. 2.14).



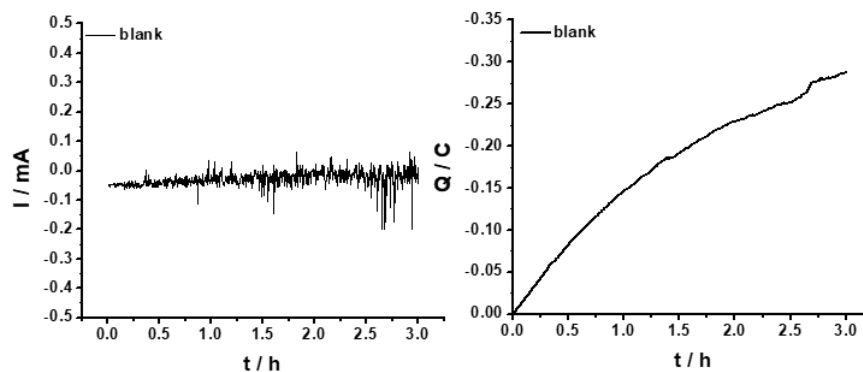


Fig. 2.14 Current (left) and charge (right) evolution with time during bulk electrolysis of CO₂- saturated ACN solution containing: Top, 0.5 mM **1**, 0.5 M TEA and 0.1 M ⁿBu₄NPF₆ at -1.5 V vs. SCE; Bottom, 0.5 M TEA and 0.1 M ⁿBu₄NPF₆ at -1.5 V vs. SCE (no CO or formate or H₂ was detected). Adapted with permission from ref. ⁴⁹ Copyright © 2019, Springer Nature.

With increasing the concentration of TEA to 1.44 M (20% in volume ratio), faradaic yield for formate and H₂ also increased to 15.8% and 3.8%, respectively, while the generation of CO was inhibited to a faradaic yield 78.3%. That means, formate production could happen in electrochemical conditions with a large concentration of amine, even if CO formation represents a competitive pathway occurring in parallel.

Spectroelectrochemistry (SEC) in the infrared region was performed at various potentials in CO₂-saturated solutions and in the presence of 0.5 M TEA (Fig. 2.13b). When the potential was scanned from -0.35 V to -0.85 V (vs. the Ag pseudo-reference), a potential window within which the catalyst is reduced, an absorption band at 1,635 cm⁻¹ built up (Fig. 2.13b), which suggest a stable [CO₂-4 electrons reduced complex] adduct.

DFT calculations were carried out at B3LYP and M06 levels on two different coordination modes of CO₂ with [Co^ICo^I(L²⁻)] (noted [CoCo(L)] in the following):. (1) CO₂ sandwiched between two Co centres and (2) CO₂ coordinated to one of the Co only. For (1), the scaled vibrational frequencies⁵⁶ of asymmetric C=O stretching are 1612 (B3LYP) and 1615 (M06) cm⁻¹. For (2), the scaled vibrational frequencies of asymmetric C=O stretching are 1,866 (B3LYP) and 1,987 (M06) cm⁻¹. These results show that it is very unlikely that CO₂ molecules bound to only one Co from the outside of the complex

cavity. While an adduct with the C atom from CO₂ binding to one Co atom, and one O atom interacting with the second Co atom (Fig. 2.13b, inset), gives a C–O stretching frequency in good agreement with the experimental value.

Natural bond orbital (NBO) analysis of the adduct between [CoCo(L)] and CO₂ (noted [CoCoCO₂(L)]) shows that the Co atom bound to the C of the CO₂ has approximately nine electrons in its valence orbitals (oxidation state 0) while the Co bound to the O atom has only eight electrons in its valence orbitals (oxidation state +1) (Tables 2.4 and 2.5). This indicates that in the four-electron-reduced compound [CoCoCO₂(L)], two electrons are located on one Co atom, which acts as a nucleophile on binding to the C of CO₂, one electron is on the second Co centre, which behaves as an electrophile to stabilize one O atom of the CO₂, and the fourth electron is delocalized over the ligand core. The two metals thus act synergistically to reductively bind and stabilize the CO₂.

Table 2.4. Natural electron configuration of [CoCoCO₂(L)].

Co1	[core]4s (0.28) 3d(7.29) 4p(0.40)
Co2	[core]4s (0.31) 3d(7.98) 4p(0.56) 5s(0.01) 4d(0.01) 5p(0.01)

Table 2.5 Calculated spin density (e⁻) of [CoCoCO₂(L)] summed for Co atoms and quaterpyridine fragments.

Co1	Qpy1	Co2	Qpy2
2.71	1.18	0.03	0.02

On setting the potential at the foot of the catalytic wave (-1.25 V vs. the Ag pseudo-reference electrode), the band at 1635 cm⁻¹ quickly disappeared and new bands at 1649 cm⁻¹ and 1680 cm⁻¹ appeared, showing the formation of bicarbonate (Fig. 2.15). A low-intensity band (shoulder) at ~1616 cm⁻¹ also appeared. Although we do not know exactly its nature so far, this may be related to a formate-complex or free formate.

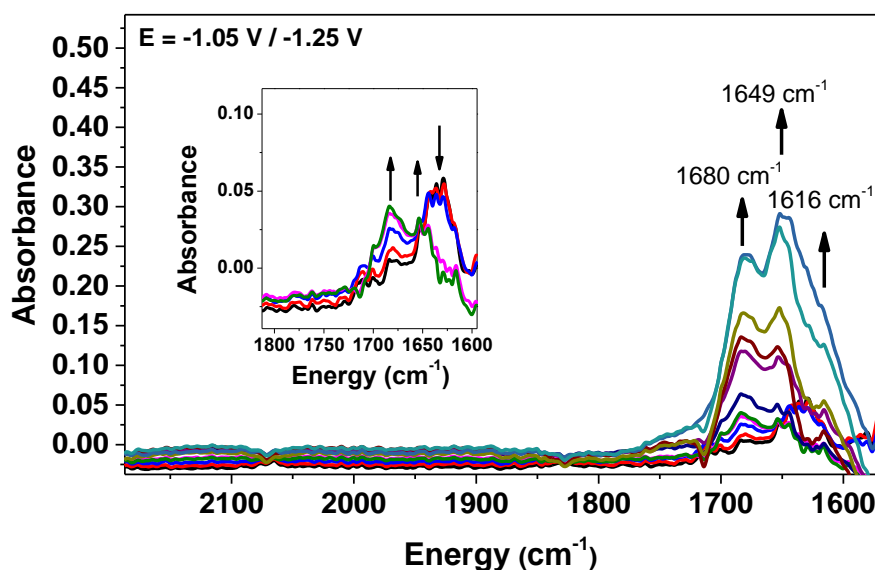


Fig. 2.15 IR-SEC experiment on a 1 mM solution of **1** in ACN (0.1 M nBu₄NPF₆, 0.5 M TEA) under CO₂ at the second reduction wave. The inset shows the disappearance of the CO₂-adduct (band at 1635 cm⁻¹) with the parallel formation of bicarbonate (bands at 1680 cm⁻¹ and 1649 cm⁻¹) occurring during the first scans. Adapted with permission from ref. ⁴⁹ Copyright © 2019, Springer Nature.

All these observations are consistent with photochemical experiments for high selective formate production (Table 2.1, entries 1–5). Comparing with photocatalytic experiments conducted with monomeric complex **2**, the reactivity is a direct consequence of metal cooperativity is further illustrated by. We found that at low catalyst concentration (5 μM) and in the presence of [Ru(phen)₃]²⁺ and TEOA, CO was produced with high selectivity (91%) and TON (1989), as we have already observed with various sensitizers, but on increasing the catalyst concentration to 150 μM, the selectivity for formate increased to 50%, with CO and H₂ being produced in 33% and 17% yield, respectively (Fig. 2.16a and Table 2.6). From 5 to 150 μM of catalyst, the CO/HCOO⁻ ratio was reduced from 18.1 to 0.65, following a mechanism for formate production involving two Co centers for binding CO₂, which is favored at a high concentration of **2**.

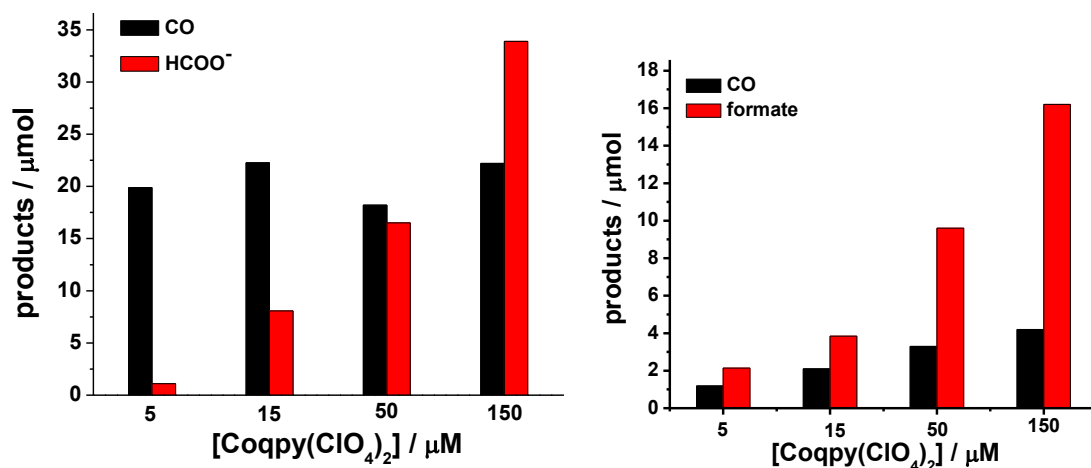


Fig. 2.16 Yields of CO and HCOO⁻ vs. [Coqpy(ClO₄)₂] for the photocatalytic CO₂ reduction of : Top, [Coqpy]²⁺ / 0.2 mM Ru(phen)₃Cl₂ / 20% TEOA / 0.1 M BIH system; Bottom, [Coqpy]²⁺ / 0.2 mM Ru(phen)₃Cl₂ / 20% TEA / 0.025 M BIH system. Adapted with permission from ref. ⁴⁹ Copyright © 2019, Springer Nature.

Table 2.6 Photoinduced CO₂ catalytic reduction with various concentrations of catalyst **2**.^a

entry	[2]/μM	Time/h	TON (selectivity, %)			Ration of n(CO)/n (HCOO ⁻)
			HCOO ⁻	CO	H ₂	
1	5	6.5	110(5)	1989(91)	83(4)	18.1
2	15	16.5	269(24)	742(67)	105(9)	2.8
3	50	24	165(38)	182(42)	85(20)	1.1
4	150	26.7	113(50)	74(33)	39(17)	0.65

^a In a typical run, 2 mL of CO₂-saturated ACN solution containing various concentrations of **2**, Ru(phen)₃Cl₂ (0.2 mM), TEOA (20%, v%) and BIH (0.1 M) was irradiated using blue LED (460 nm) at 24 °C. The TONs of products leveled off after 6.5 h, 16.5 h, 24 h and 26.7 h for entry 1, 2, 3 and 4 respectively. TON values are ±5%.

2.3.3 Proposed pathway for CO and formate production

All these observations, together with preliminary theoretical calculations (Fig. 2.17), converge to a possible mechanism for the visible-light-driven reduction of CO₂ with catalyst **1** that is shown in Fig. 2.18. Initially, catalyst **1** undergoes 4e⁻ reduction assisted by the photosensitizer to afford the neutral [CoCo(L)] species, which reductively binds to CO₂ with one Co centre linked to the C atom of CO₂ and the other to an O atom, forming a sandwich type CO₂ adduct [CoCoCO₂(L)] (Figs. 2.18 and 2.13 b, inset). Remarkably,

the OCO angles decrease from 180° to 126° and the C–O bond lengths increase from 1.116 Å to 1.243 and 1.286 Å, in line with CO₂ structure modification during reduction. After a one-electron reduction of this adduct, the catalytically active species [CoCoCO₂(L)]⁻ leads to product formation. In acidic conditions, protonation of the CO₂ adduct takes place efficiently at the O atom stabilized by one of the two Co atoms, and C–O bond cleavage results in the subsequent release of CO as product. A second reaction pathway was identified, involving C to O linkage isomerization of the reduced CO₂ adduct to [CoCoO₂C(L)]⁻ (Fig. 2.18).

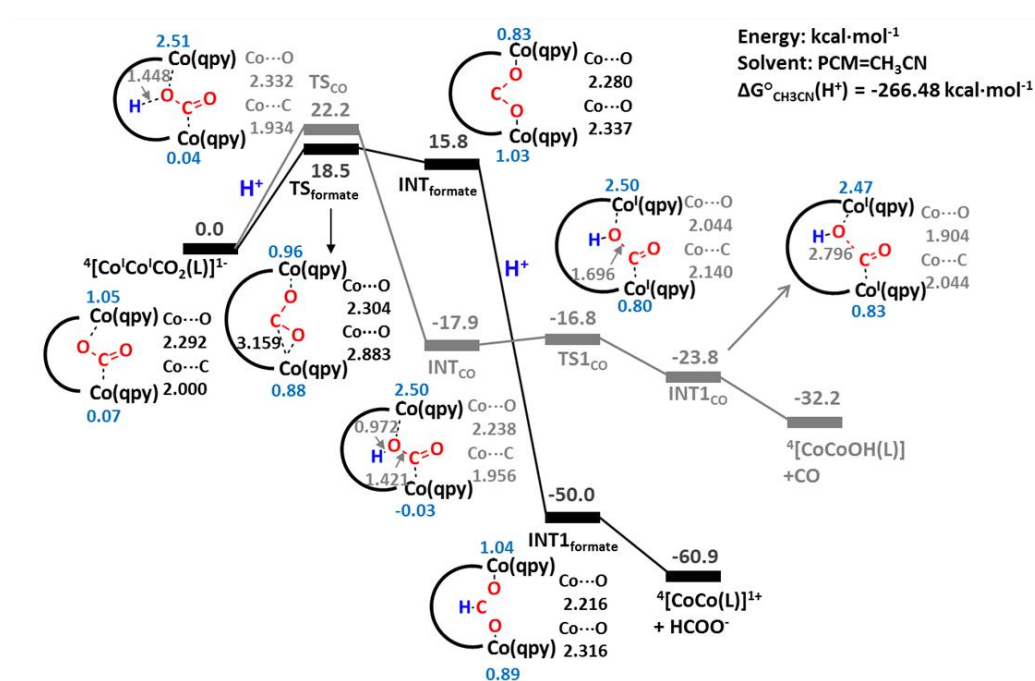


Fig. 2.17 Potential energy surface of CO₂ reduction by [CoCo(L)]⁻ at B3LYP/LanL2DZ(Co)/6-31+G(d)(nonmetals)//B3LYP/LanL2DZ(Co)/6-31G(d)(nonmetals) level. Relative Gibbs free energies at 298 K in ACN are given in kcal mol⁻¹. The spin density on Co is also given. Relative Gibbs free energies at 298 K in ACN are given in kcal·mol⁻¹. The spin density (numbers in blue color) on Co is also given. Adapted with permission from ref. ⁴⁹ Copyright © 2019, Springer Nature.

This isomerization step is endowed with a barrier of 18.5 kcal mol⁻¹ and may become competitive in media with low proton availability. [CoCoO₂C(L)]⁻ is then quickly protonated at the basic C atom with release of formate, in accordance with experimental results observed under basic conditions. Cooperativity between the two Co centres of

reduced catalyst **1** is thus the key for not only CO₂ binding but also for driving the reaction towards HCOO⁻ evolution. The alternative formation of a hydride species bridging between the two Co atoms that would further insert CO₂ to give HCOO⁻ could not be ruled out, although the absence of formate evolution in acidic conditions and the low amount of H₂ produced in all experiments makes this mechanism unlikely. However, a further mechanistic investigation will shed more light on the process, starting from Fig. 2.18, which stands as a working model.

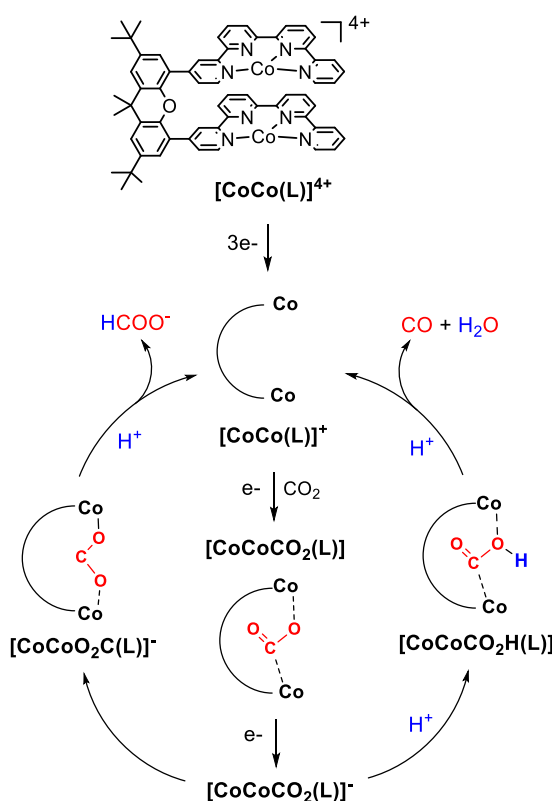


Figure 2.18 Proposed mechanism for visible-light-driven catalytic reduction of CO₂ into CO and HCOO⁻ with catalyst **1**. Complex **1** undergoes 4e⁻ reduction by the photosensitizer to afford the neutral [CoCo(L)] species which reductively binds to CO₂ with one Co center linked to C atom of CO₂ and the other to O atom, forming a sandwich type CO₂ adduct [CoCoCO₂(L)]. After a one electron reduction of this adduct, the catalytically active species [CoCoCO₂(L)]⁻ leads to product formation, either CO or formate. Adapted with permission from ref. ⁴⁹ Copyright © 2019, Springer Nature.

2.4 Sub-conclusion and sub-perspectives for bimetallic catalytic system

Various sensitizers have been employed for the photochemical reduction of CO₂, including a Ru complex, an organic phenoxazine compound as well as semiconducting g-C₃N₄ in combination with a binuclear cobalt complex as catalyst. These systems can selectively catalyze visible-light-driven CO₂ reduction to CO with high TON in the presence of weak acid phenol. By simply replacing phenol by TEOA in the solution, the catalytic process could be switched to selective formate formation with a maximum quantum efficiency of 2.6%. The synergy between the two cobalt metals guarantees the dual reactivity, which illustrates the fantastic potential of multimetallic molecular catalysts. Observation in cyclic voltammetry, spectro-electrochemistry, and DFT calculations reveal different intermediates that might correspond to new pathways of highly reduced products beyond 2 electrons/ 2 protons. We have used a ligand that consists of two quaterpyridine linked by xanthene moiety to coordinate with two cobalt, obtaining a complex with substrate-dependent selectivity towards formic acid or carbon monoxide. Other metal-based complexes have also been reported, including zinc, iron, copper, nickel.^{47, 48, 92} Heterobimetallic catalysts containing two of them can be considered for constructing a catalytic assembly with nucleophilic center and electrophilic center, respectively. It is possible to select other metals to complete the conversion of carbon dioxide to highly reduced products.

On the other hand, the link units in bimetallic complexes also have effects on the whole catalytic performance. Stable and efficient electron transfer along the linkage may boost product formation. Also, the structure of the linkage can be adjusted to tune the distance between metal centers. It is interesting to imagine the possibility of containing two or more CO₂ molecules to form C-C bond for complex reduced products. In that case, cobalt may not be the best choice of metal center: Coqpy is indeed an efficient catalyst for CO production and but is not known to be able to fix CO for further. So metals such as Fe and Cu that can keep and utilize CO in other catalytic processes may provide much more suitable active catalytic centers.

Chapter 3 - Heterogeneous photochemical reduction of CO₂ with covalently bonded molecular catalysts

Surface modification of carbon materials such as carbon nanotubes, carbon nitride and graphene derivatives has received particular attention,^{103, 104} and these materials are now widely used as electrode materials with high effective surface area combined with excellent conductivity (especially multiwalled CNTs - MWCNTs) and mechanical stability.¹⁰⁵ Recently, different techniques have been developed for the chemical functionalization of carbon materials such as graphene.¹⁰⁶ Generally, most reactions reported for the modification of sp² carbon in CNTs and graphene can potentially be adapted to other types of π -conjugated carbon surfaces. We chose the widely studied semiconductor materials carbon nitride (C₃N₄) and graphene as substrate. After morphology improvement and surface functionalization, they were covalently combined with molecular catalysts to study their catalytic performance towards CO₂ reduction.¹⁰⁷

3.1 Photochemical reduction of CO₂-to-CO with Coqpy covalently grafted on mesoporous graphitic carbon nitride (“Coqpy@mpg-C₃N₄”)

3.1.1 Synthesis and characterization of Coqpy@mpg-C₃N₄

a. Molecular-materials hybrid assemblies preparation

Mesoporous graphitic carbon nitride (mpg-C₃N₄)¹⁰⁸ and nanosheets of graphitic carbon nitride (nsg-C₃N₄)¹⁰⁹ were prepared according to previously reported methods. Coqpy@mpg-C₃N₄ was prepared by the addition of 1-ethyl-3-(3-dimethylaminopropyl)carbodiimide (EDC, 3.05 mg, 16 μ mol) and triethylamine (TEA, 2.2 μ L, 16 μ mol) to a stirring suspension of Coqpy-Ph-COOH (4.48 mg, 8 μ mol, see Fig. 3.1) in DMF (5 mL), a modified quaterpyridine with a benzoic acid group.

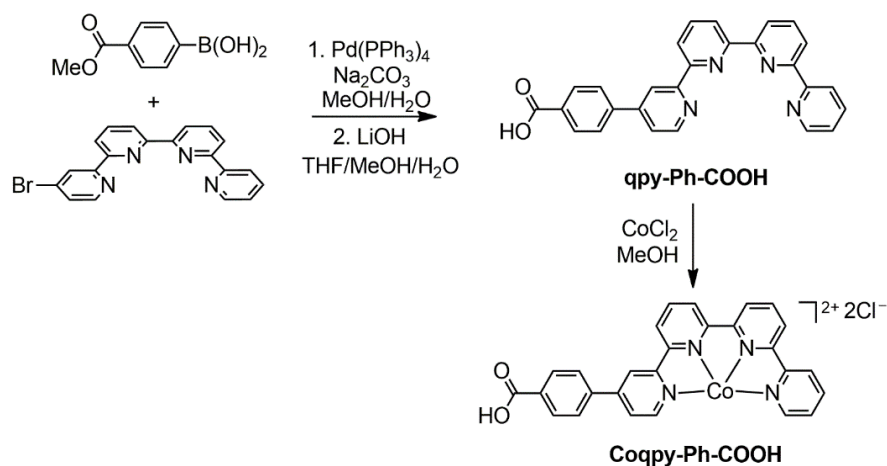


Fig. 3.1 Synthesis scheme of Coqpy-Ph-COOH catalyst. Adapted with permission from ref. 107,¹⁰⁷

Copyright 2020 American Chemical Society.

The mixture was stirred for 20 min at room temperature, then a 1-hydroxybenzotriazole (HOBt, 2.14 mg, 16 μ mol) solution in 0.5 mL DMF was added and kept stirring for 1 h. Next, mpg-C₃N₄ (80 mg) suspension in 2 mL DMF was introduced into the mixture. After stirring for 7 days, the product was isolated by filtration on a Nylon membrane (0.1 μ m). Excess Coqpy-Ph-COOH and other impurities were removed through washing cycles, including sonication, filtration and re-suspension of the solid in DMF (200 mL). UV-Vis spectroscopy was used to check the filtrate to ensure no Coqpy-Ph-COOH remained in the final washing. After filtration, the obtained Coqpy@mpg-C₃N₄ was washed with ultrapure water several times, following the above procedure. Finally, the precipitate was dried under vacuum to yield the Coqpy@mpg-C₃N₄ hybrid. Coqpy@nsg-C₃N₄ was similarly synthesized by using nsg-C₃N₄ instead of mpg-C₃N₄. Two other types of materials have prepared. First adsorbed sample Coqpy-mpg-C₃N₄ was prepared by dissolving Coqpy-Ph-COOH (1 mg) into a mpg-C₃N₄ (25 mg) suspension in 25 mL DMF. After stirring overnight, the final solid was obtained by a similar post-treatment including filtration and washing cycles, but no sonication. In a final step, the precipitate was dried under vacuum to yield the Coqpy-mpg-C₃N₄, for which the Co complex is physically adsorbed onto the carbon nitride material. Mixed sample Coqpy-Ph-COOH/mpg-C₃N₄ was prepared as follows: the mpg-C₃N₄ was dispersed into ACN and sonicated to achieve a uniform suspension. After that, a defined amount of Coqpy-Ph-

COOH solution was added into the suspension and the photocatalysis was started immediately.

b. Nitrogen adsorption/desorption experiment

From nitrogen adsorption/desorption isothermal test at 77 K, the pore volume and specific surface area of the substrate mp-g-C₃N₄ were calculated to be 0.4993 cm³ g⁻¹ and 110.7 m² g⁻¹, respectively. After grafting with Coqpy and photoreaction, the pore volume of 0.5219 cm³ g⁻¹ and specific surface area of 118.8 m² g⁻¹ was obtained (see Fig. 3.2), meaning that the morphology was maintained.

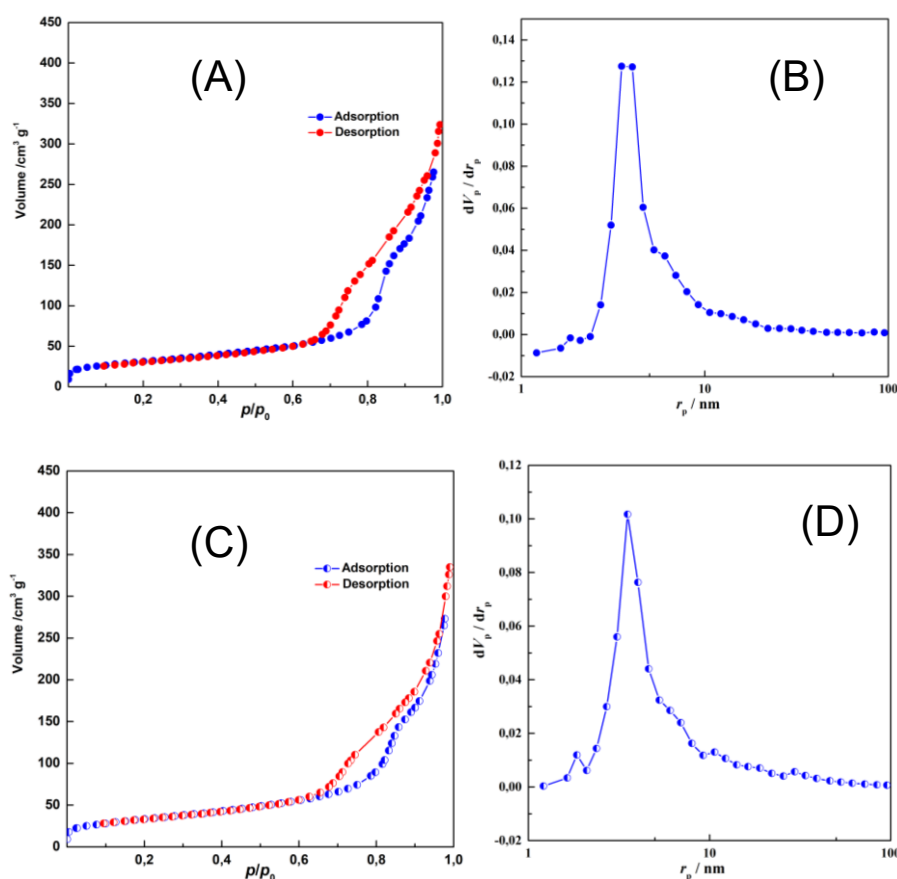


Fig. 3.2 (A) Nitrogen adsorption-desorption isotherms and (B) the corresponding Barrett-Joyner-Halenda (BJH) pore-size distribution curve of mp-g-C₃N₄; (C) Nitrogen adsorption-desorption isotherms and (D) the corresponding Barrett-Joyner-Halenda (BJH) pore-size distribution curve of mp-g-C₃N₄@Coqpy after photocatalysis in ACN solution with BIH for 24 h. Adapted with permission from ref. 107, Copyright 2020 American Chemical Society.

c. Infrared spectra

IR spectra of mpg-C₃N₄, Coqpy-Ph-COOH and of the hybrid assembly are presented in Fig. 3.3. Both bare material and hybrid assembly show typical features of mpg-C₃N₄, including N-H stretching in the 3200 cm⁻¹ region with -NH₂ specific stretching around 3280 cm⁻¹, interchain NH···O-C bonding around 3170 cm⁻¹, triazine features around 810 cm⁻¹ as well as a broad band extending in the 1100–1600 cm⁻¹ region that can be assigned to in-plane C–N stretching and bending vibrations of the graphitic layers.¹¹⁰ In the hybrid spectrum, despite weak signals due to low catalyst loading, characteristic peaks at 1682 and 1558 cm⁻¹ attributed to C=O stretching of the amide link and to in plane N-H deformation coupled with C-N stretching were observed.

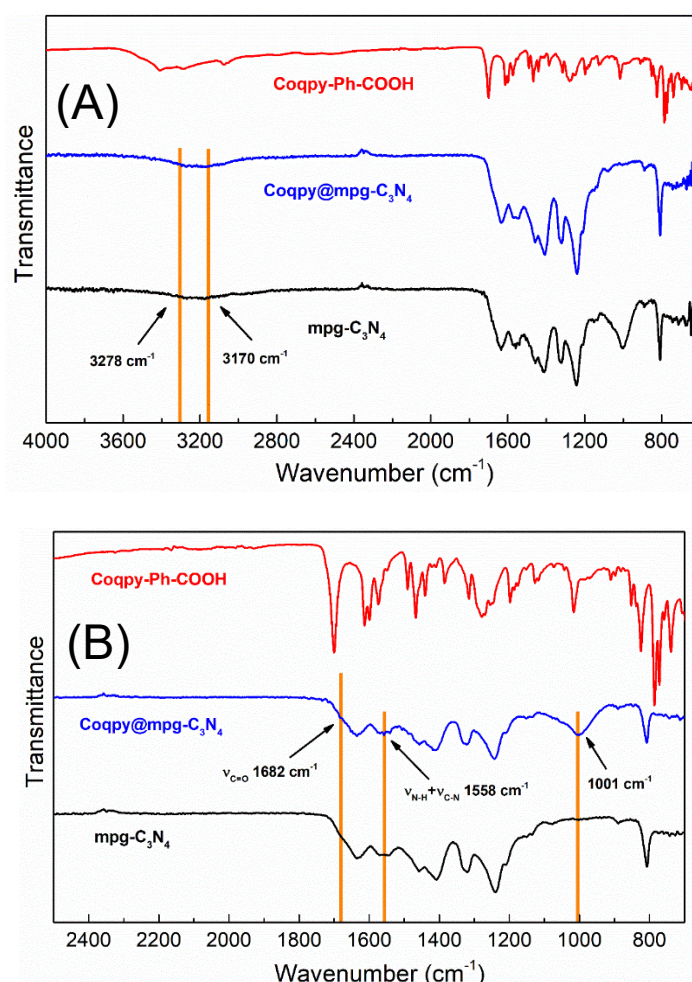
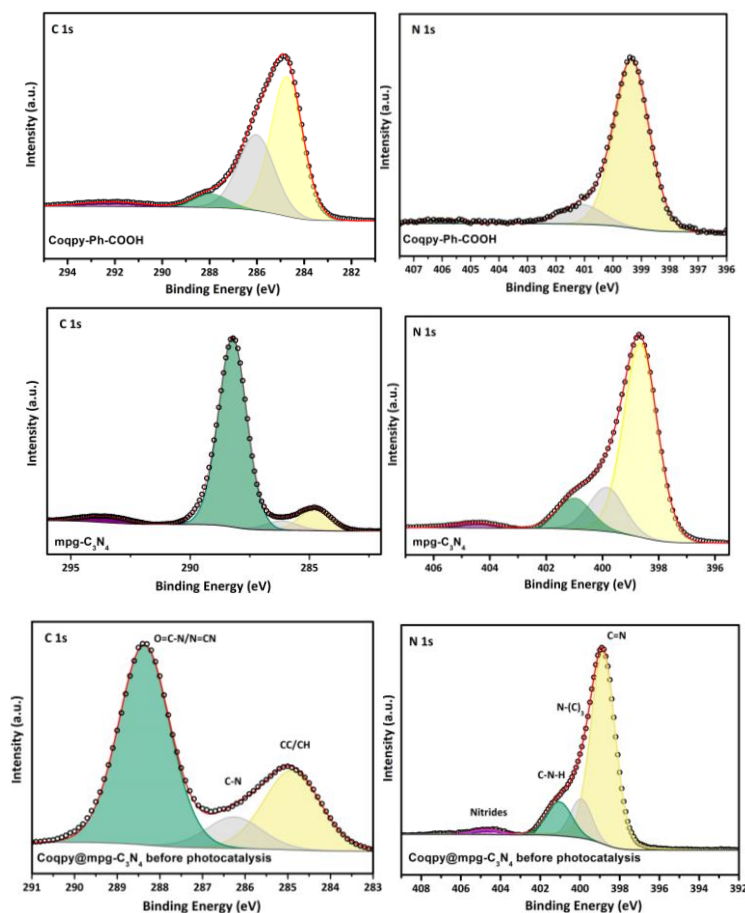


Fig. 3.3 (A) FTIR spectra of mpg-C₃N₄ (black), Coqpy-Ph-COOH (red) and of the hybrid Coqpy@mpg-C₃N₄ (blue), (A) wide scan and (B) focus on the 800–2400 cm⁻¹ region. Adapted with permission from ref. 107, Copyright 2020 American Chemical Society.

d. X-Ray Photoelectron Spectroscopy (XPS) analysis

As shown in Fig. 3.4, typical XPS signatures originating from C1s, N1s and O1s atoms within the hybrid are observed at binding energies of about 287, 400 and 532 eV.¹¹⁰ The C1s spectrum consists in three components, a first one from NC=N (carbon nitride) at 288.9 eV, a second one at 284.9 eV corresponding to C-C/C-H; a third one at 286.3 eV from C-N attributed to the coupling of C₃N₄ and Coqpy-Ph-COOH units.

The amide C=O can be observed at 532.4 eV in O1s peak. C=N and N(C)₃ peaks of the triazine motif were identified in the N1s spectrum and centered at 398.8 eV and 399.9 eV respectively. A weak N1s peak centered at 404.8 eV is attributed to the nitride substrate. The peak centered at 401.1 eV is consistent with C-N-H from covalent amide linkage. On the other hand, weak Co2p signature at *ca.* 782 eV can be observed, showing the presence of cobalt inside the hybrid material.



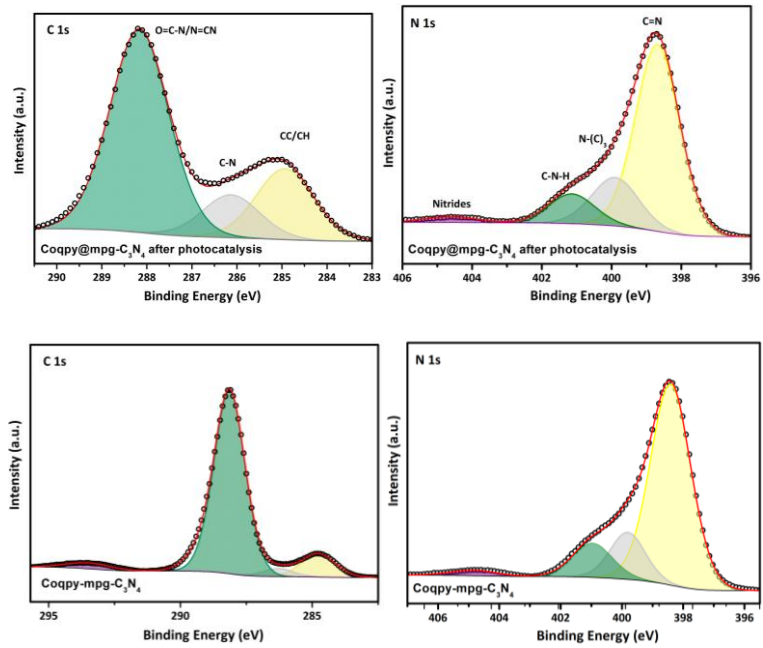
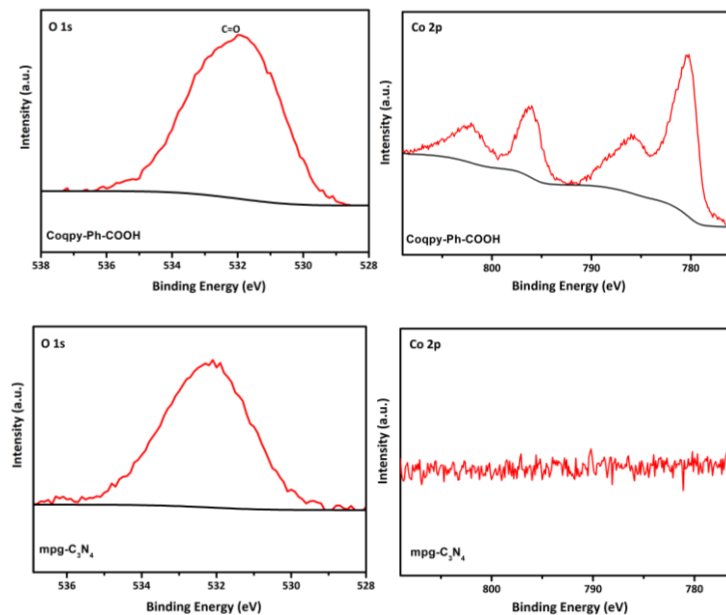


Fig. 3.4 (a) High-resolution XPS spectra of the carbon C 1s (left column) and the nitrogen N 1s (right column) of Coqpy-Ph-COOH, mpg-C₃N₄, Coqpy@mpg-C₃N₄ before photocatalysis, Coqpy@mpg-C₃N₄ after photocatalysis, Coqpy-mpg-C₃N₄ (from top to bottom). Adapted with permission from ref. 107, Copyright 2020 American Chemical Society.



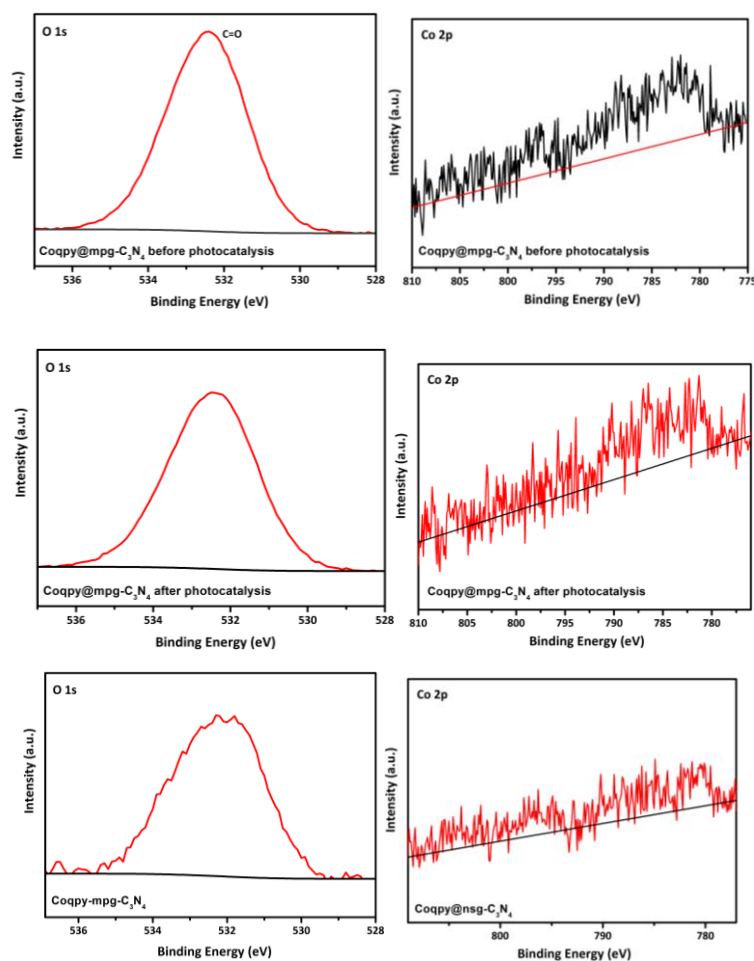


Fig. 3.4 (b). High-resolution XPS spectra of the oxygen O 1s (left column) and the cobalt Co 2p (right column) of Coqpy-Ph-COOH, mpg-C₃N₄, Coqpy@mpg-C₃N₄ before photocatalysis, Coqpy@mpg-C₃N₄ after photocatalysis, Coqpy-mpg-C₃N₄ (from top to bottom). Adapted with permission from ref. 107, Copyright 2020 American Chemical Society.*

e. Inductively Coupled Plasma - Optical Emission Spectroscopy (ICP-OES) analysis

Loading amounts of Coqpy-Ph-COOH were calculated from cobalt contents through ICP-OES. The results for different hybrid materials (covalently linked or adsorbed) are summarized in Table 3.1. The concentration of Coqpy-Ph-COOH suspended in the reaction solution is very similar to typical conditions used in a homogeneous catalyst system.^{27, 29}

Table 3.1 Amount of cobalt in hybrid materials determined by ICP, and equivalent Coqpy concentration in solution.

hybrid	Co (wt %)	Coqpy ($\mu\text{mol g}^{-1}$)	[Coqpy] ^a (μM)
Coqpy@mpg-C ₃ N ₄	0.00876	1.48	3.0
Coqpy-mpg-C ₃ N ₄	0.00744	1.26	2.5
Coqpy@nsg-C ₃ N ₄	0.02670	4.53	9.0

^a Calculated for 6 mg of hybrid material suspended in a 3 mL solution.

f. Cyclic Voltammetry analysis

The CV of Coqpy-Ph-COOH was performed in DMF containing 0.1M Bu₄NPF₆ as supporting electrolyte and is shown in Fig. 3.5.

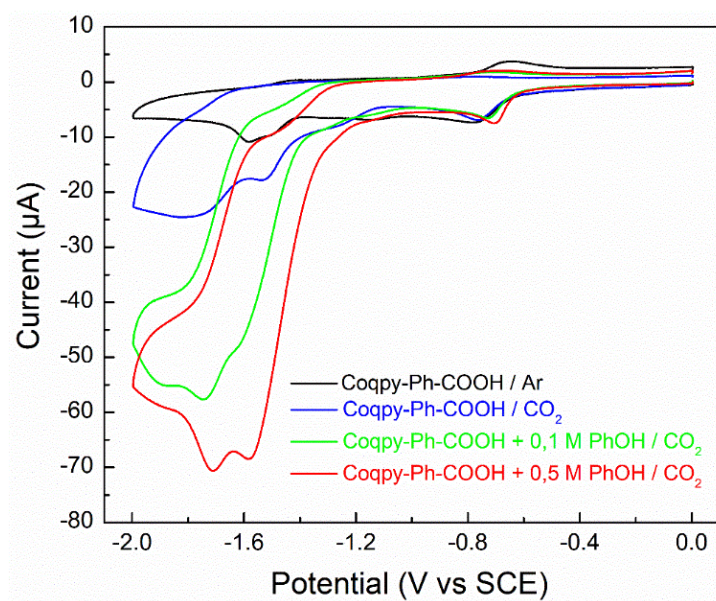


Fig. 3.5. Cyclic voltammetry of Coqpy-Ph-COOH (0.2 mM) in DMF solution (0.1 M NBu₄PF₆) at $v = 0.1$ V/s and $T = 298$ K under argon (black) and CO₂ (blue) atmosphere as well as in the presence of 0.1 M phenol (green), 0.5 M phenol (red) under CO₂. Adapted with permission from ref. 107, Copyright 2020 American Chemical Society.

Under argon and upon reductive scan, a reversible wave at -0.7 V vs. SCE is observed and is attributed to the Co^{II}/Co^I. Further reduction first leads to quasi-reversible waves at

- 1.1 V vs. SCE and -1.4 V vs. SCE due to combined metal and ligand-based reduction, in line with previous reports.^{82, 111} Under CO₂ atmosphere, an increase is observed on the latter wave, showing that Coqpy-Ph-COOH possesses the ability to catalytically reduce CO₂. In the presence of a weak Brønsted acid (phenol), the catalytic current drastically further increases. The onset potential of the catalytic wave is positive to the position of the conduction band (CB) of mpg-C₃N₄, located at *ca.* -1.35 V vs. SCE, as reported elsewhere,¹¹² indicating that the illuminated semi-conductive material may be able to reduce the cobalt molecular catalyst.

3.1.2 Catalytic performance for CO₂ reduction under visible-light

Under visible-light irradiation, the catalyst suspension can convert CO₂ to CO with a selectivity of 97% (Fig. 3.6). Long-term recycling experiment shows that the catalyst is still active for at least 4 days, reaching a TON for CO of 254 (Fig. 3.12).

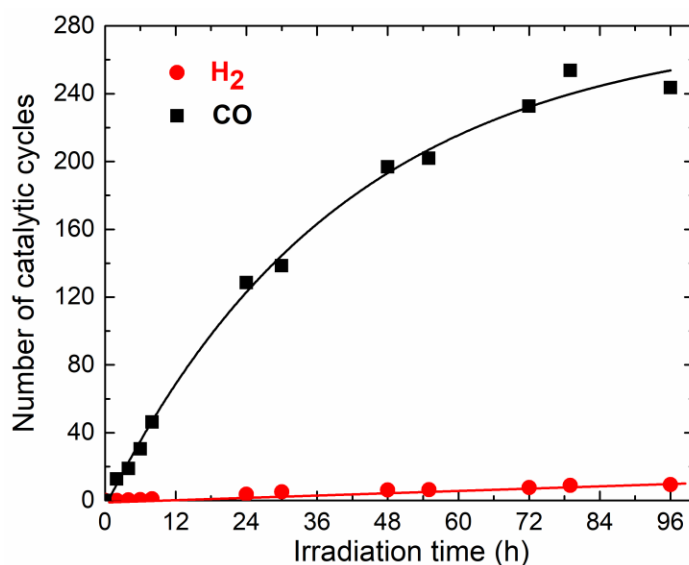


Fig. 3.6 Generation of CO (black squares) and H₂ (red circles) over 4 days upon visible-light irradiation ($\lambda > 400$ nm) of a CO₂-saturated ACN solution containing 6 mg Coqpy@mpg-C₃N₄, 0.05 M BIH, and 0.03 M PhOH. Adapted with permission from ref. 107, Copyright 2020 American Chemical Society.

The origin of carbon was asserted by running isotope-labeled experiments with ¹³CO₂ giving ¹³CO as the product (see Fig. 3.7) as shown by GC-MS measurements (Fig. 3.7(B)).

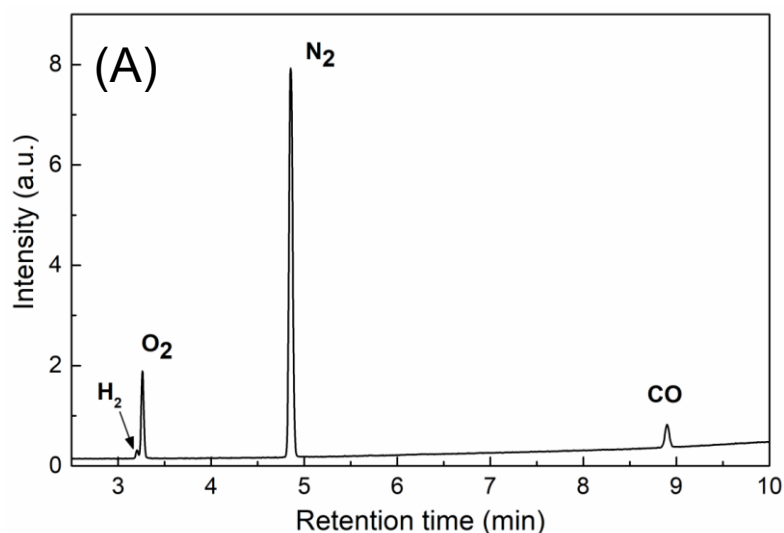


Fig. 3.7 (A) Typical gas chromatogram obtained after long-term irradiation of a suspension containing 6 mg of hybrid Coqpy@mpg-C₃N₄, 0.05 M BIH and 0.03 M phenol, under ¹³CO₂ atmosphere.

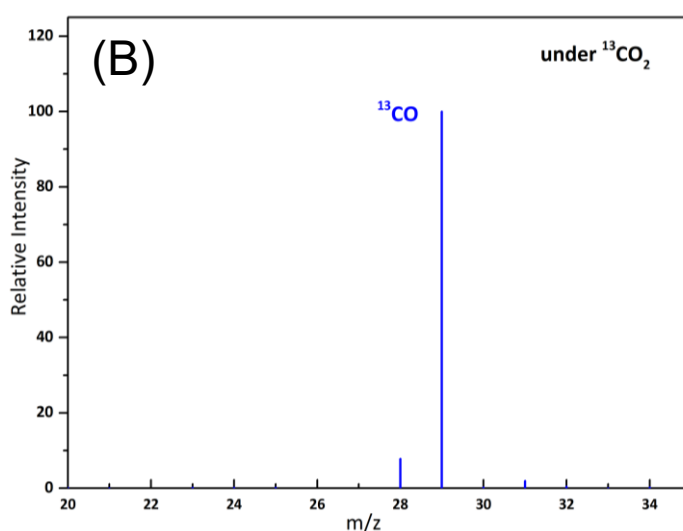


Fig. 3.7 (B) Corresponding mass spectra of the CO GC peak. Adapted with permission from ref. 107, Copyright 2020 American Chemical Society.

In order to further illustrate the advantages of this covalent bond combination, we performed a series of comparative and control experiments. Table 3.2 reports data obtained after typical 24h irradiation. No formate was identified from the liquid phase during the photocatalysis. Complete blank experiments results are also given in Table 3.2, showing that all components of the catalytic system, including CO₂ and light irradiation, are needed.

Molecular catalysts associated with the semiconductor particles may become active once photons lead to the formation of an electronically excited state. Electron transfer occurs either between molecules on the surface or between a surface site and an adsorbed/attached molecule. Similar to the classification of photocatalysis, the electron transfer process can be broadly divided into two categories, “type I” for the adsorbate molecules directly excited by photons and “type II” for the solid excited by photons. Materials that don’t participate in the photo-excited electron transfer process are called “insulator”, such as SiO₂ and Al₂O₃. They only provide a two-dimensional environment for the reactive molecules. In the case of insulator Al₂O₃ for example, electrons transfer occur directly from donor molecules to acceptor molecules.

In our experiments, we employed Al₂O₃ to further verify the role of carbon nitride (Table 3.2, entry 7). The electrons in the valence bond of C₃N₄ are first excited into the semiconductor's conduction band (CB) and then transferred into the vacant orbitals of the acceptor. The positively charged holes are left on the band edge of the valence band (VB). At the same time, another electron recombined with the holes on the valence band edge, and will be provided from the filled orbital of the donor, an easily oxidisable amine in our case.

In order to further prove the catalytic ability of the carbon nitride supported Coqpy, we use some comparative experiments to probe for catalytic role of various components. Metal cations, individual carbon nitrides, individual molecular catalysts, and insulator alumina were all tested in a series experiments. Specifically, experiments performed with a mixture of a cobalt chloride salt and carbon nitride or Coqpy-Ph-COOH and Al₂O₃ suspension only furnishes a very low amount of reduction products (entries 7 and 8 respectively, Table 3.2). Moreover, a simple mixture of the cobalt molecular complex with mpg-C₃N₄ considerably decreases the amount of CO produced (entries 2 and 3, Table 3.2) and concomitantly the selectivity for CO₂ reduction significantly diminishes. These observations indicate that covalent grafting of the molecular catalyst greatly enhances catalysis.

Table 3.2 Visible light-driven CO₂ reduction with Coqpy catalyst covalently attached to mpg-C₃N₄.

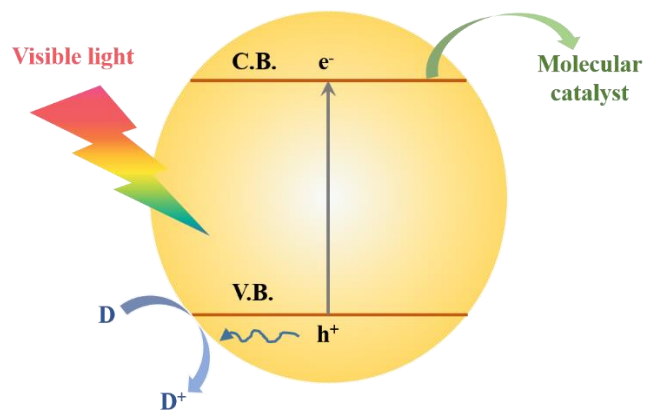
entry	catalyst ^a	product (μmol)/TON _{co} ^b /Selectivity _{co} (%)	
		H ₂	CO
1	Coqpy@mpg-C ₃ N ₄	0.06	1.15/128/98
2	Coqpy-Ph-COOH/mpg-C ₃ N ₄	0.04	0.31/37/88
3	Coqpy-mpg-C ₃ N ₄	0.03	0.15/21/83
4	Coqpy@mpg-C ₃ N ₄ ^c	0.013	0
5	Coqpy@mpg-C ₃ N ₄ ^d	0.001	0
6	mpg-C ₃ N ₄	0.012	0.017/-/59
7	Coqpy/Al ₂ O ₃	0.004	0.062/8/94
8	CoCl ₂ /mpg-C ₃ N ₄	0.013	0.018/1.7/58
9	Coqpy@nsg-C ₃ N ₄	0.018	0.81/27/98
10	Coqpy/mpg-C ₃ N ₄	0.035	0.22/26/86
11	Coqpy-mpg-C ₃ N ₄ ^e	0.09	0.52/58/85

^a reaction conditions: 6 mg catalyst (3 μM Coqpy) in a CO₂-saturated MeCN solution containing 0.05 M BIH and 0.03 M PhOH. A 6 mL quartz cell with a septum was used as the reaction vessel; and a solar simulator equipped with a 100 W Xenon lamp and a 400 nm optical filter was used as irradiation source. Reaction time: 24 h. Amount of Coqpy in catalyst: covalently linked at mpg-C₃N₄ (Coqpy@mpg-C₃N₄), 3 μM; mixed with carbon nitride (Coqpy/mpg-C₃N₄), 3 μM; adsorbed at the carbon nitride surface (Coqpy-mpg-C₃N₄), 2.5 μM; mixed with Al₂O₃ (Coqpy/Al₂O₃), 3 μM; covalently linked at nsg-C₃N₄ (Coqpy@nsg-C₃N₄), 9 μM. ^b relative to the amount of Coqpy or CoCl₂. ^c under an argon atmosphere. ^d in the dark. ^e covalent linkage with different loading amount.

Recently, a mixed catalyst of polymerized cobalt phthalocyanine and mesoporous carbon nitride has been reported to generate CO from CO₂ with *ca.* 90 TON and a selectivity of 80%.⁶⁵ In this case, light adsorption of C₃N₄ substrate may be shielded after loading with the polymers. In another study, Co²⁺ has been introduced into C₃N₄ substrate as single sites and resulted in CO₂-to-CO conversion with a TON of 200 and a selectivity of 80%.¹¹³ However, the formation of CoO oxide was observed, causing decrease photocatalytic activity.

3.1.3 Investigation of the photoinduced electron transfer mechanism

Irradiation of mpg-C₃N₄ with visible light (> 400 nm) allows electron-hole separation with the promotion of an electron in the CB of the semiconductor.



Scheme 3.1 schematic illustration of electron/hole separation under visible light illumination of a semi-conductive particle/materials.

One of the key parameters for the catalytic process is the efficiency of the electron transfer (ET) to Coqpy-Ph-COOH. We thus performed experiments to investigate the emission quenching of mpg-C₃N₄ with BIH or Coqpy-Ph-COOH (Fig. 3.8 and Fig. 3.9).

Under light excitation, electrons can be transferred from mpg-C₃N₄ to the complex Coqpy-Ph-COOH due to electronic interaction between the conduction band and the complex orbital. The complex thus play the role of an oxidative quencher. BIH is a reduction quencher which can supplement electrons in the valence band of the carbon nitride at the same time.

In our measurements, steady-state emission spectrum of suspended mpg-C₃N₄ shows two peaks of similar intensity at *ca.* 490 and 540 nm, in accordance with previous studies.¹¹⁴ We observed that the two emission peaks were quenched linearly at different rates, both with BIH and Coqpy-Ph-COOH which could be explained taking into account these peaks correspond to slightly different excited states.

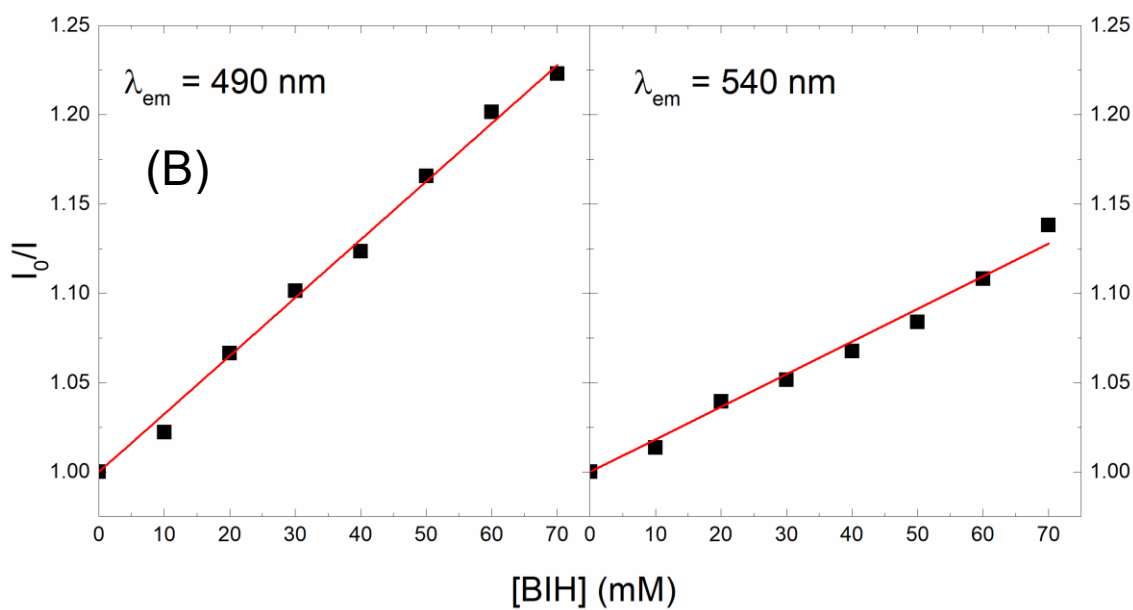
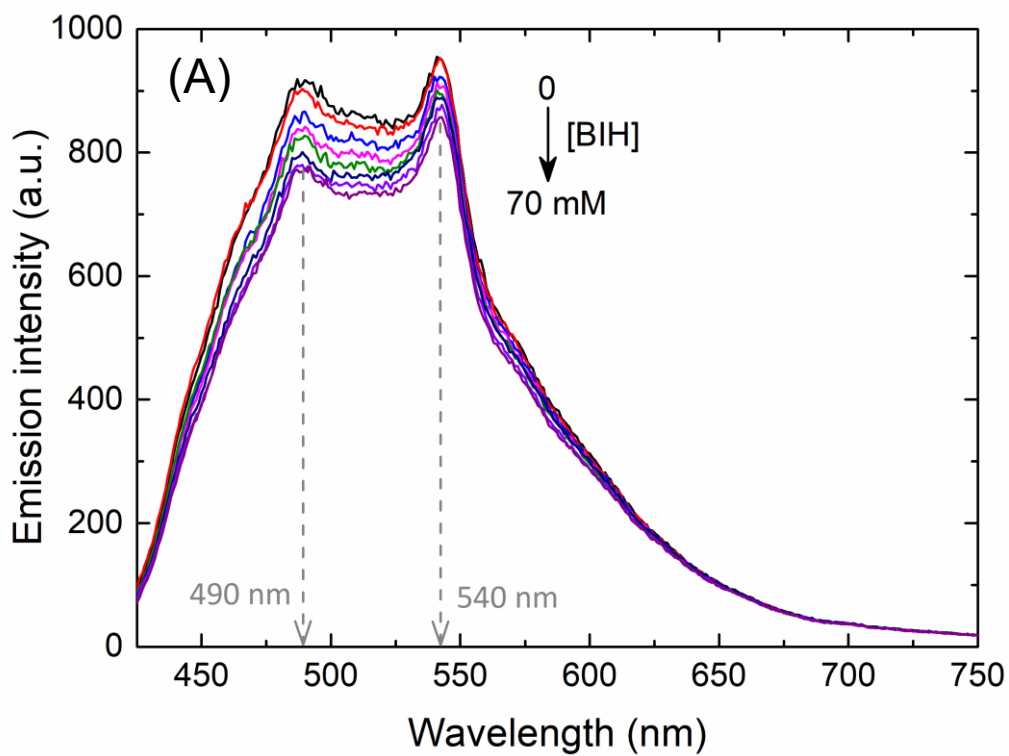


Fig. 3.8. (A) Emission spectra of a 6 mg mpg-C₃N₄ suspension in ACN containing 0 (black), 10 (red), 20 (blue), 30 (pink), 40 (green), 50 (yellow), and 60 mM (magenta) BIH; (B) linear plot of the emission ratio at 490 (left) and 540 nm (right) vs. BIH concentration according to the Stern-Volmer equation. Adapted with permission from ref. 107, Copyright 2020 American Chemical Society.

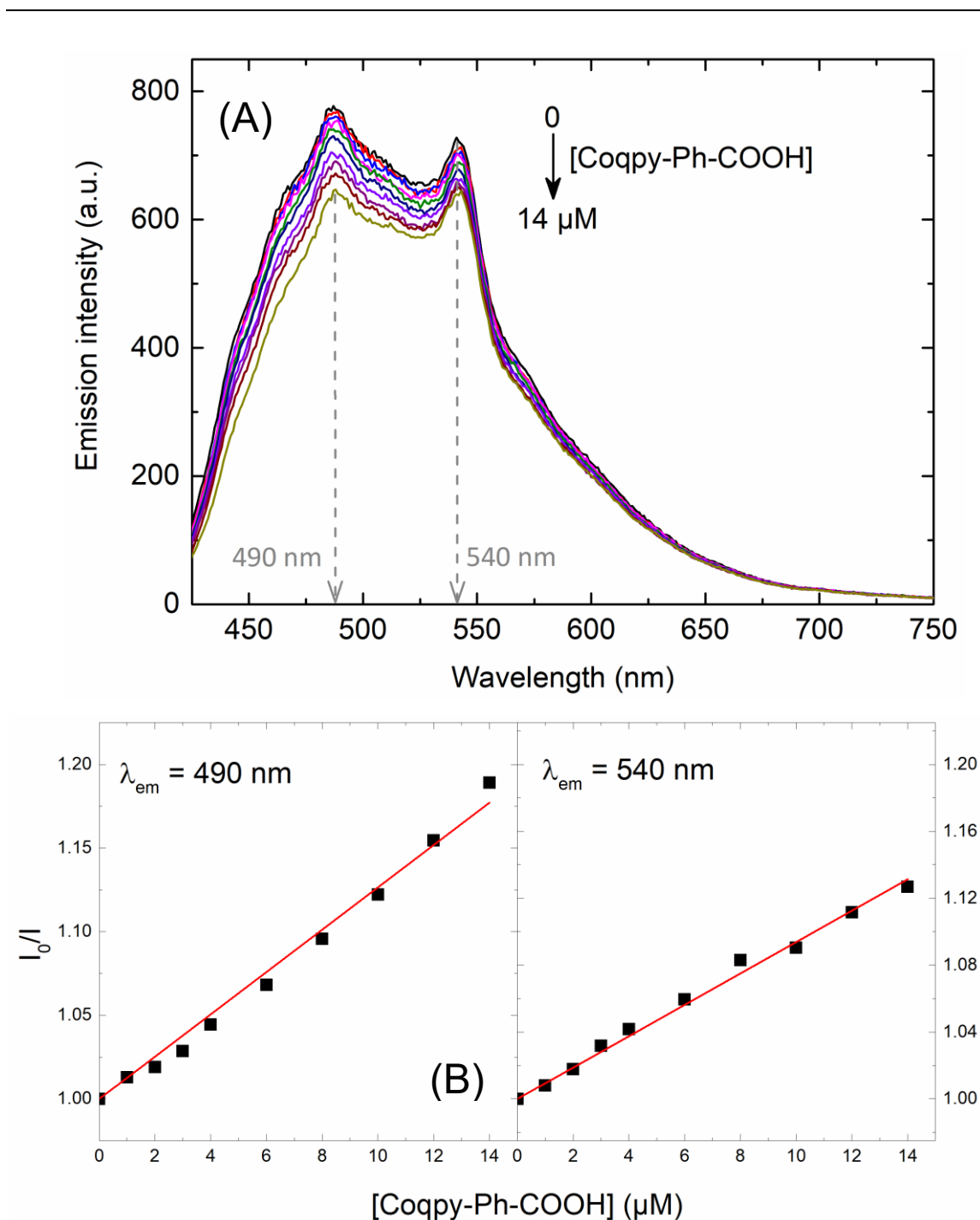


Fig. 3.9 (A) Emission spectra of a 6 mg mpg-C₃N₄ suspension in ACN containing 0 (black), 1 (red), 2 (blue), 3 (magenta), 4 (olive), 6 (navy), 8 (violet), 10 (purple), 12 (wine) and 14 μM (dark yellow) Coqpy-Ph-COOH; (B) linear plot of the emission ratio at 490 (left) and 540 nm (right) vs. Coqpy-Ph-COOH concentration according to the Stern-Volmer equation. Adapted with permission from ref. 107, Copyright 2020 American Chemical Society.

Electron transfer rate constant determination through Stern-Volmer (S-V) analysis (Fig. 3.8(B) and 3.9(B)) requires the excited state lifetime of mpg-C₃N₄. Several studies reported a very short lifetime for C₃N₄ excited states.¹¹⁵⁻¹¹⁷ In another study which investigated excited-states and electron transfer dynamics of g- and mpg-C₃N₄ hybridized with a Ru mononuclear complex, emissive excited states decay was observed with a three-component (from 0.7 to 12 ns) kinetics. However, neither electron acceptors nor hole scavengers can quench these excited states. Generally speaking, k_q will be used to evaluate the rate of electron transfer in quenching experiments. But the excited-state lifetime (τ_0) is needed for calculation (see equation 3.1). Due to the detection limit of the instrument, we chose to use K_{SV} to evaluate the electronic transfer rate, without precisely estimating τ_0 .

We applied Stern-Volmer analysis with the following equation:

$$\frac{I_0}{I} = 1 + K_{SV}[Q] = 1 + k_q\tau_0[Q] \quad (\text{Eq. 3.1})$$

where I_0 and I are the emission intensity without and in the presence of a quencher (respectively), K_{SV} is the Stern-Volmer constant equal to the slope of the linear relationship, k_q is the apparent quenching rate constant, τ_0 the excited-state lifetime without quencher, and $[Q]$ the quencher concentration.

Table 3.3. Stern-Volmer constants for mpg-C₃N₄ emission quenching analysis.

Quencher	K_{SV} @ 490 nm	K_{SV} @ 540 nm
BIH	3.253 ± 0.049	1.826 ± 0.048
Coqpy-Ph-COOH	12650 ± 286	9379 ± 165

In the quenching experiments, the Stern-Walmer constant of the cobalt complex (Table 3.3) is much larger (by a factor > 3900) than that of BIH. It largely counterbalances the smaller catalyst concentration (by a factor of 16). Therefore, even in cases where the exact rate constant cannot be determined, electron transfer is theoretically effective and is likely to occur from mpg-C₃N₄ to the cobalt molecular catalyst.

Photocurrent response has been measured to get insight into the electron transfer (Fig. 3.10). The materials mpg-C₃N₄, Coqpy/mpg-C₃N₄ (obtained by simple mixing of the Coqpy-Ph-COOH and mpg-C₃N₄) and Coqpy@mpg-C₃N₄ were deposited at an FTO electrode, respectively, which was connected to a platinum electrode in a 0.1 M Na₂SO₄ solution without any bias (see Experimental section for details). Upon running 10 consecutive illumination cycles, the current responses of mpg-C₃N₄ and Coqpy/mpg-C₃N₄ were negligible whereas the covalently linked Coqpy@mpg-C₃N₄ assembly showed a significant, quickly rising and stable current response. A slight attenuation was observed after ten cycles, which may result from the spalling of traces materials on the FTO electrode. In sample preparation, the hybrid and conductive glass FTO electrode are only connected by small quantity of Nafion polymer. Under the influence of light and current during the test, it is likely to gradually fall off as the test progresses.

The experiments illustrate that the electron transmission between the two parts is enhanced through the covalent chain.

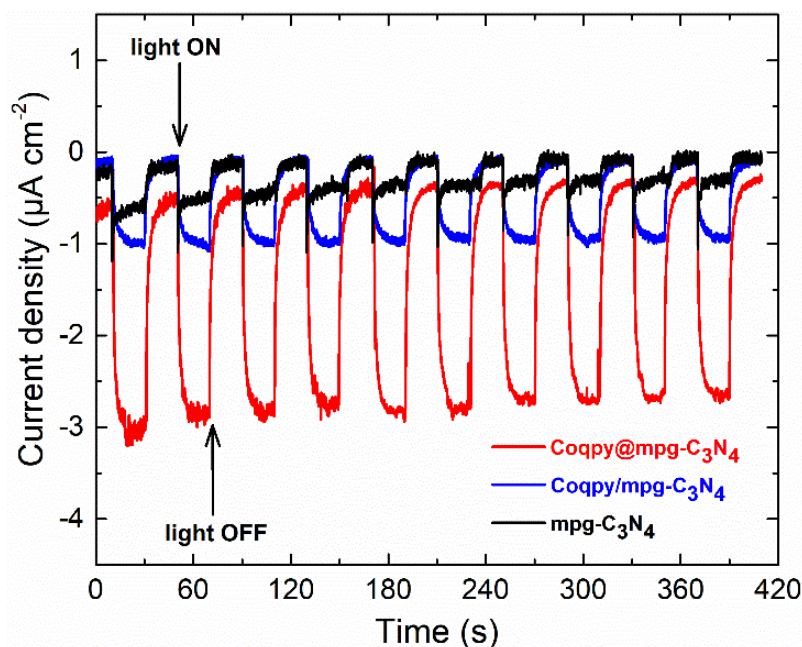


Fig. 3.10 Transient (light on/off) photocurrent responses of mpg-C₃N₄(black), Coqpy/mpg-C₃N₄ (blue) and Coqpy@mpg-C₃N₄ (red) hybrid ink dropped onto a FTO electrode connected to a platinum electrode (no bias, 0.1 M Na₂SO₄ solution). Adapted with permission from 107, Copyright 2020 American Chemical Society.

Electronic impedance spectroscopy (EIS) response of mpg-C₃N₄, Coqpy/mpg-C₃N₄ and Coqpy@mpg-C₃N₄ were further measured (Fig. 3.11). From these data, the charge-transfer resistance of Coqpy@mpg-C₃N₄ is smaller than Coqpy/mpg-C₃N₄ and mpg-C₃N₄, illustrating half the hybrid Coqpy@mpg-C₃N₄ possesses the lowest impedance. It confirms that the covalent linking significantly accelerates the photoexcited charge transfer.

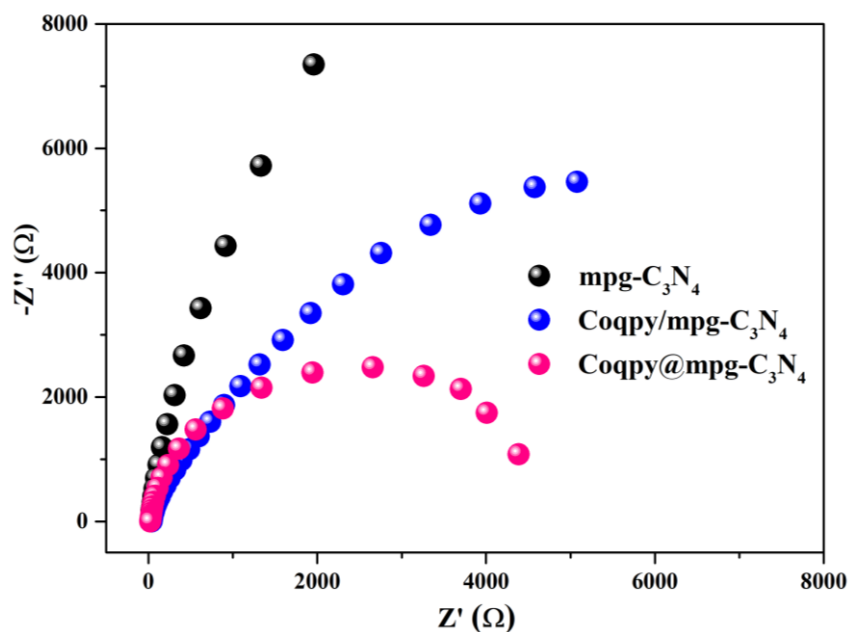


Fig. 3.11 EIS (electrochemical impedance spectroscopy) responses of mpg-C₃N₄ (black), Coqpy/mpg-C₃N₄ (blue) and Coqpy@mpg-C₃N₄ (pink) in the dark. Adapted with permission from 107, Copyright 2020 American Chemical Society.

3.1.4 Stability of the catalytic system

a. Recycling photocatalytic experiments

To further evaluate the stability of this hybrid catalyst during CO₂ reduction reaction, we conducted four successive cycles of experiments with the same batch of catalyst.

For each cycle, the quartz cell was irradiated with visible light for 24 hours in standard Coqpy@mpg-C₃N₄/BIH/PhOH MeCN solution. After each cycle, the hybrid was washed with a large amount of MeCN combined with ultrasonic treatment, and then centrifuged and dried. After that, the hybrid was dispersed again into a fresh ACN

containing BIH and PhOH, then saturated with CO₂ for 30 min to start a new photocatalytic cycle.

All the four catalytic cycles show similar efficiency and selectivity, which indicating a remarkable stability of CO production and asserting the absence of large hybrid degradation during irradiation (Fig. 3.12). Although the number of catalytic cycles decreases with each cycle, a total number of *ca.* 500 catalytic cycles was reached after 96 h. Taking into account that CO₂-to-CO conversion necessitates two electrons, the apparent quantum yield for CO formation is $\Phi = 0.25\%$ (see calculation details in Chapter 1). This recycling strategy also indicates the simple recovery of the catalyst from the solution is promising.

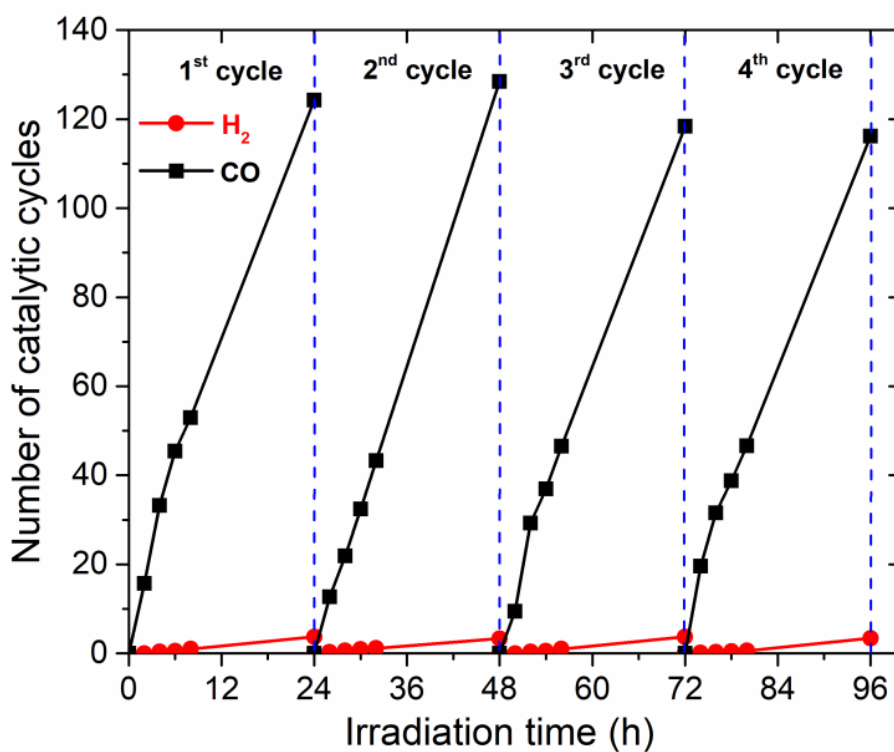


Fig. 3.12 Generation of CO (black squares) and H₂ (red circles) during four consecutive 24 h irradiation cycles using the same hybrid material (see text). Adapted with permission from ref. 107, Copyright 2020 American Chemical Society.

b. X-ray diffractograms and UV-Vis absorption spectra

X-ray diffractograms of complex mpg-C₃N₄, nsg-C₃N₄, Coqpy-Ph-COOH, Coqpy@mpg-C₃N₄ before and after irradiation are shown in Fig. 3.13.

The Coqpy@mpg-C₃N₄ mixed diffraction peaks before and after irradiation include the characteristic diffraction peaks of the complexes at 7.1°, 10.1°, 12.5°, 16.1°, 21.6°, 23.9°, 27.3°, 29.9°. Peak of C₃N₄ is always seen at 27.5°, which is due to the strong diffraction peak of the (002) plane of g-C₃N₄ of heptazine (conjugated aromatic ring). According to the database search and matching, the structure of the hybrid and the porous aluminum silicate zeolite (JCPDS reference card 00-023-0214) match well, and it partially overlaps with the complex and confirming the retention of mpg-C₃N₄ porosity. This porous structure was not observed on mpg-C₃N₄, which may be due to the change of the chemical environment on the surface of the hybrid during the synthesis process.

In the catalyst after the photocatalytic reaction, no characteristic diffraction peak of cobalt oxide was observed. Although the content of cobalt is low, this data cannot provide evidence for the decomposition of the complex into metal oxides or even metal oxides as catalytic centers. Combined with the XPS data in Fig. 3.4, it also confirmed that cobalt is present in Coqpy @ mpg-C₃N₄ before and after photocatalysis, and cobalt is also present in the adsorbed sample Coqpy-mpg-C₃N₄.

In order to evaluate the stability of the complex in the photocatalytic process, the absorption spectra of the compounds in the solution before and after the photocatalytic reaction were also examined. The absorption spectra of PhOH, BIH, qpy-Ph-COOH ligand, Coqpy-Ph-COOH complex and the photochemical mixture before and after irradiation are shown in Fig. 3.14. The UV-Vis absorption spectrum retains the same spectral trend as before irradiation, although the intensity is lower. No characteristic absorption peak of the ligand was observed.

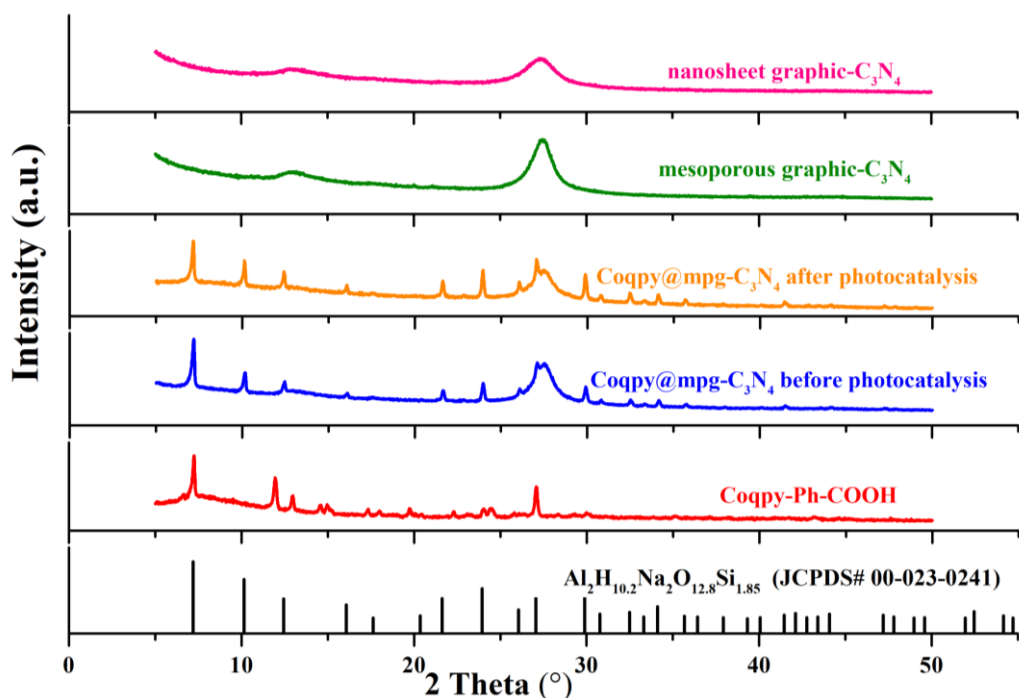


Fig. 3.13 XRD pattern of Coqpy-Ph-COOH molecule (red), Coqpy@mpg-C₃N₄ before photocatalysis (blue), Coqpy@mpg-C₃N₄ after photocatalysis (orange), mesoporous graphic-C₃N₄ (green) and nanosheet graphic (pink) compared to patterns of a sodium aluminum silicate hydrate (a porous zeolite, JCPDS reference card # 00-023-0241, black). Adapted with permission from ref. 107, Copyright 2020 American Chemical Society.

The Coqpy@mpg-C₃N₄ hybrid material we synthesized is the first catalytic system made of a molecular catalyst covalently immobilized on carbon nitride for CO₂RR. The effective and selective covalent connection of molecular catalysts and polymeric materials seems to be a promising method for catalytic reduction of CO₂, leading to good control of the structure of the catalyst and excellent selectivity and activity.

Among reports of earth-abundant metal-based catalysts combined with carbon nitride-based materials, Coqpy@mpg-C₃N₄ not only shows high selectivity and CO production activity, but also shows long-term stability. Therefore, it inherits the high selectivity of molecular catalysts and the excellent stability of solid materials.

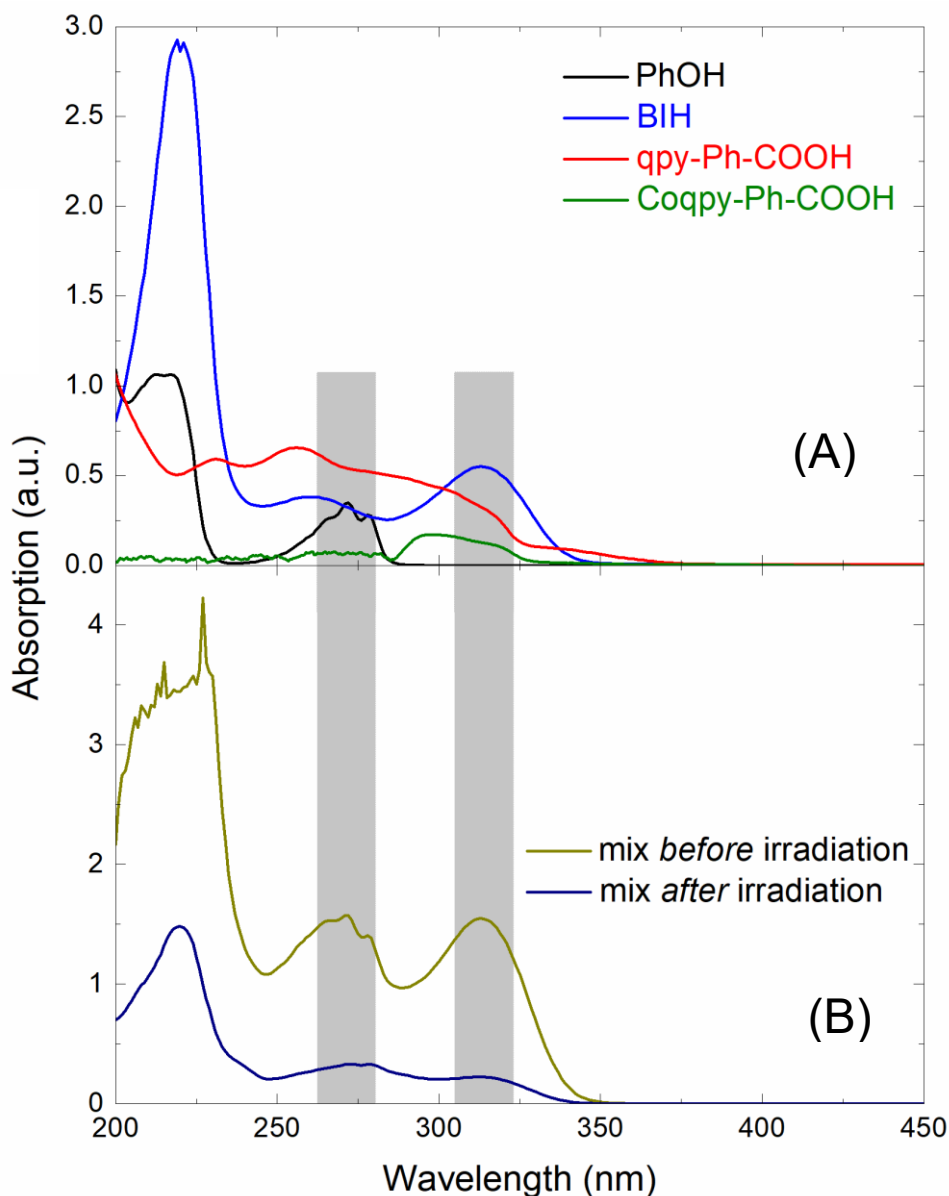


Fig. 3.14 UV-vis absorption spectra of (A) 0.3 mM PhOH (black), 0.36 mM BIH (blue), qpy-Ph-COOH ligand (red) and Coqpy-Ph-COOH (olive) in ACN (concentrations of the ligand and complex cannot be determined due to low solubility) and (B) photochemical solution mixture containing all components (see entry 1, Table 3.1) before (dark yellow) and after (navy) reaction in ACN. These solutions were filtered and diluted 50 times with MeCN. Adapted with permission from ref. 107, Copyright 2020 American Chemical Society.

This type of combination takes into account the independent adjustment capabilities of the molecular complex structure and inorganic material structure, and there is still a lot of room for adjustment and improvement in the association between the two parts. Such

excellent performances provide new development ideas for the development of highly active catalytic materials, and not only for the reduction of carbon dioxide. Other catalytic reaction can be envisioned, while a better understanding of charge transport and transfer properties with the hybrid materials still needs to be achieved.

3.2 Selective reduction of CO₂ to CO or HCOO⁻ under visible light with Coqpy covalently grafted on a graphene material (Coqpy@GA)

Graphene consists of a single layer of carbon atoms arranged in a two-dimensional honeycomb lattice, and its derivatives are well-known materials suitable for anchoring molecules due to their adjustable porosity, high electronic and thermal stability, and chemical inertness in most reaction conditions.¹¹⁸⁻¹²⁰ Recently, various graphene derivatives have been developed, which are characterized by extremely rich surface chemical properties, affording a wide range of materials for advanced functionalization schemes. Due to the simplicity and scalable synthesis, graphene oxide is the most widely studied matrix.¹²¹ However, the control of the rich oxygen-containing functional groups on the surface is a difficult task, including tertiary alcohols, epoxide, carboxyl and carbonyl groups.¹²² Graphene acid (GA) has been synthesized and investigated as a graphene layer with the basal plane densely and homogeneously decorated by carboxylic groups.¹²³

Owing simple synthesis, easy scalability, high surface area and electronic conductivity, GA can afford both precise control on the type of surface groups and maintenance of the sp² network of pristine graphene, which makes this material an interesting substrate for chemical functionalization.

3.2.1 Synthesis and characterization of Coqpy@GA

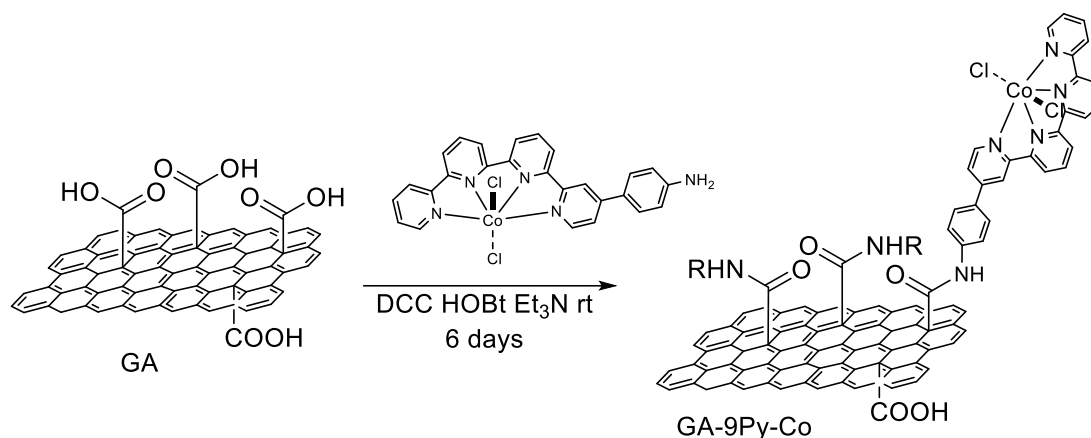
a. Synthesis of graphene acid (GA)

GA was synthesized according to a 2-steps protocol described in the literature.¹²⁴⁻¹²⁶ Briefly, 0.12 g (~4 mmol) of fluorographite was suspended in 15 mL DMF and sonicated

under nitrogen atmosphere for 4 h. Then, 1.06 g (16 mmol) of KCN were added to the suspension and let react at 130°C for 24 h, in order to promote the nucleophilic substitution of fluorine atoms with cyano groups. The suspension was diluted with 15 mL of acetone and washed by centrifugation with fresh and hot (80 °C) DMF, dichloromethane, acetone, ethanol and water for 3 times. In a second step, the so formed cyanographene was hydrolysed in 20% HNO₃ under reflux at 100°C for 24 h, to convert the –CN groups into –CO₂H groups. Finally, the material obtained was washed by following the same centrifugation protocol described above. The preparation of this material was done by ours collaborators at Padova University in Italy.

b. Functionalization of GA with CoqpyNH₂

The coupling of GA with the derivatized CoqpyNH₂Cl₂ molecule was achieved employing carbodiimide chemistry, which is often used for peptide synthesis since it preserves the structure of the organic substrates (Scheme 3.2). In order to activate the –COOH groups of GA, 20 mg of GA were suspended in 20 mL of N,N-dimethylformamide (DMF) and 4 mg (0.03 mmol) of hydroxybenzotriazole (HOBt) and 4 µL (0.03 mmol) of trimethylamine were added. The mixture was kept under stirring for 45 min at 0 °C in an ice bath. Then, the ice bath was removed and 6 mg (0.03 mmol) of dicyclohexyl carbodiimide (DCC) and 5 mg (0.009 mmol) of the amino-functionalized Cobalt quaterpyridine modified with amino phenyl group were added (Scheme 1). The reaction mixture was kept under stirring at room temperature (RT) for 6 days. The resulting solid was separated by filtration using a 0.2 µm polytetrafluoroethylene (PTFE) membrane, and thoroughly washed with 3x50 mL of fresh DMF, 3x50 mL of a 1:1 DMF:water mixture, 3x50 mL of methanol and 2x50 mL of acetone. After each filtration step, the powder was suspended in the fresh washing solvent and sonicated for 5 min in order to remove the eventual physisorbed species. Finally, the sample was dried under vacuum to obtain the GA-Coqpy.



Scheme 3.2 Functionalization route of GA with the amino-functionalized Cobalt quaterpyridine molecule.

3.2.2 Characterization of GA and GA-Coqpy

a. Surface density of $-\text{COOH}$ analysis

Graphene acid is a promising oxidized derivative of graphene, whose basal plane is strongly and selectively decorated with $-\text{COOH}$ groups. The amount of $-\text{COOH}$ groups is around 6 at. %, which is higher than in pristine Graphene oxide (GO). In addition, it has been demonstrated both experimentally and theoretically that GA is also conductive, owning an electrical conductivity very close to pristine graphene. Therefore, it represents a very appealing platform for immobilizing molecular catalysts by covalent functionalization, especially for energy related applications.

b. Raman spectra and FT-IR spectra analysis

In order to confirm the covalent functionalization of GA with the CoqpyCl_2 molecule, the preservation of the CoqpyCl_2 molecule structure and the interaction between the molecule and GA substrate, different characterization analysis were performed.

Vibrational spectroscopies confirmed the successful formation of amide bonds. Fig. 3.15 shows the Raman spectra for the pristine GA, GA-Coqpy and amino-modified CoqpyCl_2 samples. The Raman spectrum of GA shows the characteristic D (1350 cm^{-1}), G (1590 cm^{-1}), 2D (2700 cm^{-1}) and D+D' (2900 cm^{-1}) bands of graphene, whereas the one

of the amino-modified CoqpyCl₂ molecule shows several bands in the 500-1700 cm⁻¹ range. The GA-Coqpy sample mainly shows the D, G, 2D and D+D' bands characteristic of GA; however, it is also possible to observe the presence of some bands characteristic of the CoqpyCl₂ molecule overlapping with those of GA, confirming its immobilization on GA. For example, one can see a broad band between 600 and 700 cm⁻¹, and an increase of the intensity at around 1500 cm⁻¹, which perfectly match with the bands associated to the CoqpyCl₂ molecule. An increase of the I_D/I_G ratio for the functionalized sample (I_D/I_G = 1.07), compared to that of the pristine GA (I_D/I_G = 1.04), is also observed. This increase is typically associated with the introduction of defects in the structure of the graphene layer and may be interpreted as confirmation of the functionalization.

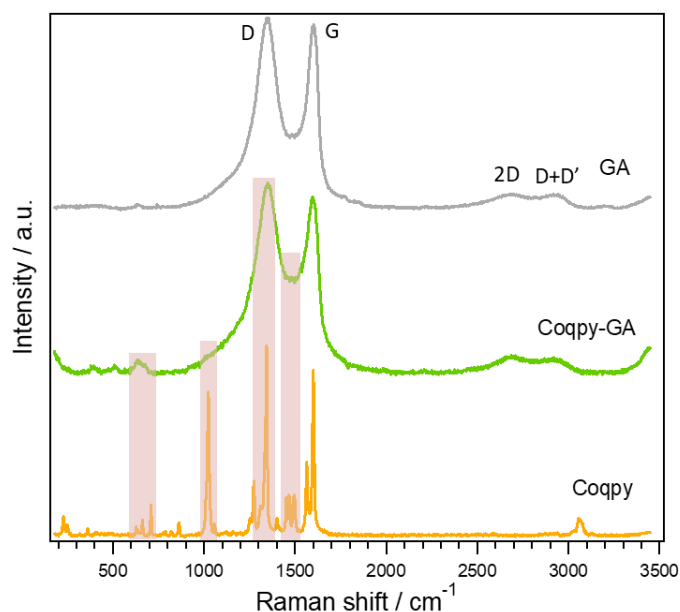


Fig. 3.15. Raman data of pristine GA, GA-Coqpy and ammino-modified CoqpyCl₂ (Coqpy-NH₂) molecule.

The formation of amide bonds is inferred from the FTIR spectroscopy results reported in Fig. 3.16. The presence of -COOH groups in the GA is confirmed by the bands at 1710 cm⁻¹ and 3421 cm⁻¹, related to the C=O and C-OH stretching in the carboxylic groups, respectively. After the coupling with the CoqpyNH₂Cl₂ molecule, the band at 3421 cm⁻¹ decreases due to the reaction between the -COOH groups of GA and the -NH₂ groups of the cobalt molecule, with the subsequent formation of the covalent bond. This is also

confirmed by the shift of the C=O stretching band from 1710 cm^{-1} (C=O in acid group) to 1699 cm^{-1} (C=O in amide group), further confirming the formation of the –CONH– group. In addition, characteristic bands of the amino-modified CoqpyCl₂ molecule are observed in the GA-Coqpy FTIR spectrum, proving the presence of cobalt quaterpyridine in the hybrid sample.

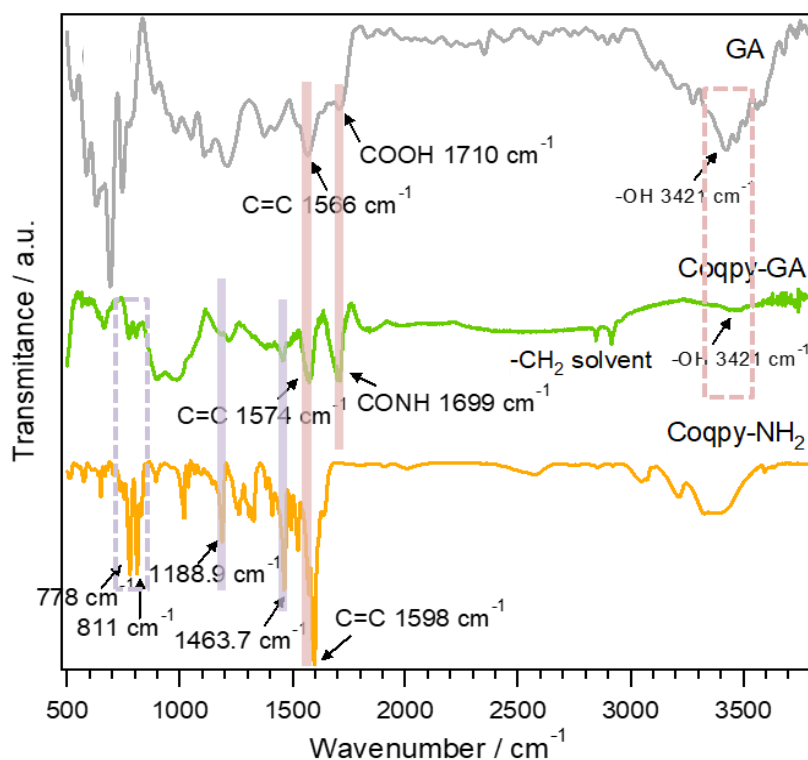


Fig. 3.16 FTIR data of pristine GA, GA-Coqpy and amino-modified CoqpyCl₂ molecule.

Therefore, vibrational spectroscopies strongly suggest that the molecule was incorporated to the GA scaffold via covalent bonds and that the structure of both the substrate and the molecule are preserved by employing our soft functionalization procedure.

c. XPS analysis

Fig. 3.17 as well as Tables 3.4 and Table 3.5 show the XPS results for the GA-Coqpy hybrid. The C 1s region of GA is also reported for comparison. The C 1s spectrum of the two samples is centered at 284.4 eV, which is attributed to the graphitic component (sp^2

hybridized carbon atoms). The component centered at 285.4 eV is associated to sp^3 hybridized carbon atoms (C sp^3) and constitutes the 11.7 at. % of GA. After the immobilization of the Cobalt complex, it increases up to 22.2 at. % due to the introduction of the Co-complex, since this component overlaps with the C-N one. GA contains oxygen species, like alcohols (286.5 eV), epoxy (287.1 eV), carbonyl (287.8 eV) and carboxylic (288.9 eV) groups (Table 3.4). After the coupling, the amount of the different oxygen groups does not vary significantly, except in the case of the carboxylic groups where a decrease from 5.6 at. % to 3.7 at. % is observed. This is attributed to the fact that these later groups are involved in the covalent coupling with the Co complex, as shown by FTIR spectroscopy.

Regarding the N 1s region, it was deconvoluted into three components centered at 398.6 eV, 399.8 eV and 401.2 eV, which are ascribed to C=N, N-Co and C-N-H bonds, respectively. It is interesting to note that the ratio between the N-Co and C-N-H components is close to 4:1 (Table 3.5), confirming that the Co complex contains four nitrogen atoms bonded to cobalt for each $-NH_2$ terminal group able to participate in the covalent coupling with GA. It suggests the preservation of the molecule during the functionalization treatment.

The binding energy (BE) and the shape of the Co 2p spectrum indicate that the oxidation state of Co is +2 as expected, in accordance with the presence of a $Co-N_4$ structure.

The surface composition calculated from the XPS data is 68.2 at. % C, 26.4 at. % O, 4.2 at. % N and 1.3 at.% Co (5.5 wt.%). The comparison of the amount of Co atoms immobilized on the GA substrate (1.3 at. %) and the amount of carboxylic groups consumed during the coupling process (1.7 at. %) suggests that almost one Co atom is incorporated for each covalent bond formed between the Co complex and GA.

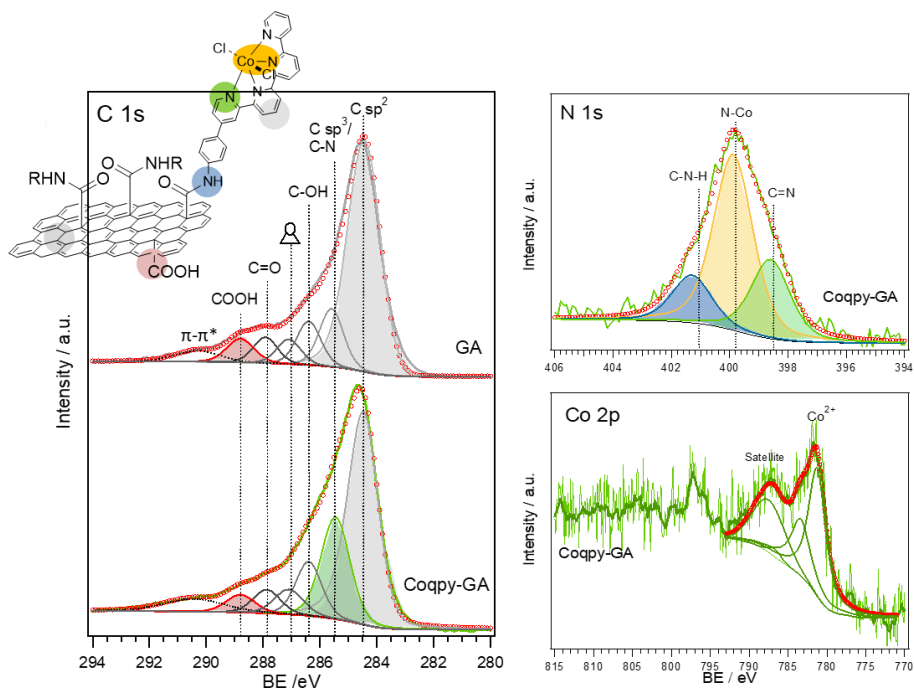


Fig. 3.17 C 1s, N1s and Co 2p XPS spectra for GA-Coqpy sample and their corresponding deconvolution into single chemical components. The C 1s region of GA is also shown for comparison.

Table 3.4 Analysis of the C 1s region for GA and GA-Coqpy. For each component, the binding energy and the amount (at. %) is provided.

Sample	C sp ²	C sp ³ /C-N	C-OH	Epoxy	C=O	COOH
GA	284.4 eV	285.4 eV	286.4 eV	287.1 eV	287.9 eV	288.8 eV
	63.7 %	11.7 %	8.8 %	5.0 %	5.2 %	5.6 %
Coqpy-GA	284.4 eV	285.4 eV	286.4 eV	287.1 eV	287.9 eV	288.8 eV
	53.0 %	22.2 %	10.5 %	5.4 %	4.9 %	3.9 %

Table 3.5 Analysis of the N 1s region for GA-Coqpy. For each component, the binding energy and the amount (at. %) are provided.

Sample	C=N	N-Co	C-N-H
Coqpy-GA	398.6 eV	399.8 eV	401.2 eV
	26.2 %	58.1 %	15.7 %

d. XAS analysis

Fig. 3.18 shows the *ex situ* XANES and Fourier transform (FT) EXAFS spectra for the GA-Coqpy hybrid and the amino-modified Co complex at the Co K edge, as well as for oxides used as reference to establish correlation between the K-edge excitation energy

and the metal oxidation state. For the two samples, the edge position indicates that the oxidation state of Co is close to +2 as expected. Comparing the XANES region for the immobilized and the free Co molecule, a slight difference in the pre-edge can be observed, which is also reflected in the FT EXAFS spectra.

Fig. 3.19 shows the fitted FT EXAFS spectra fitted by using the model reported by Henke *et al.*¹²⁷ and the corresponding k -space spectra. The fitting results are summarized in Table 3.6. The amino-modified CoqpyCl₂ molecule was fitted with a Co-N shell with 4 nitrogen atoms at 1.89 Å, a Co-Cl shell with 2 chlorine atoms at 2.21 Å, and a Co-C shell with 6 carbon atoms at 2.73 Å. After the covalent bonding with GA, some differences were observed in the Coqpy unit. A similar effect has already been reported in the literature for the grafting of organometallic species to carbon supports. So we can speculate on this possibility that the molecule lost the two chlorine atoms and a new interaction between cobalt and oxygen from the –COOH groups of GA substrate was formed. The new Co-O interaction caused a stretching of the Co-N (2.03 Å) and Co-C (2.94 Å) bonds, which could have an effect on the catalytic activity.¹²⁸⁻¹³¹

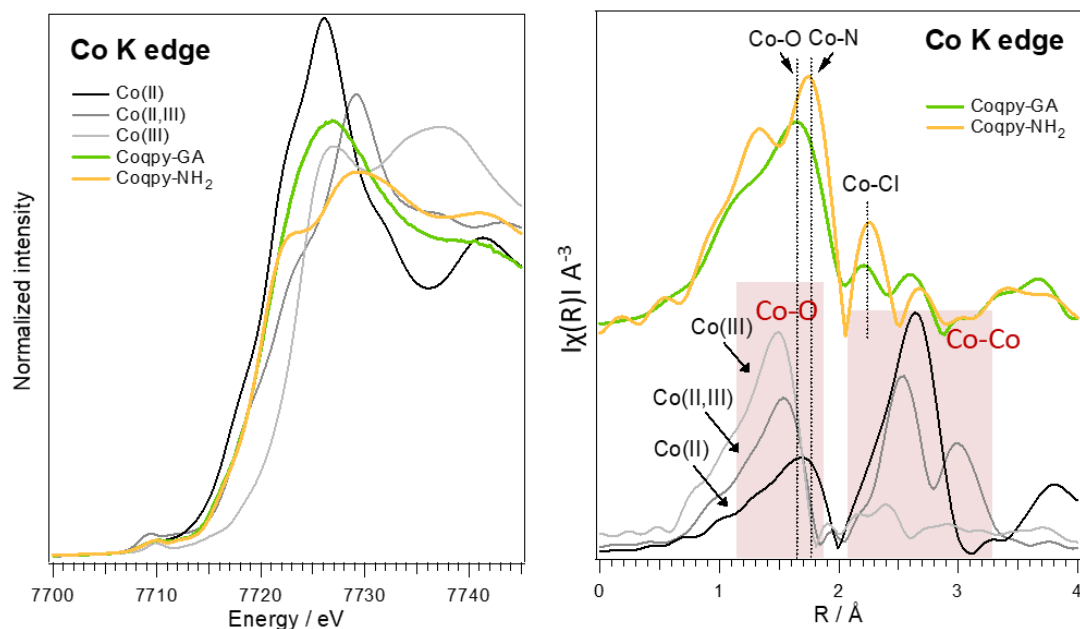


Fig. 3.18 XANES (left panel) and Fourier transformed EXAFS (right panel) spectra at the Co K edge for the GA-Coqpy hybrid and the amino-modified CoqpyCl₂ molecule.

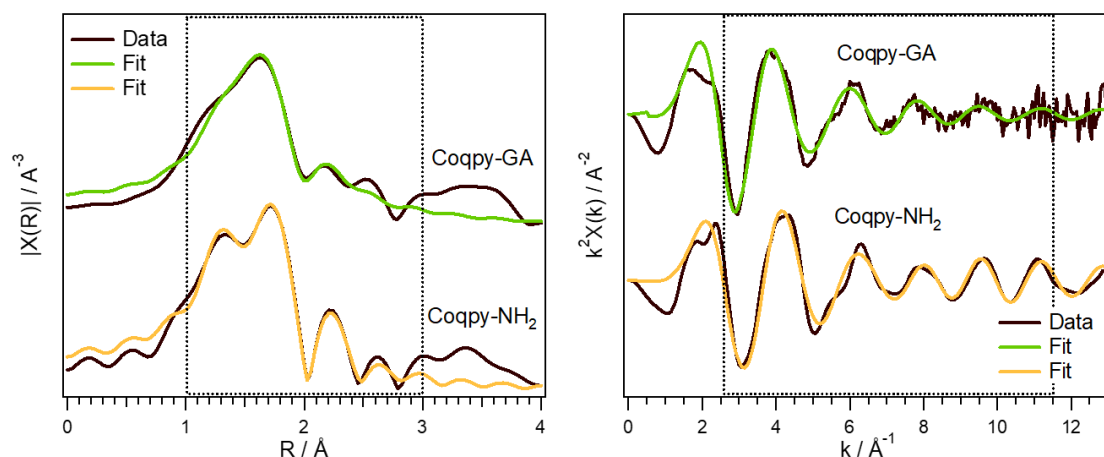


Fig. 3.19 FT EXAFS spectra (left panel) and the corresponding k^2 weighted data at the Co K edge (right panel) for the GA-Coqpy hybrid and the amino-modified CoqpyCl₂ molecule. The black curves represent the experimental data and the coloured ones the fit for GA-Coqpy (green) and CoqpyNH₂ (yellow). The dotted squares indicate the R and k ranges used in the fits.

Table 3.6 Structural parameters obtained for the amino-modified CoqpyCl₂ from fitting the Co K edge EXAFS data acquired under air. ($R_f = 0.010$, $\Delta E_0 = 5.3 \pm 1.5$ eV).

Sample	Shell	N	R/Å	$\sigma^2 \times 10^4 / \text{Å}^2$	R_f
Coqpy-NH ₂	Co-N	4	1.894 ± 0.018	78 ± 25	0.010
	Co-Cl	2	2.213 ± 0.010	21 ± 12	
	Co-C	6	2.732 ± 0.035	99 ± 41	
Coqpy-GA	Co-N	4	2.038 ± 0.036	135 ± 86	0.016
	Co-O	1	2.118 ± 0.044	16 ± 41	
	Co-C	6	2.948 ± 0.087	293 ± 124	

e. UV-Vis diffuse reflectance spectroscopy analysis

The interaction between light and the samples was investigated by UV-Vis diffuse reflectance spectroscopy and the results are shown in Fig. 3.20. GA exhibits a constant absorption in all the visible range, while the Co complex shows a wide absorption band between 650 and 400 nm. The GA-Coqpy shows the same behaviour as GA in the 400-800 nm range, which could indicate that only GA absorbs the light. Below 400 nm, the

decrease of the absorbance is sharper than that for GA but similar to that of the Co complex.

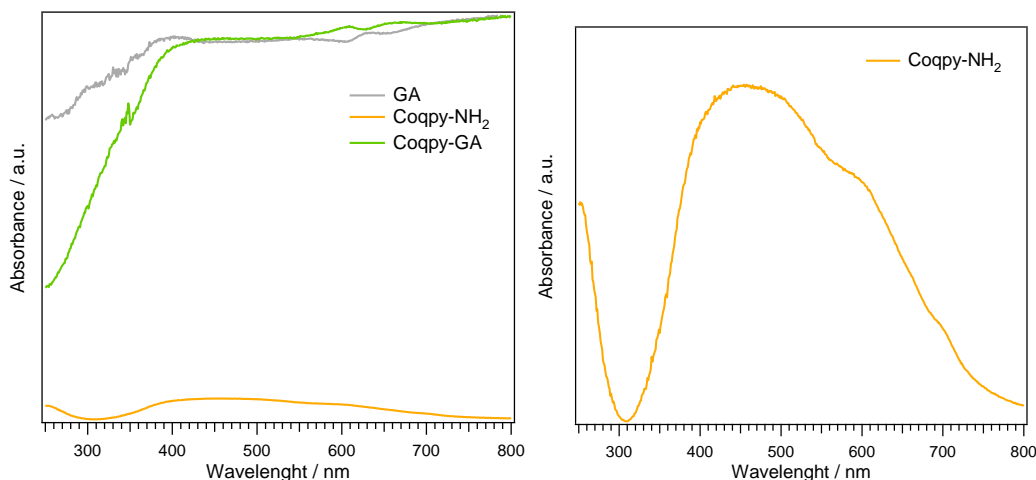


Fig. 3.20 UV-Vis diffuse reflectance spectra for pristine GA, GA-Coqpy and amino-modified CoqpyCl₂ molecule.

3.2.3 Catalytic performance for CO₂ reduction under visible-light

a. General procedure of photocatalytic CO₂ reduction experiment

Photocatalytic CO₂ reduction with GA-Coqpy was conducted in a quartz cell with an inner volume of 6 mL. GA-Coqpy hybrid material (1 mg) was dispersed into a MeCN solution (3 mL) and used as a stock suspension. For each photocatalytic experiment, 60 μ L hybrid stock suspension and a tiny stirring bar were poured into the quartz cell. After adding a sacrificial donor (BIH) as well as a certain amount of weak acid or base, the quartz cell was sealed with a rubber septum and bubbled with CO₂ for *ca.* 30 min. Then, the suspension was irradiated with a solar simulator equipped with a 100 W Xenon lamp and an optical filter ($\lambda \geq 400$ nm). The temperature was controlled during each experiment by a water bath at 298 K. Control experiments (with no catalyst, no CO₂ or no light) and comparison experiments (using either Coqpy + GA, CoCl₂ + GA, CoO_x + GA and Coqpy/Al₂O₃) were conducted in the same conditions than the complete catalytic system.

b. Photocatalytic CO₂ reduction

The visible-light-driven catalytic reaction catalyzed by the GA-Coqpy hybrids was achieved with high selective conversion of CO₂ to carbon monoxide or formate by changing the reaction conditions. We further describe in the following experiments done in acidic conditions and basic conditions, respectively.

b1. Photocatalytic CO₂ reduction to CO

Besides BIH as sacrificial donors, weak acids such as phenol (PhOH) or trifluoroethanol (TFE) were employed in the photocatalysis to provide protons in this part.

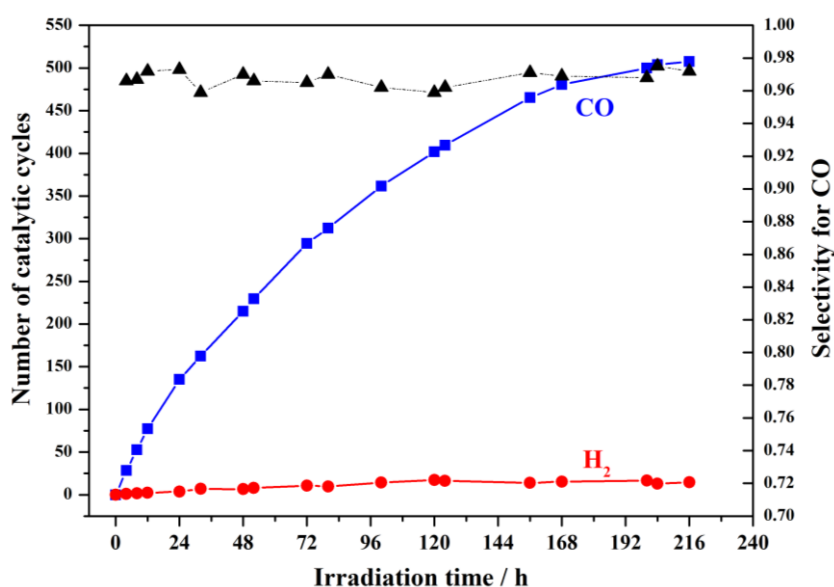


Fig. 3.21 Photocatalytic CO₂ reduction products and selectivity as a function of time in CO₂-saturated ACN solution for reactions performed in the presence of 0.1 M PhOH for a suspension containing GA-Coqpy (Coqpy 15 μM), 0.05M BIH ($\lambda > 400$ nm).

The concentration of the complex Coqpy employed in the photocatalytic reaction was optimized to be 15 μM (compare entries 1-3, Table 3.7). The concentration of the reactants was optimized through experiments 5 and 6, and then two sets of photocatalytic experiments were conducted using phenol and trifluoroethanol, respectively. First of all, two long-term photocatalytic reaction of CO₂ were carried out. After more than 200 hours of light irradiation, the conversion of CO₂ to carbon monoxide can reach turnover number as high as 513 (with Phenol, Table 3.7, entry 5) or 437 (with TFE, Table 3.7, entry 4), corresponding to high selectivities of 97% or 98%, respectively.

Table 3.7 CO₂ reduction with Coqpy catalyst covalently attached to GA in acidic conditions under visible light ($\lambda > 400$ nm).

	entry	catalyst ^a	conditions	Time/h	product (μmol)/ TON _{CO} ^b / selectivity _{CO}
Experimental Group	1	GA-Coqpy 187 μM	0.025M BIH, 0.5 M PhOH	51	0.13 1.81/9.7/93.1%
	2	GA-Coqpy 19 μM	0.05M BIH, 0.1 M PhOH	24	0.03 1.58/83/98.5%
	3	GA-Coqpy 7 μM	0.05M BIH, 0.1 M PhOH	45	0.23 3.39/162/93%
	4	GA-Coqpy 15 μM	0.05M BIH, 0.1 M TFE	218	0.13 6.6/437/98%
	5	GA-Coqpy 15 μM	0.05M BIH, 0.1 M PhOH	222	0.27 7.6/513/97%
	6	GA-Coqpy 15 μM	0.05M BIH, 0.05 M PhOH	230	0.23 6.4/432/96.5%
Control Group	7	GA+Coqpy 15 μM	0.05M BIH, 0.1 M TFE	152	trace 0.18/12/99%
	8	GA+Coqpy 15 μM	0.05M BIH, 0.1 M PhOH	152	0.006 0.192/12.8/97%
	9	GA+CoCl ₂ 15 μM	0.05M BIH, 0.1 M TFE	89	0.005 0
	10	GA+CoCl ₂ 15 μM	0.05M BIH, 0.1 M PhOH	89	0.003 0
	11 ^c	GA-Coqpy 15 μM	0.05M BIH, 0.1 M TFE	63	trace 0
	12 ^c	GA-Coqpy 15 μM	0.05M BIH, 0.1 M PhOH	76	0.006 0
	13 ^d	GA-Coqpy 15 μM	0.05M BIH, 0.1 M TFE	76	0.008 0.012/1.13/60%
	14 ^d	GA-Coqpy 15 μM	0.05M BIH, 0.1 M PhOH	63	0.013 0.018/1.7/58%

^a reaction conditions: 0.02 mg catalyst in a CO₂-saturated ACN solution containing BIH and PhOH. A 6 mL quartz cell with a septum was used as the reaction vessel; and a solar simulator equipped with a 100 W Xenon lamp and a 400 nm optical filter was used as irradiation source.

^b relatively to the amount of Coqpy or CoCl₂.

^c under an argon atmosphere.

^d in the dark.

Control experiments were designed to further evaluate the catalytic performance of GA supported Coqpy catalyst. Physically mixed GA and Coqpy and cobalt salt have been

employed as catalysts. The mixed sample show negligible hydrogen and CO evolution with PhOH (Table 3.7, entry 8) or TFE (Table 3.7, entry 7). While the cobalt salt as catalyst only generates traces of hydrogen (Table 3.7, entries 9-10). Moreover, control experiments in dark or under argon also illustrated the necessity of photoirradiation and CO₂ (Table 3.7, entries 11-14).

b2. Photocatalytic CO₂ reduction to formate

First, triethylamine was chosen to replace phenol to create alkaline conditions. In the presence of BIH, carbon dioxide was reduced to CO with a selectivity of 69% and a TON of 194 upon 79 hours of irradiation (Table 3.8, entry 1). When the triethylamine in the system was replaced with triethanolamine, the catalytic selectivity changed drastically. The liquid formate became the main product with a TON of 260 and a selectivity of 97%, while the gas-phase product only included a small amount of hydrogen (Table 3.8, entry 2). The amount of catalyst and BIH used in the system also impacted catalysis (Table 3.8, entries 3-5). After optimization, when the amount of the composite catalyst is adjusted to a concentration of 7 μM, the turnover number for formic acid reached 330 and the selectivity was 99% (Table 3.8, entry 5, fig. 3.22).

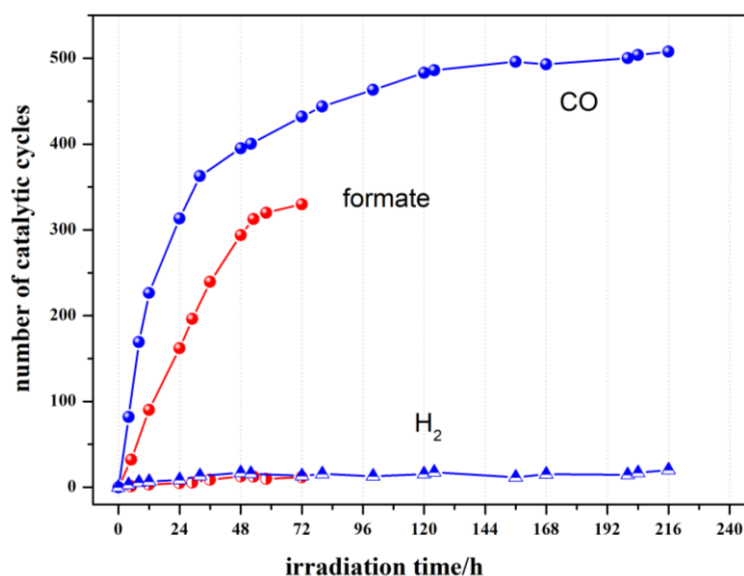


Fig. 3.22 Photocatalytic CO₂ reduction products as a function of time in CO₂-saturated ACN solution for reactions performed in the presence of 0.1 M PhOH (blue) or 1.51 M TEOA (red) in a suspension containing GA-Coqpy (Coqpy 15 μM), 0.05M BIH ($\lambda > 400$ nm).

In addition to the optimal amount of catalyst, the amount of electron sacrificial agent was also adjusted to achieve the best catalytic efficiency. Control experiments were then conducted under alkaline conditions to evaluate the carbon dioxide conversion effect of the catalyst. Similar to the experimental protocol under acidic conditions, physically mixed GA and Coqpy as well as cobalt salt (CoCl₂) can not trigger the CO₂ reduction (Table 3.8, entries 6-7). Also, the GA-Coqpy as catalyst only generates traces of hydrogen under argon (Table 3.8, entry 8), and shows no catalytic activity in the dark (Table 3.8, entry 9).

Table 3.8 CO₂ reduction with Coqpy catalyst covalently attached to GA in basic conditions under visible light ($\lambda > 400$ nm).

entry	catalyst ^a	conditions	time h	product (μmol)/ TON _{formate} ^b / Selectivity _{formate} (%)		
				H ₂	formate	
Experiment Group	1	GA-Coqpy 15 μM	0.025M BIH, 1.44 M TEA	72	1.3	2.9co/194co /69co ^e
	2	GA-Coqpy 15 μM	0.025M BIH, 1.51 M TEOA	96	0.11	3.92/262/97
	3	GA-Coqpy 153 μM	0.025M BIH, 1.51 M TEOA	28	0.006	0.31/2.1/98
	4	GA-Coqpy 15 μM	0.05M BIH, 1.51 M TEOA	30	0.06	3.62/242/98
	5	GA-Coqpy 7 μM	0.025M BIH, 1.51 M TEOA	45	0.07	7.05/330/99
Control Group	6	GA + Coqpy 15 μM	0.025M BIH, 1.51 M TEOA	48	0	0
	7	GA + CoCl ₂ 15 μM	0.025M BIH, 1.51 M TEOA	89	0	0
	8 ^c	GA-Coqpy 15 μM	0.05M BIH, 1.51 M TEOA	63	trace	0
	9 ^d	GA-Coqpy 15 μM	0.025M BIH, 1.51 M TEOA	63	0	0

^a reaction conditions: 0.02 mg catalyst in a CO₂-saturated ACN solution containing BIH, TEA, or TEOA. A 6 mL quartz cell with a septum was used as the reaction vessel; and a solar simulator equipped with a 100 W Xenon lamp and a 400 nm optical filter was used as irradiation source.

^b relatively to the amount of Coqpy or CoCl₂.

^c under an argon atmosphere.

^d in the dark.

^e reduction products are H₂ and CO.

c. Investigation on formate generation with Coqpy@GA

With addition of isopropanol, no CO has been detected in these conditions (Table 3.9,

entries 2-3). Replacing TEOA with TEA and adding PrOH in the photocatalysis, the production of formate was suppressed and hydrogen increased. (entry 2) As the concentration of PrOH increases, the production of formate decreases, and the yield of hydrogen increases (entry 3). When TEOA and isopropanol were simultaneously added to the solution (entries 2-3), the production of H₂ was promoted while the production of formate was not completely suppressed but was weakened. Then, isopropanol (*pKa* = 16.5) was replaced by phenol (*pKa* = 9.95, entry 4), the production of formic acid was further reduced and the hydrogen generation was greatly increased. And some CO was also detected. After that, a photocatalysis was conducted with molecular Coqpy in MeCN solution of BIH and acetic acid (*pKa* = 4.76). Hydrogen generation was boosted to a TON of 118 with a little amount of CO (TON = 18) produced (Table 3.9, entry 6).

Table 3.9 GA@Coqpy photocatalytic CO₂-to-formate conversion with additional acid (CH₃COOH, PrOH and PhOH) under visible light ($\lambda > 400$ nm).

entry	catalyst ^a	conditions ^a	time h	product (μmol)/TON ^b /selectivity%		
				H ₂	CO	formate
1 [*]	GA-Coqpy 7 μM	0.025M BIH, 1.51 M TEOA	45	0.07	0	7.05/330/99
2	GA-Coqpy 7 μM	0.025M BIH, 1.51 M TEOA, 40 mM PrOH	45	0.20/9/11	0	1.50/70/89
3	GA-Coqpy 7 μM	0.025M BIH, 1.51 M TEOA, 2M PrOH	45	0.66/31/57	0	0.49/23/43
4	GA-Coqpy 7 μM	0.025M BIH, 1.51 M TEOA, 0.3 mM [Ru(bpy) ₃] ²⁺ , 40 mM PhOH	45	2.70/127/4 2	2.87/135/44	0.91/43/14
5	Coqpy 20 μM	0.025M BIH, 1.51 M TEOA, 0.5M CH ₃ COOH	24	7.1/118/86	1.1/18/13	0
6 ^c	Coqpy 5 μM	0.3 mM [Ru(bpy) ₃] ²⁺ , 0.1 M BIH, 0.5 M TEOA	80 min	0.23/23/1	26.6/2660/9 8	0.35/35/1

^a reaction conditions: 0.02 mg catalyst in a CO₂-saturated ACN solution containing BIH and PrOH. A 6 mL quartz cell with a septum was used as the reaction vessel; and a solar simulator equipped with a 100 W Xenon lamp and a 400 nm optical filter was used as irradiation source.

^b relatively to the amount of Coqpy.

^{*} the optimized conditions of the CO₂-to-formate conversion.

^c irradiation using blue LED (460 nm), data referenced from our previous work.⁸²

d. Calculation of apparent quantum yield in photocatalytic CO₂ reduction

The number of incident photons was calculated using the classical iron ferrioxalate (K₃Fe(C₂O₄)₃) chemical actinometer, following the procedure reported previously and using known parameters for calculations. We determined that the number of incident photons reaching the sample was $(2.18 \pm 0.17) \times 10^{19}$ photons per hour. The CO₂-to-CO reduction being a two-electron process, the overall quantum yield Φ of the process was determined using the following equation:

$$CO\% = \frac{\text{Number of CO molecules formed} \times 2}{\text{Number of incident photons}} \times 100\%$$

Taking 513 as the turnover number for CO (Table 3.7, entry 8), we obtain an apparent quantum yield Φ of about 0.57 % after 222 h of irradiation.

Taking 330 as the turnover number for formate (Table 3.8, entry 1), we obtain an apparent quantum yield Φ of about 0.37 % after 72 h of irradiation.

e. Isotope labelled experiments

Both CO and formate have been confirmed to be issued from CO₂ by using labelled ¹³CO₂.

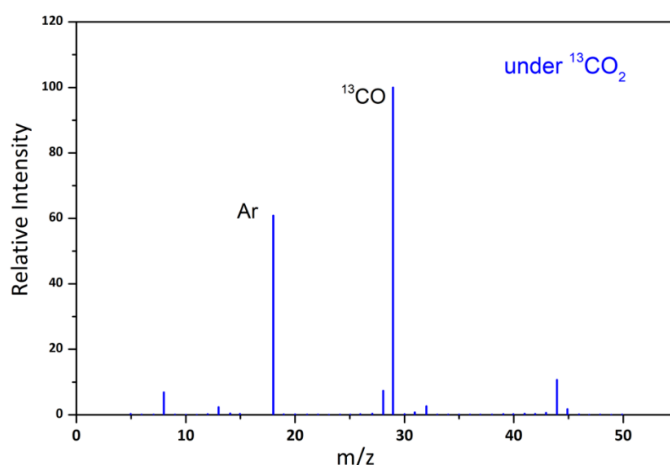


Fig. 3.23 Mass spectra of the CO GC peak corresponding to gas chromatogram obtained after long-term irradiation of a suspension containing hybrid GA-Coqpy (Coqpy 15 μ M), 0.05 M BIH and 0.1 M phenol under ¹³CO₂ atmosphere.

After saturating the solution with argon, the isotope experiment was conducted under $^{13}\text{CO}_2$ atmosphere. In addition to the argon signal, overwhelmingly dominant peak is ^{13}CO . The peak at m/z 44 in MS spectra is $^{12}\text{CO}_2$ resulting from the air entrance during a long-term irradiation. And the $^{12}\text{CO}_2$ also generated trace amount of ^{12}CO at m/z 28.

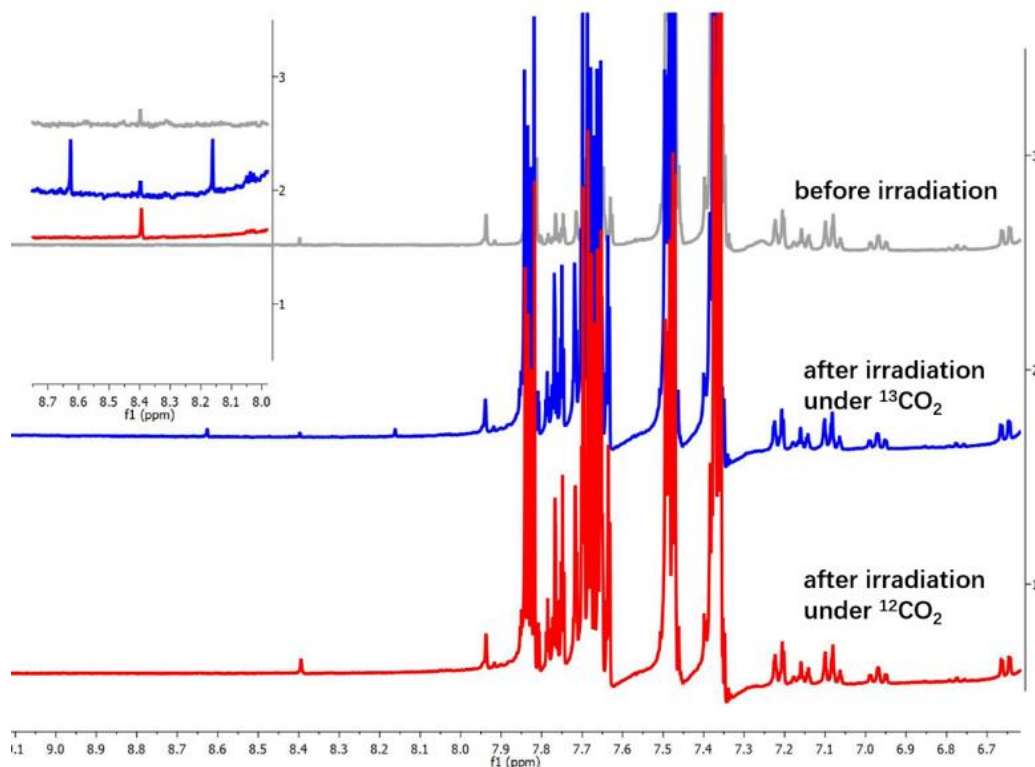
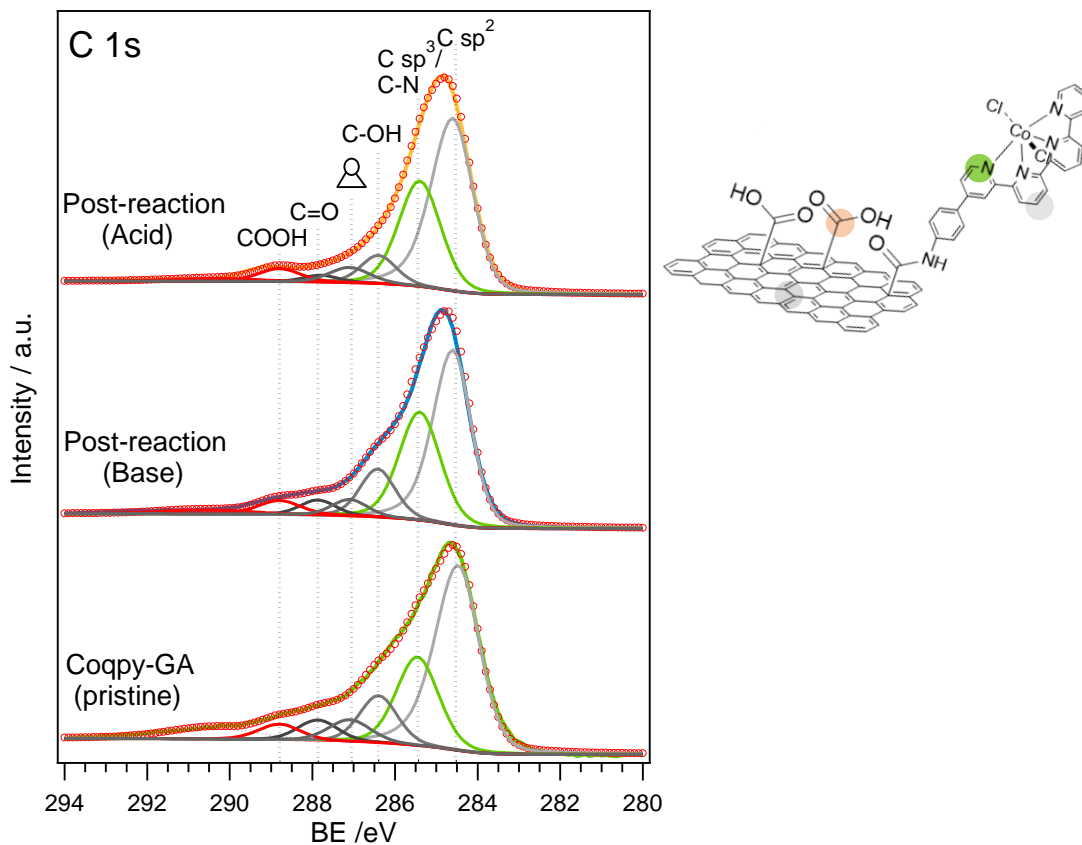


Fig. 3.24 ^1H NMR spectra of formate obtained before irradiation (grey) and after long-term irradiation of a suspension containing hybrid GA-Coqpy (Coqpy 7 μM), 0.025 M BIH and 1.51 M TEOA under $^{12}\text{CO}_2$ (red) and $^{13}\text{CO}_2$ atmosphere (blue).

A small peak of formate (*ca.* 8.4 ppm) was observed in NMR data before catalysis, which may be issued from graphitic acid surface. Visible-light irradiation were performed under $^{12}\text{CO}_2$ and $^{13}\text{CO}_2$, respectively. After photocatalysis, CO_2 was converted into formate in the presence of TEOA. Under $^{12}\text{CO}_2$, the intensity of formate peak increased; while under $^{13}\text{CO}_2$, the intensity of original peak at 8.4 ppm didn't change, but two symmetrical peaks (*ca.* 8.15 ppm, 8.65 ppm) were obtained, indicative of $\text{H}^{13}\text{COO}^-$. Formate is then generated through the CO_2 reduction under visible-light irradiation.

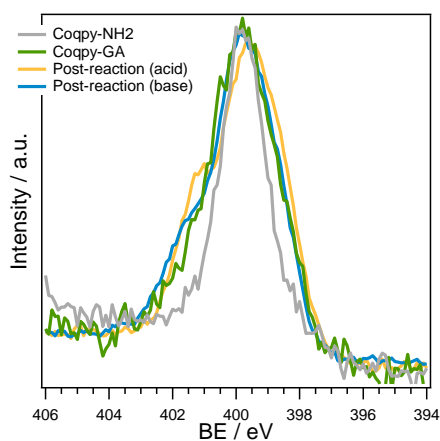
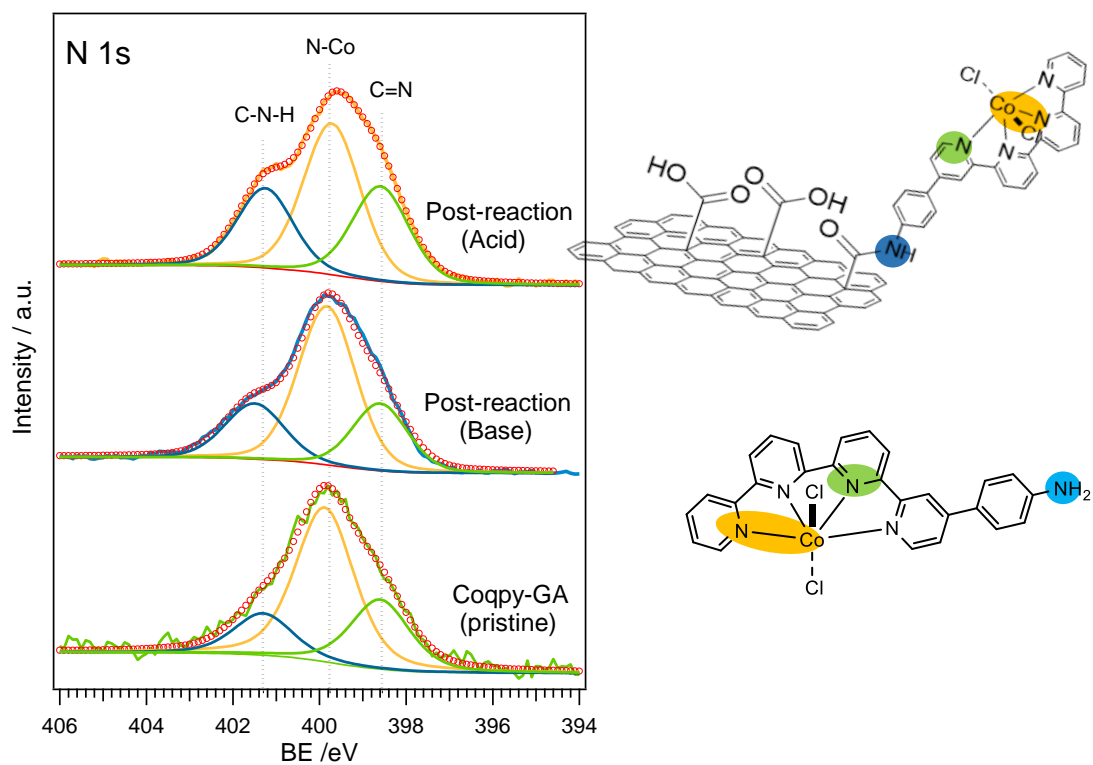
3.2.4 Stability of the catalytic system

a. XPS analysis



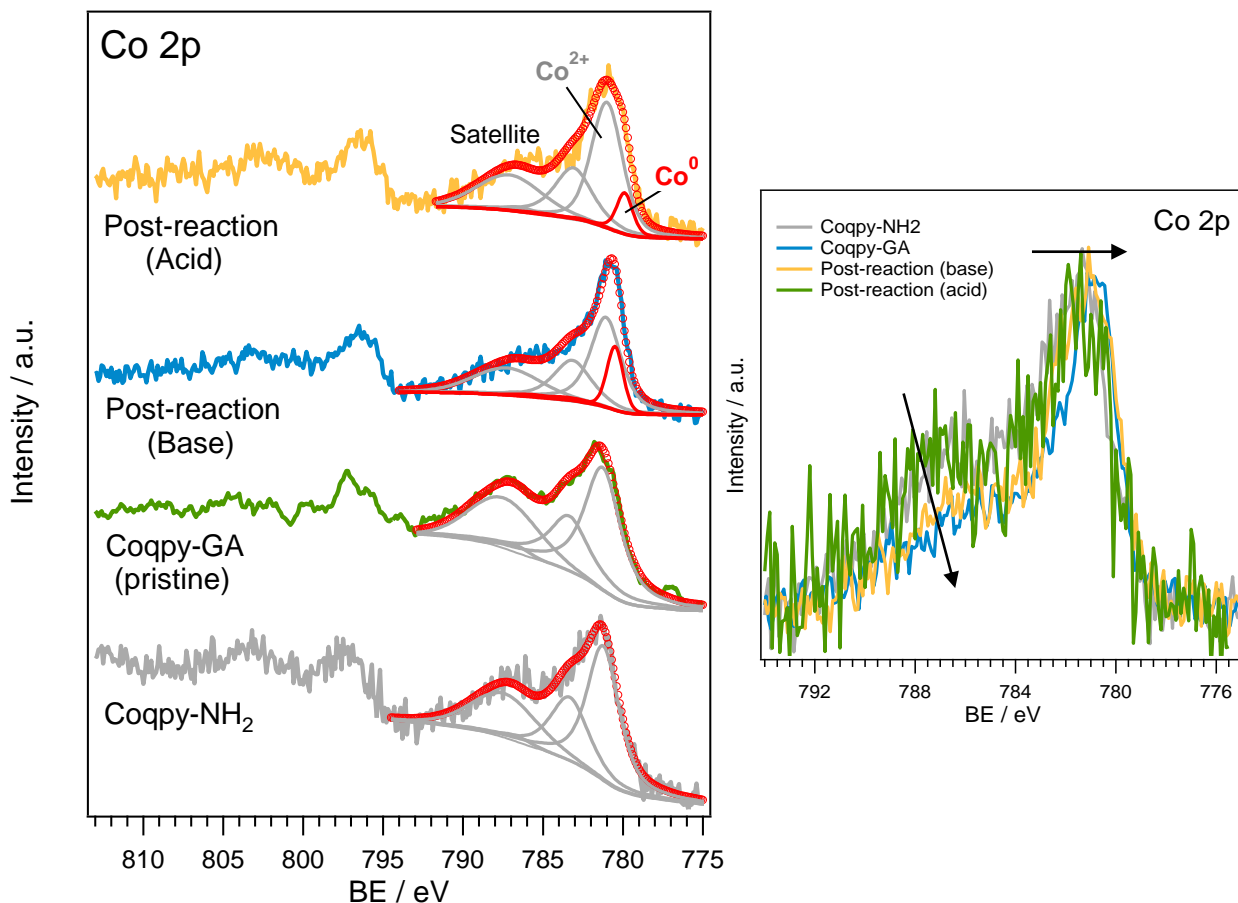
Sample	C sp ²	C sp ³ /C-N	C-OH	Epoxy	C=O	COOH
Coqpy-NH ₂	284.7 eV 57.5 %	285.6 eV 25.3 %	286.5 eV 15.5 %	---	28.8 eV 1.7 %	---
Coqpy-GA	284.4 eV 53.0 %	285.4 eV 22.2 %	286.4 eV 10.5 %	287.1 eV 5.4 %	287.9 eV 4.9 %	288.8 eV 3.9 %
Post-cat base	284.6 eV 48.0 %	285.4 eV 29.5 %	286.4 eV 11.2 %	287.1 eV 3.8 %	287.9 eV 3.5 %	288.8 eV 4.0 %
Post-cat acid	284.6 eV 53.4 %	285.4 eV 30.1 %	286.4 eV 6.7 %	287.1 eV 4.2 %	287.9 eV 1.6 %	288.8 eV 4.0 %

Fig. 3.25 XPS spectra of C for pristine GA-Coqpy and samples collected after photocatalytic reaction.



Sample	C=N	N-Co	C-NH ₂	(C) ₂ -NH
Coqpy-NH ₂	398.6 eV 18.3 %	399.7 eV 68.0 %	400.5 eV 13.7 %	---
Coqpy-GA	398.6 eV 26.2 %	399.8 eV 58.1 %	---	401.2 eV 15.7 %
Post-cat Base	398.6 eV 23,2 %	399.8 eV 56.4 %	---	401.5 eV 20.4 %
Post-cat acid	398.6 eV 29.6 %	399,7 eV 46.4 %	---	401.3 eV 24.0 %

Fig. 3.26 XPS spectra of N for pristine GA-Coqpy and samples collected after photocatalytic reaction.



Sample	Co ²⁺	Co (unknown)
Coqpy-NH ₂	100 %	---
Coqpy-GA	100 %	---
Post-cat (Base)	84.7%	15.3 %
Post-cat (Acid)	90.8 %	9.2 %

Fig. 3.27 XPS spectra of Co for pristine GA-Coqpy and samples collected after photocatalytic reaction.

Slight increase of C sp³ component was observed and was probably due to contamination from the electrolyte. The Co 2p spectra before and after coupling with GA are very similar, indicating that the Coqpy structure is maintained in the hybrid. The decrease of the satellite peak intensity, as well as the narrowing and shift toward lower BE of the main peak, may indicate a slight reduction of Co²⁺ after reaction. This effect is more evident for the reaction conducted in basic conditions.

An additional component of cobalt at lower binding energy is observed after reaction. However, it is difficult to identify from XPS.

b. Recycling experiments

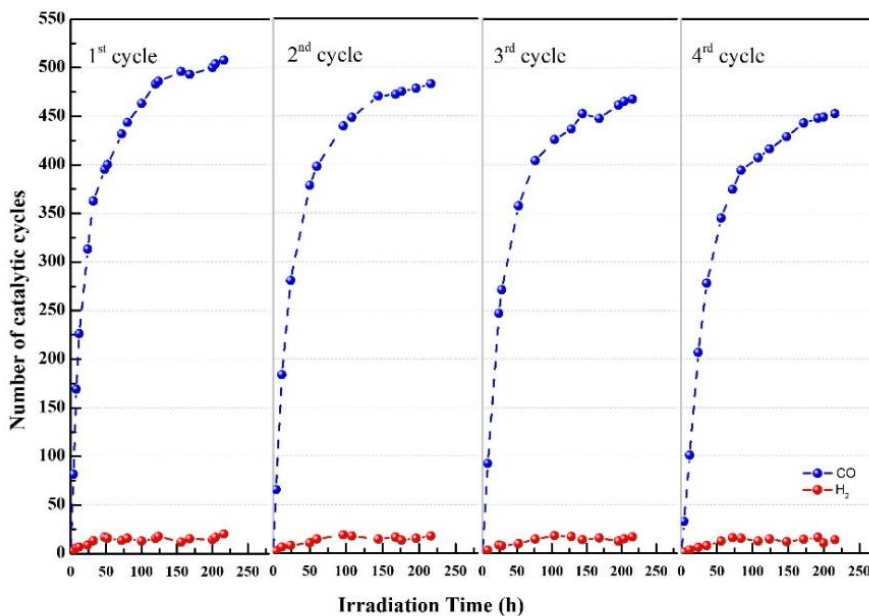


Fig. 3.28. Recycling experiments of photocatalytic reduction to CO: generation of CO (blue circles) and H₂ (red circles) during four consecutive 216 h irradiation cycles using the same hybrid material.

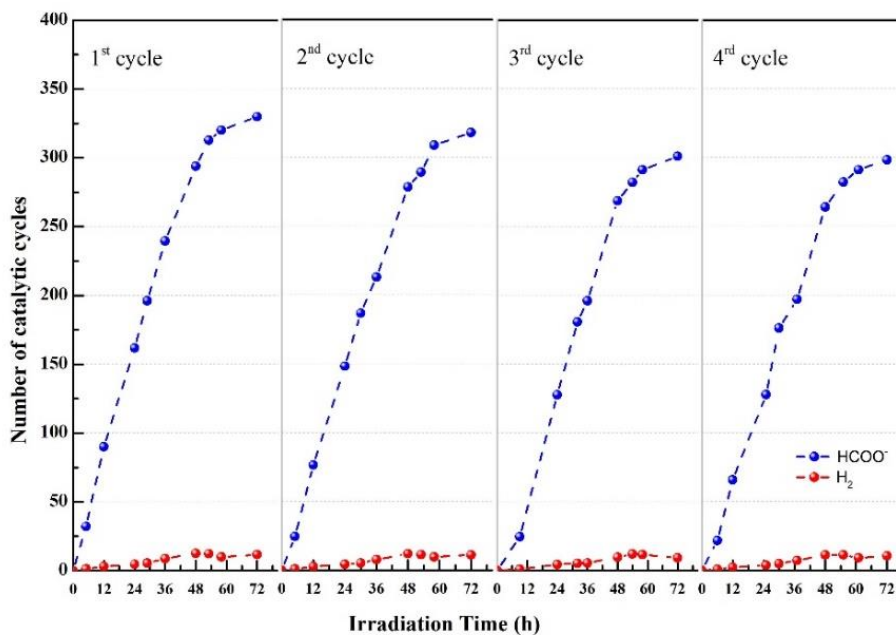


Fig. 3.29 Recycling experiments of photocatalytic reduction to formate: generation of formate (blue circles) and H₂ (red circles) during four consecutive 72 h irradiation cycles using the same hybrid material.

To further investigate the stability of the hybrid assembly, we re-employed the same hybrid for four successive cycles. Each cycle corresponded to visible-light irradiation of a standard GA@Coqpy/BIH/PhOH or GA@Coqpy/BIH/TEOA ACN solution. After each cycle, the hybrid was washed with ACN, sonicated and then centrifuged. After drying, the hybrid was dispersed again into a fresh ACN containing BIH/PhOH or BIH/TEOA and then saturated with CO₂ for 30 min prior to start a new photocatalytic cycle.

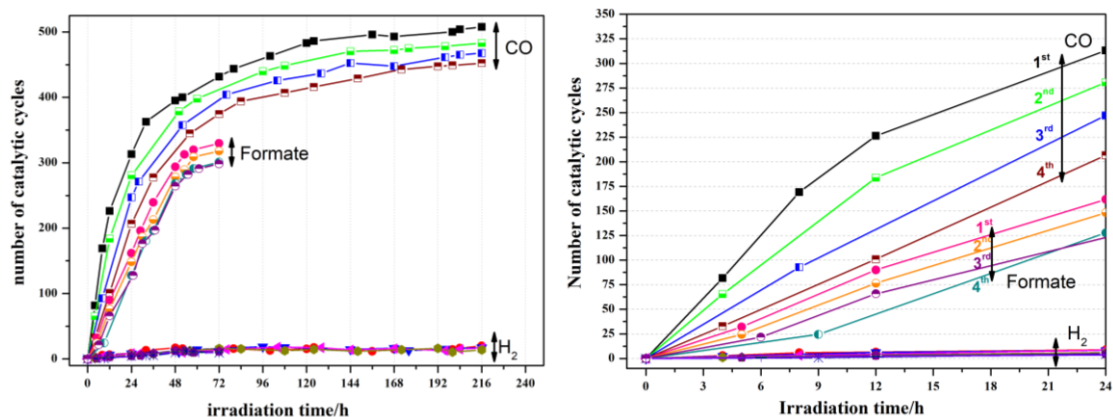
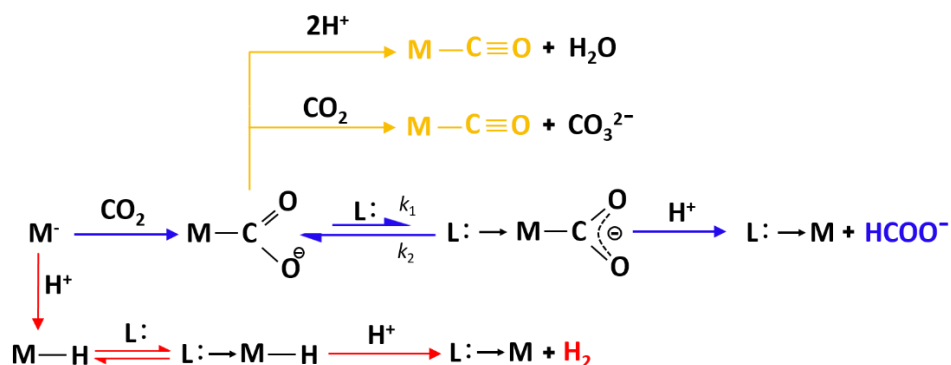


Fig. 3.30 Comparison of formate and CO generation during four cycles.

From recycling experiments with PhOH and TEOA (Fig. 3.28 and Fig. 3.29) respectively, both the production of CO and formate remain important but have declined, which may be due to the shedding or decomposition of the Coqpy molecule and the environmental changes of the functional groups on the GA surface. It is worth mentioning that during the recycling experiments under the two conditions, the selectivities of CO and formate remained unchanged. The overlapping data illustrate that CO formation is faster than HCOO⁻ (Fig. 3.30).

3.2.5 Proposed pathway for CO and formate production

A possible catalytic pathway accounting for the above experimental results is given in the following scheme:



Scheme 3.3 Proposed pathway of H₂ (red), CO (yellow), formate (blue) generation. L represents TEOA, that may bind to the Co center and increase the electronic density at the C atom of the CO₂.

H₂ may be generated through a metal hydride intermediate, after reaction of a proton with the doubly reduced catalyst (red pathway on Scheme 3.3). It remains a minor pathway, as illustrated in Tables 3.7 and 3.8. The formation of an adduct between CO₂ and the reduced catalyst is preferred, and C-O bond cleavage ensues either with a weak Brønsted acid (*e.g.* phenol) or with a second CO₂ molecule (Lewis acid) in absence of any added Brønsted acid, releasing CO in both cases (yellow pathway, Scheme 3.3). Note that the pending free carboxylic acid groups remaining at the surface of the graphene material may also act as a proton donor, even if the concentration is very small. In the presence of triethanolamine (TEOA = L, Scheme 3.3), an equilibrium occurs with M-CO₂ adduct, with L acting as an axial ligand to the metal (it is reasonable to postulate that k_1 and k_2 are large with $k_1 \ll k_2$, so that the equilibrium constant $K = k_1/k_2$ is small). It significantly increases electron density at the carbon atom of the partially reduced CO₂.¹³² In the presence of a low content of acid (residual acid groups at the graphene surface, see *e.g.* entries 2-5, Table 3.8) or of a very weak acid (*e.g.* entry 4 in Table 3.9), protonation may occur at the C atom, leading to the release of formate (blue pathway, Scheme 3.3). In such cases, the equilibrium between M-CO₂ and L-M-CO₂ is shifted to the right and formate is obtained as only product (entries 2-5, Table 3.8) or in competition with H₂ production once a weak external acid is added to the solution, due to the concomitant enhancement of the hydricity of the M-H hydride intermediate (entries 4-6, Table 3.9), as illustrated on the red pathway in Scheme 3.3.

3.3 Conclusions and perspectives

The Coqpy@mpg-C₃N₄ hybrid material we synthesized is the first catalytic system made of a molecular catalyst covalently immobilized on carbon nitride for CO₂RR. The effective covalent connection of molecular catalysts to polymeric materials seems to be a promising method for catalytic reduction of CO₂, leading to good control of the structure of the catalytic site, high selectivity and activity.

After combing earth-abundant metal-based catalysts with carbon nitride-based materials, Coqpy@mpg-C₃N₄ hybrid not only shows high selectivity and CO production activity, but also shows long-term stability. It combines the high selectivity of molecular catalysts and the excellent stability of solid materials.

Coqpy and the surface-functionalized graphene material may also be connected by covalent bonds to achieve efficient electron transfer. This hybrid can efficiently and selectively achieve the photochemical reduction of CO₂ and still maintain stable catalysis after recycling. The target product of CO₂ reduction can in this case be switched by changing the reactants. These results demonstrate the promising interaction between inorganic materials and molecular catalysts towards new catalytic activity.

Such covalent combinations are also based on independent adjustment of the molecular complex structure and inorganic material structure, and there is still a lot of room for improvement in the combination between the two parts. The good catalytic performances so far obtained open new pathways for the development of highly active catalytic materials, and not only for the reduction of CO₂. Other catalytic reactions may be envisioned, such as OER, ORR and reduction of N₂. On a more fundamental side, a better understanding of charge transport and transfer properties within the hybrid materials still needs to be achieved.

Chapter 4 - New approach towards strong conjugation of molecular catalysts with (semi)conductive support

4.1 Electrochemical reduction of CO₂ through strong electronic coupling of Coqpy to graphitic electrode

In our previous work, we studied molecular catalysts supported by inorganic materials, showing that the covalent bond-linked hybrids catalysts have high catalytic efficiency and excellent selectivity. To achieve efficient electron transfer between the light sensitive material and the catalytic sites, we need to have electronic interaction between the molecular orbitals of the catalyst and the conduction band of the semi-conductor. Modulation and control of this interaction may be a way to study more thoroughly the impact of this factor and then to design even more efficient catalytic systems. Naturally, we began to seek other ways to combine the Coqpy molecule with solid material. For that, we choose glassy carbon electrode surfaces. This chapter accounts for the preliminary work we have so far done along these lines. It is a short one but since it may open original perspectives for my thesis topics, thus I decided to include it in this manuscript.

In this connection, we became interested in the original and stimulating work of Surendranath's group. They have done a series of interesting work based on graphite-conjugated pyrazines. They managed to introduce ortho-quinone moieties at edge planes of graphitic carbon which were reacted with ortho-phenylenediamine derivatives (o-phenylenediamine, [Ru^{II}(dmbpy)₂(phenda)]²⁺ (dmbpy = 4,4'-dimethyl-2,2'-bipyridine, phenda = 5,6-diamino-1,10-phenanthroline) and [Rh^{III}Cp*(phenda)Cl]⁺ (Cp* = pentamethylcyclopentadienyl), respectively, see Fig. 4.1). It led to graphite-conjugated pyrazines (GCPs) that are active for oxygen reduction electrocatalysis in alkaline aqueous electrolyte.¹³³

Cyclic voltammetry tests illustrate that in protic electrolytes, both surface-bounded GCC-phenazine units and dissolved molecular phenazine undergo chemically reversible

PCET reactions. The metal-based GCC sites can give rise to redox waves only if they can undergo ion exchange with the solution.

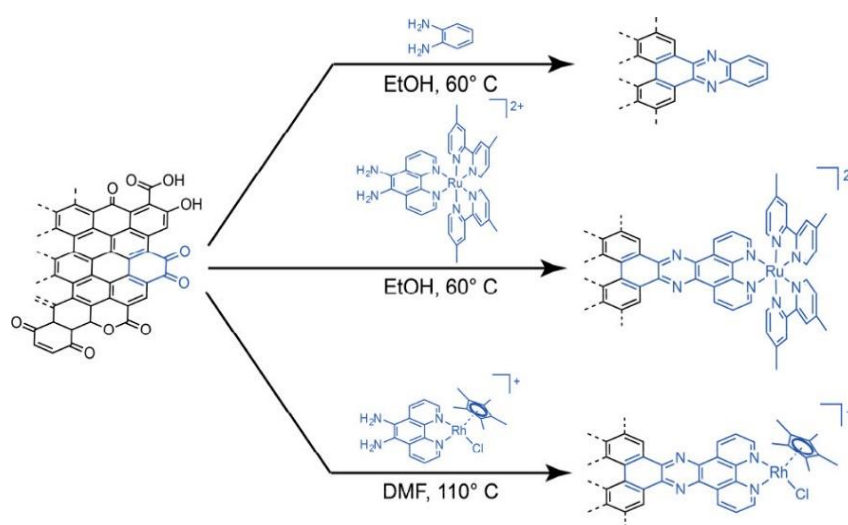


Fig. 4.1 Synthesis of GCC-Phenazine (Top), GCC-Ru (Middle), and GCC-Rh (Bottom). Adapted with permission from ref. 133, Copyright 2018 American Chemical Society.

Without ion transfer, no redox signal is observed. The absence of redox features in GCC-phenazine and GCC-Ru in aprotic acetonitrile electrolyte is most likely because no ET is occurring. For GCC-Ru, no redox wave was observed despite scanning > 0.35 V positive of the expected value, too large of a shift to be explained by changes in the π acidity of the surface-conjugated phenanthroline ligand. It follows that if no reversible redox wave is observed even 0.35 V past the expected E° , the variation in applied potential is not imposing a substantial driving force for ET to the Ru center. The fundamental reason why no Ru reduction is obtained is due to the very strong electronic conjugation of its orbitals with the conduction band of the electrode: upon going to negative potential, the Fermi level energy of the electrode increases and so does the orbitals of the conjugated Ru center. In other words, modifying the potential at the electrode does not modify the driving force for electron transfer between the carbon surface and the metal sites (*i.e.* the outer sphere charge transfer does not occur). It is the change of the electrostatic surface potential that drive ion transfer and trigger concerted charge transfer, then allowing to activate substrates in catalytic processes.

This simple “bottom-up” method for constructing molecularly well-defined active sites on ubiquitous graphitic solids enables the rational design of tunable heterogeneous catalysts.

The same group recently reported the condensation of *fac*-Re(5,6-diamino-1,10-phenanthroline)(CO)₃Cl to *o*-quinone edge defects on graphitic carbon surfaces, leading to a graphite-conjugated rhenium (GCC-Re) catalysts that is highly active for CO₂ reduction to CO in acetonitrile electrolyte.⁶⁹ In this work, the well-defined and tunable electrocatalysts were again obtained on graphitic carbon surfaces, an additional illustration of this promising strategy for constructing heterogeneous catalysts.

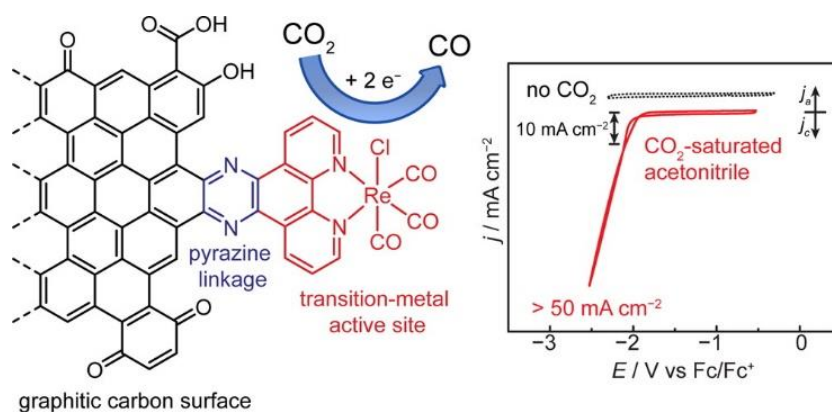
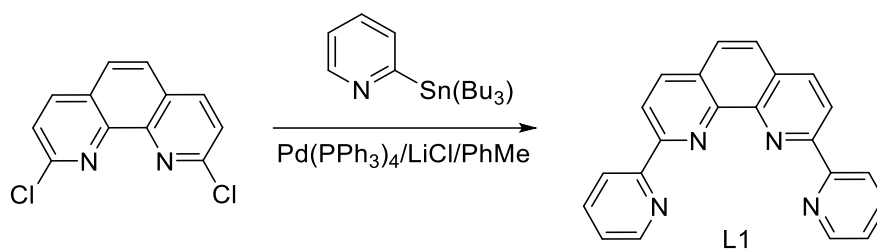


Fig. 4.2 Graphite-conjugated rhenium catalysts for CO₂ reduction. Adapted with permission from ref. 69, Copyright 2016 American Chemical Society.

Following these early studies, we used an earth-abundant metal cobalt, that is, to conjugate the catalytically active complex Coqpy with glassy carbon electrode (GCE) and started studying its electrochemical behavior and catalytic performance.

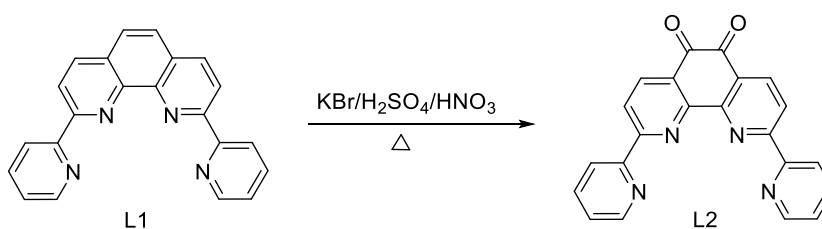
4.1.1 Synthesis of CoLCl₂ (L = 2,9-di(pyridin-2-yl)-1,10-phenanthroline-5,6-diamine)

a. Synthesis of 2,9-di(pyridin-2-yl)-1,10-phenanthroline (L1)¹³⁴



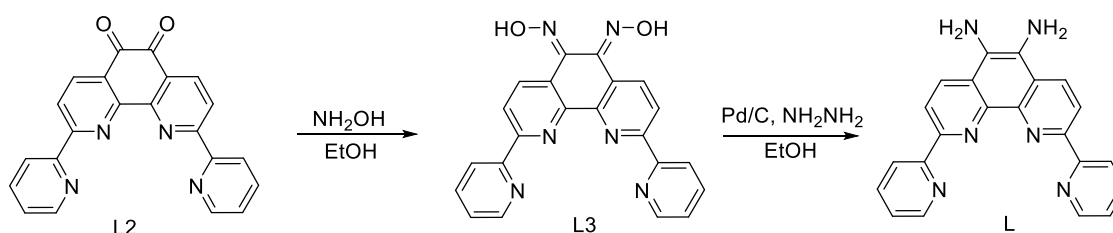
A mixture of 2,9-dichloro-1,10-phenanthroline (1.25 g, 5.0 mmol), 2-(tributylstannyl)pyridine (4.66 g, 12 mmol), Pd(PPh₃)₄ (577.5 mg, 0.5 mmol) and LiCl (737.6mg, 17 mmol) in toluene (50 mL) was refluxed for 48 h under argon. After cooling down, the mixture was filtered and evaporated to dry. The crude product was purified by chromatography with petroleum/dichloromethane (1:1) as elute to afford 2,9-di(pyridin-2-yl)-1,10-phenanthroline as white powder. Yield: 750 mg (44%).

b. Synthesis of 2,9-di(pyridin-2-yl)-1,10-phenanthroline-5,6-dione (L2)



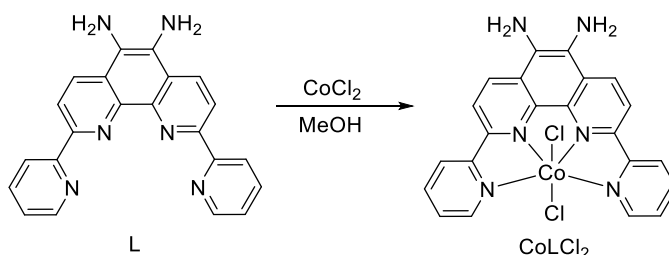
A mixture of 2,9-di(pyridin-2-yl)-1,10-phenanthroline (361 mg, 1.08 mmol), potassium bromide (1.30 g, 10.9 mmol) in H₂SO₄ (4.5 mL)/HNO₃ (2.5 mL) was stirred for 12 h at 85 °C. After cooling down, the mixture was poured on ice and neutralized with saturated NaHCO₃. The yellow 2,9-di(pyridin-2-yl)-1,10-phenanthroline-5,6-dione was filtered and washed with water. After drying under vacuum for 12h, 2,9-di(pyridin-2-yl)-1,10-phenanthroline-5,6-dione was obtained as a yellow solid. Yield: 350 mg (96%).

c. Synthesis of 2,9-di(pyridin-2-yl)-1,10-phenanthroline-5,6-diamine (L)



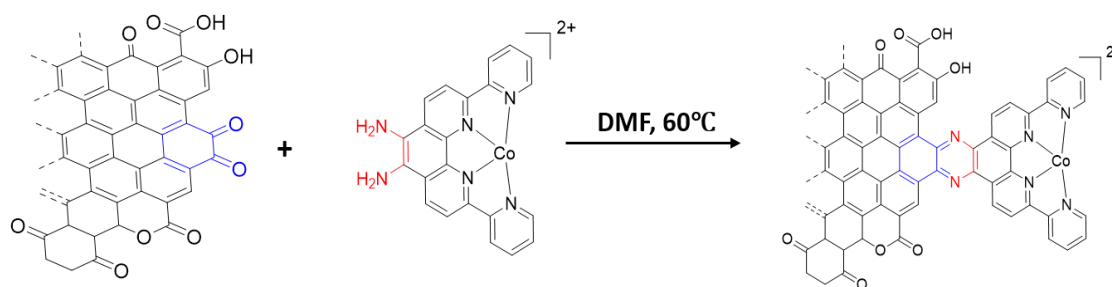
A mixture of 2,9-di(pyridin-2-yl)-1,10-phenanthroline-5,6-dione (350 mg, 0.96 mmol), NaHCO₃ (152 mg, 1.43 mmol) and NH₂OH·HCl (240 mg, 3.46 mol) in ethanol (20 mL) was refluxed for 14 h under argon. After cooling down, the solid was filtered and washed successively with water and ethanol. The resulting yellow product (300 mg) and Pd/C (100 mg, 10% on activated carbon) in ethanol (20 mL) was heated to reflux under argon. Then hydrazine monohydrate (2.5 mL) in ethanol (5 mL) was added dropwise over 1 h. The resulting reaction mixture was further refluxed overnight under argon. After cooling down, the solvent was evaporated in vacuo. Then the resulting solid was dissolved in methanol, followed by filtering through a bed of celite to remove the undissolved Pd/C catalyst. The solvent was evaporated in vacuo and the resulting solid was washed with water and isopropanol to afford 2,9-di(pyridin-2-yl)-1,10-phenanthroline-5,6-diamine as a red solid. Yield: 200 mg (57%). ESI-MS in MeOH: m/z 365.5, [L + H]⁺.

d. Synthesis of CoLCl₂



A mixture of 2,9-di(pyridin-2-yl)-1,10-phenanthroline-5,6-diamine (36.4 mg, 0.1 mmol) and CoCl₂·6H₂O (36 mg, 0.15 mmol) in MeOH (30 mL) was stirred at room temperature for 24 h under argon. The brown precipitate was filtered and washed with water/isopropanol to give CoLCl₂ as a brown yellow solid. Yield: 30 mg (61 %). ESI-MS in MeOH: m/z 211.5, [CoL]²⁺; m/z 423.5, [CoL]⁺; 458.4, [CoLCl]⁺.

4.1.2 Synthesis of graphite-conjugated-Coqpy (GC-Coqpy)



Scheme 4.1 Preparation scheme for conjugating glassy carbon and Cobalt-complex.

The synthesis of GC-Coqpy was achieved by condensing ortho-quinone of a GCE electrode with ortho-phenylenediamine of the modified molecular catalyst. After polishing the electrode surface, the GC-electrode suffered a brief anodic treatment to creating the surface quinone. Specifically, anodizing the electrode via potentiostatic electrolysis at 3.5 V vs. RHE for 10 seconds in 0.1 M H₂SO₄. Then the electrode was abundantly rinsed with water and ethanol.

After that, the GCE was immersed in 20 mL of Ar sparged DMF containing 0.1 mM of the desired ortho-phenylenediamine derivative. The reaction vessel was subsequently heated under Ar for 24 hours at 60°C. Upon cooling, the electrode was copiously washed with ethanol and subsequently treated with 0.1 M HClO₄ for 3 hours to hydrolyze adventitious imine linkages formed on the surface. Following the acid treatment, the electrode was washed with pure water.

An additional procedure is necessary for removing organic physisorbed species. The electrode was then soaked into ACN for 3h to remove organic physisorbed species. Next, after rinsing the electrode with water and soaked in water for an additional hour, the obtained electrode was dried in a 50 °C oven.

4.1.3 Characterization of GC-Coqpy electrode

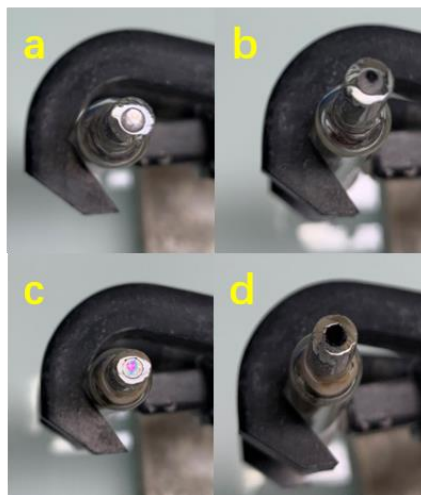


Fig. 4.3 Pictures of synthesized GCC-Coqpy-I from different perspectives. (a), (b) obtained by using Pt gauze as a counter electrode; (c), (d) obtained by using Pt wire as a counter electrode.

The pictures illustrate the unevenness of the electrode surface, which is most likely caused by the uncontrolled oxidation during the first oxidation step. Using Pt wire or Pt net as counter electrodes result in different surface conditions (Fig. 4.3).

We further tried to oxidize the electrode surface differently. After polishing the glassy carbon electrode, using the platinum wire as the counter electrode, the electrolytic solution was oxidized under stirring in time sequences of 5 seconds. A uniform oxidation surface can be obtained in 25 to 30 seconds. After condensation with molecular catalyst, the electrode surface is smooth and shiny. Moreover, it is still smooth after cyclic voltammetry, without visible changes from simple naked eye (Fig. 4.4). We set the oxidation time until the surface is uniform.

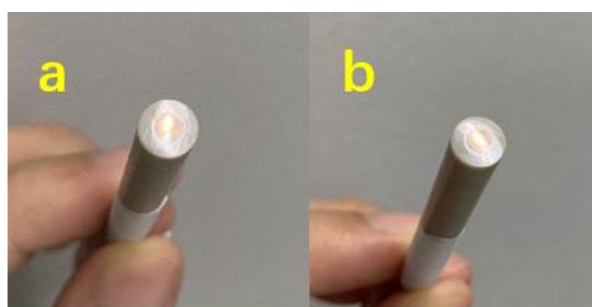


Fig. 4.4 Pictures of GCC-Coqpy-II obtained from modified procedure (a) as-synthesized; (b) after CV scan.

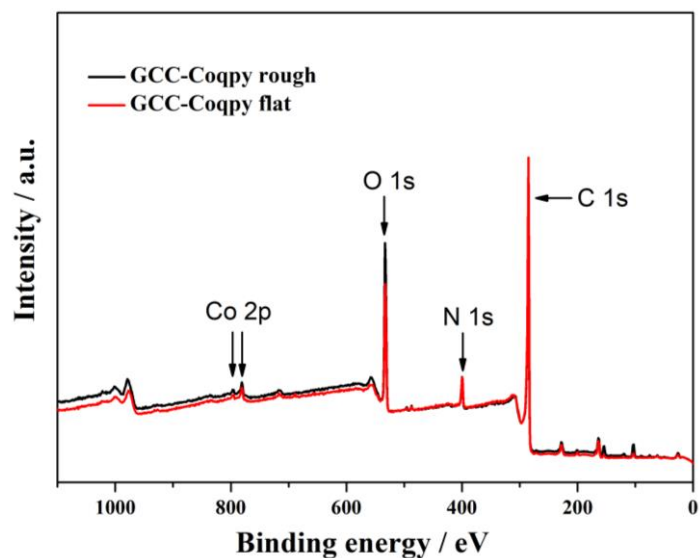


Fig. 4.5 XPS survey spectra of two regions in GCC-Coqpy on GCP (glassy carbon plate).

From XPS survey of GCC-Coqpy, it can be concluded that the Co:N ratio is approximately 1:6 (Fig. 4.5; theoretical ratio is 1:6). In high resolution XPS, $N_{\text{pyridine}}:N_{\text{pyrazine}}$ of GCC-Ru is 1.5:1 (Fig. 4.6; theoretical ratio is 2:1). The above XPS analysis is thus consistent with the expected condensation structures.

Only preliminary experiments have been conducted so far to study the catalytic performance of GCC-Coqpy and their electrochemical properties. A brief account is described in the next section.

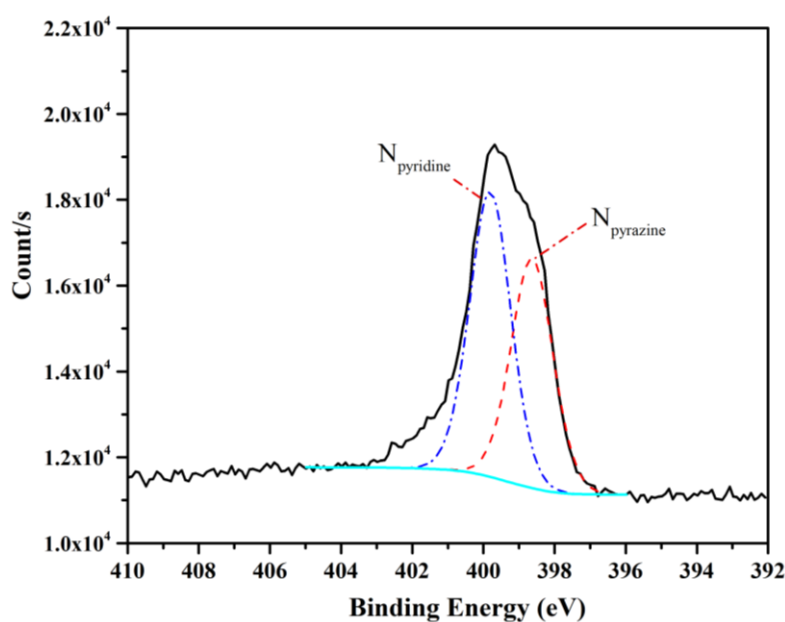


Fig. 4.6 High-resolution N 1s XPS spectra of GCC-Coqpy on GCP (glassy carbon plate).

4.1.4 Cyclic voltammetry characterization of GCC-Coqpy electrode

Typical cyclic voltammetry of a GCC-Coqpy-I under Ar and CO₂ is shown in Fig. 4.7. Under the CO₂ atmosphere, the onset potential is around -1.1 V vs. SCE. However, the same phenomenon was not observed in the GCC-Coqpy-II catalyst (Fig. 4.8). There is no significant difference between carbon dioxide and argon. After adding 3 M of phenol, an irreversible reduction peak appeared at -1.2 V. After bubbling with Ar, the peak at -1.2 V disappeared. It thus seems that these electrodes are catalytically active and show early onset potential. Detailed catalytic studies will be the next step of this work.

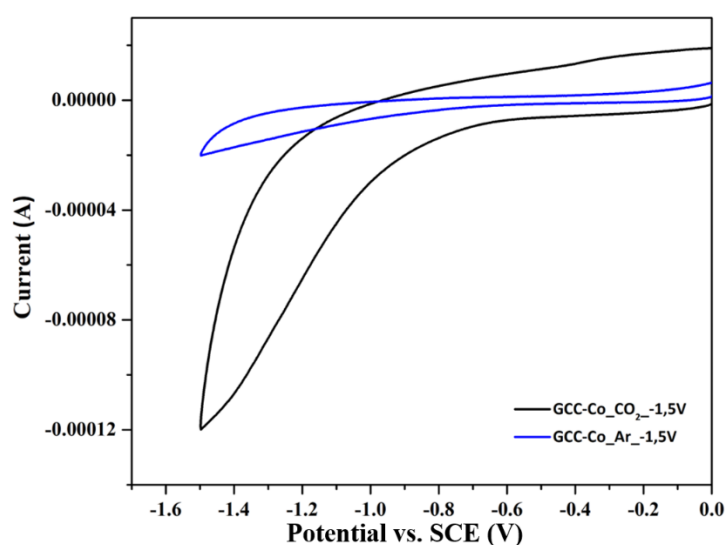


Fig. 4.7 CV comparison of GCC-Coqpy-I under CO₂ and Ar in ACN with 0.1 M TBAPF₆. $v = 0.1$ V/s.

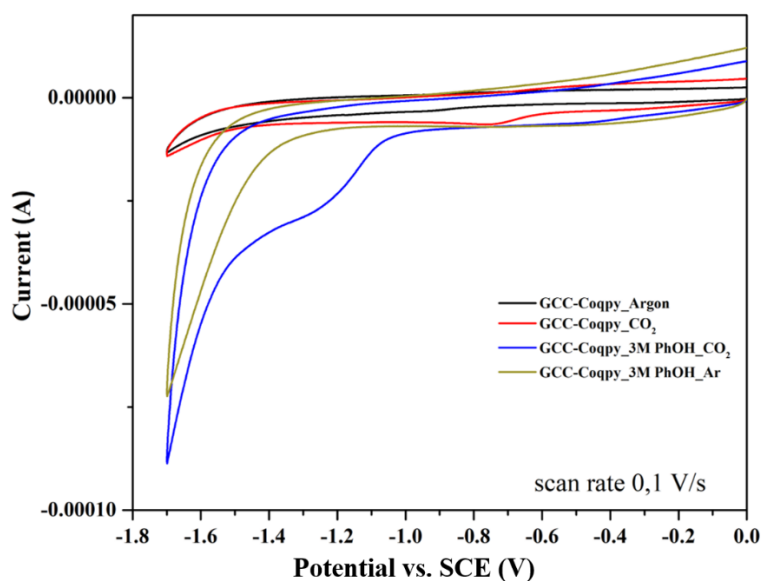


Fig. 4.8 The CV of GCC-Coqpy-II in ACN with 0.1 M TBAPF₆ and 3 M PhOH. $v = 0.1$ V/s.

4.2 Perspectives

The preliminary cyclic voltammetry data have sparked our interest in having a thorough look at these modified electrodes. Preliminary data are promising both in organic solvent and protic medium (not shown in this manuscript). The synthesis of conjugated systems has also been proven to be successful and it may be widely applied to many molecular catalysts. One may also envision to use different types of materials (both conductive and semi-conductive, 2D and 3D materials). Thus, further studies will help in characterizing the catalysis and getting insights into the catalytic mechanisms. This may lead to extremely stable catalytic systems, and maybe to new catalytic properties.

Chapter 5 - General conclusions and perspectives

5.1 General conclusions

The main objective of this thesis was to explore the use of molecular catalysts into artificial photosynthetic systems working under visible-light illumination, and to integrate these catalysts into hybrid systems upon combining them to a conductive or semi-conductive material. The molecular catalysts are capable of triggering catalytic reactions in homogeneous solutions or upon hybridization with other supporting matrices to drive catalysis in heterogeneous conditions. The presented results describe the molecular photocatalytic reduction conducted with a bimetallic cobalt complex bearing a bi-quaterpyridine ligand in several different conditions, including various photosensitizers (Ru complex, organic dye, semi-conductive C₃N₄ polymer), in the presence of additional co-substrates (weak acid-phenol, base-TEOA). Further, light-harvesting semiconductor mpg-C₃N₄ and graphene acid were chosen to append with the monomeric quaterpyridine cobalt catalyst. Both the catalytic efficiency and the selectivity as well as direction towards the product showed a significant improvement compared with the freely diffusing complex. These results could be summarized as follows:

1. We have first studied photo-stimulated catalytic reduction of CO₂ in homogeneous solutions with binuclear cobalt complex bearing a bi-quaterpyridine ligand. Various photosensitizers, including Ru complex, organic compound, and semiconductive carbon nitride, can sensitize the bimetallic biqpyCo₂ and furnish reduction products through two electrons/two protons transfers. The catalyst can achieve selective CO₂ to CO or HCOO⁻ conversion upon visible light irradiation. Remarkably, by changing the acid co-substrate present in the solution, the two synergistic cobalt atoms can steer the reactivity towards the desired product. Selective formate production was obtained in basic ACN solution with TEOA. The most selective formation of formate was sensitized by g-C₃N₄, which produced 91% formate (TON *ca.* 493) and 9% H₂ (TON *ca.* 48). Meanwhile, formate can

be generated more efficient with the $[\text{Ru}(\text{phen})_3]^{2+}$, corresponding to a turnover number of 821 (selectivity 75.9%). At the same time, 20.4% of CO can be obtained. By employing a phenoxazine derivative (pheno) as photosensitizer, CO_2 was can be converted to formate and CO with turnover numbers of 565 (selectivity 58%) and 284 (selectivity 29%), respectively. While CO_2 reduction affords CO with almost perfect selectivity in the presence of a weak acid, phenol for example. Sensitized by $[\text{Ru}(\text{phen})_3]^{2+}$, CO_2 was converted to CO and formate in a turnover number of 829 (selectivity 96%) and 12, respectively. Organic compound pheno can also be used as photosensitizer, resulting a turnover number of 518 for CO in a selectivity of 89.3% with a trice amount of H_2 produced. Through investigation conducted with cyclic voltammetry, infrared spectro-electrochemistry and DFT calculation, we have demonstrated that such control of 2 electrons/2 protons reduction of CO_2 results from cooperativity between the 2 cobalt sites. It is one of the first time that such cooperativity is demonstrated in molecular multi-metallic catalysts. It opens stimulating perspectives for the activation of CO_2 . Upon tuning the nature of the two metals: enhanced reactivity may be obtained. Upon tuning the linker between the two sub-units chelating the two metals, possible coordination of several molecules (CO_2 , CO) could lead to new reactivity and C-C coupling.

2. By creating covalent amide bonds, solid-supported Coqpy photocatalytic systems have been designed and evaluated. It includes the grafting the complex with mesoporous carbon nitride or graphene acid, respectively. These cheap and relatively easily prepared materials are also excellent solid materials in the design of artificial photosynthetic systems.

Grafting Coqpy with mpg- C_3N_4 through an amide bond led to constructs a molecule supported photocatalyst for photoreduction of CO_2 . Using BIH as sacrificial donor, CO was selectively generated with a TON of 128 (selectivity 98%) in ACN solution containing phenol, showing an enhanced catalytic activity compared with samples obtained by physical mixing or absorption, along with excellent stability over time. Results of photocurrent response, electrochemical impedance spectroscopy and

fluorescence emission quenching illustrated that fast and efficient electron transport occurred from the excited material to the catalyst.

3. Functionalizing carboxyl groups at the surface of graphene provided another option to graft the amino-modified Coqpy. In that case, the obtained Coqpy@GA can convert CO₂ to CO with a high selectivity of 97% (TON *ca.* 513) in the presence of phenol. When replacing phenol with TEOA, CO₂ can be reduced to formate in a turnover number of 330 and 99% selectivity. This may be related to specific coordination properties at the Co metal immobilized at the surface material. Interestingly, this phenomenon bears similarity to what we have observed in homogeneous photocatalysis with bimetallic complex. After comparing with other experimental results, a possible scheme of H₂, CO, formate formation was proposed to illustrate the different pathways, especially for CO and formate.

4. Conjugating molecular complexes with conductive materials have been proved to be beneficial for electron transfer during catalytic reaction. A preliminary study has been conducted including the preparation of Coqpy conjugated glassy carbon electrode and cyclic voltammtery test, showing catalytic activity with an early onset potential.

All these catalysts that have been investigated in my thesis illustrate the promising efforts for mimicking artificial photosynthesis. The synthesized bimetallic molecular complex biqpyCo₂ shows the significance of cooperation between two metal centers. Moreover, the proposed catalytic mechanism with a molecular catalyst plays a vital role in achieving better catalytic performance. On the other hand, molecule-supported catalytic systems make efforts to improve the stability and reutilization of the catalysts, which is beneficial to the development of molecular catalysts in practical application. Even these above investigations work on different aspects of artificial photosynthesis, they all provide useful inspiration for further study.

5.2 Future perspectives

As a perspective, promising molecular catalysts with high intrinsic still need to be discovered for producing chemical fuels from solar energy *via* AP. Tuning the structure of molecular catalysts after getting insights spectroscopic and mechanistic studies is a rational approach towards intrinsic catalytic performance. For an AP device based on molecular catalysis, a high intrinsic activity of the molecular catalyst, especially low overpotential, is an essential requirement for obtaining high efficiency. In this connection, bimetallic or multimetallic complexes may show excellent activities and to mimicking the natural photosynthetic process and as noted above may lead to new chemistry in the future.

Because of the complexity of molecule-supported AP catalytic systems, the performance can be controlled by several factors. The present research is only a preliminary contribution toward a practical device. Such device for solar fuels production is highly challenging involving not only light absorption, charge transfer, and catalytic activity aspects but also engineering problems, such as device design and mass transfer/transport control. Considering the advantages of molecular catalysts, the construction of systems based on molecular catalysts is still highly promising.

The following challenges need to be addressed for developing AP systems:

(1) To develop earth-abundant metal based efficient catalysts that are able to work under aqueous, especially acidic conditions. Moreover, the design of catalysts to go beyond the “traditional” of two-electron reduction to produce liquid fuels (or convert N_2 into chemicals) is still not achieved.

(2) To expand light absorbers, explore new transparent p-type semiconductors and upgrade the anchoring groups of functional molecules for long-term stable AP devices. The common anchoring groups of molecules are carboxylic or phosphate groups. However, such groups cannot tolerate long periods of irradiation in aqueous electrolyte environment. Stronger binding groups should be designed and investigated.

(3) To reveal the deactivation pathways, especially the reasons for the decomposition of modified catalysts. Such understanding is essential to improve the stability and activity of AP devices for practical applications.

In addition, the strategies for immobilization of molecular catalysts on the substrate, the mechanistic understanding of catalytic process, and the determination of the kinetics of electron transfer (notably at photoelectrodes) also need to be investigated thoroughly. These are also urgent tasks for the further development of AP devices based on molecular catalysts and future practical applications.

Chapter 6 - Experiments and methods

6.1 Chemicals and Synthesis

6.1.1 Commercial chemicals

Solids

NaOH (99.5%), KOH (99.5%), NaHCO₃ (99%), KCl (99.5%), KHCO₃ (99.5%), K₂C₂O₄ (99.5%) and FeCl₃·6H₂O (99.5%) were purchased from Merck; KH₂PO₄ (97%) was purchased from Prolabo; K₂HPO₄ (99.5%) was purchased from Labosi; *fac*-(Tris(2-phenylpyridine))iridium(III) (99%) was purchased from Sigma-Aldrich. FeCl₃·6H₂O (99%), FeBr₂ (99%) and phenol (99.5%) were purchased from Alfa Aesar; (2, 2'-bipyridine)bis(2-phenylpyridinato)iridium(III) hexafluorophosphate (Ir(ppy)₂(bpy)PF₆, 90%) was purchased from TCI. (NH₄)₂-Fe(SO₄)₂·6H₂O (99%), purpurin (90%), benzaldehyde (99%), N, N'-dimethyl-1, 2-phenylenediamine (99%) and 2-phenylbenzimidazole (99.5%) were purchased from Sigma Aldrich; NH₄PF₆ (99.5%) was purchased from Acros Organics; NBu₄PF₆ (99%) and Ethylenediaminetetraacetic acid disodium salt (EDTA, 99%) were purchased from Fluka; free base 5,10,15,20-tetra(N,N,N-trimethyl-4-anilinium)porphyrin tetrachloride was purchased from Frontier Scientific, Phen1 and Phen2 were obtained from Miyake lab.

All chemicals were used as received without further purification.

Liquids and solvents

Acetone (99.8%), methanol (99.8%), ethanol (99.9%), ethyl acetate (99.5%), dichloromethane (99%), 2-propanol (99.0%), and hydrochloric acid (37%) were purchased from VWR. Methyl iodide (99%) and acetic acid (99.5%) were purchased from Alfa Aesar. Electrolyte solutions were prepared with ultra-pure water (TKA MicroPure, 0.055 μS·cm⁻¹) or electrochemical grade acetonitrile, dimethyl sulfoxide, N, N-dimethylformamide (Acros, > 99.8%, over molecular sieves and stored under Argon

atmosphere). Triethylamine (TEA, Acros Organics, 99%), triethanolamine (TEOA, Sigma, >99%), N, N-diisopropylethylamine (DIPEA, Fisher Scientific, >99%) and 2, 2, 2-trifluoroethanol (TFE, Romil Ltd., >99.5%) were used without further purification. Methanol and dichloromethane were distilled over calcium hydride; THF was dried over sodium then distilled after addition of benzophenone. Solvents were freshly distilled or stored overnight under an argon atmosphere.

Gases

Argon (> 99.998 %), ^{12}CO (> 99.7 %), and $^{12}\text{CO}_2$ (> 99.7 %) gases were purchased from Air Liquide. CH_4 (> 99 %) was from Fluka. ^{13}CO (99 % content in atom ^{13}C) and $^{13}\text{CO}_2$ (99 % content in atom ^{13}C) were purchased from Sigma Aldrich. High purity hydrogen was generated from an F-DBS Hydrogen Generator (WM-H2 500).

6.1.2 Synthesis and purifications

1,3-dimethyl-2-phenyl-2,3-dihydro-1H-benzo[d]imidazole (BIH)¹³⁵ and 4-bromo-2,2':6',2'':6'',2'''-quaterpyridine were prepared according to literature.

(1, 3-dimethyl-2-phenyl-2, 3-dihydro-1H-benzo[d]imidazole) (BIH) A solution of N, N'-dimethyl-1, 2-phenylenediamine (1.5 g, 7.7 mmol) was treated with 4 g of methyl iodide in 10 mL of methanol containing 0.32 g of NaOH. The reaction mixture was heated at 110 °C overnight in a Pyrex bottle. The longer the reaction period, the higher was the yield of the salt, especially for substances having electron-withdrawing substituents. The brown crude product was decolorized by the activated carbon in hot aqueous ethanol (ethanol:H₂O, 5:1 v/v). After removal of the solvent, the product was recrystallized from absolute ethanol. The yield was over 80%. Without further purification, to a solution of 1.7 g this product in 60 mL of CH₃OH was slowly added with 459 mg NaBH₄ in ice-bath. The reaction took place instantaneously to give a cloudy, white suspension. The reaction mixture was stirred vigorously for 1 h under Ar. After removal of the solvent under reduced pressure, the white solid was recrystallized from ethanol:H₂O (2:1 v/v) to give a colorless crystalline product. The yield was over 80% (0.87 g). IR (KBr) 3038 (w), 2953

(w), 2861 (w), 2801 (w), 1601 (m), 1495 (s), 1456 (m), 1368 (s), 1295 (m), 1234 (m), 1157 (m), 1121 (m), 1061 (m), 777 (m), 741 (m), 700 (m) cm^{-1} ; $^1\text{H-NMR}$ (DMSO-d_6) δ 2.52 (s, 6 H, NCH_3), 4.88 (s, 1 H, 2-H), 6.46 (m, 2 H, 5-H), 6.64 (m, 2 H, 4-H), 7.44-7.59 (m, 5 H, phenyl); UV-vis (2-propanol- H_2O , 4:1 v/v) λ_{max} nm (log ϵ) 312 (3.82), 260 (3.70).

4-([2,2':6',2'':6'',2'''-quaterpyridin]-4-yl)benzoic acid (qpy-Ph-COOH).

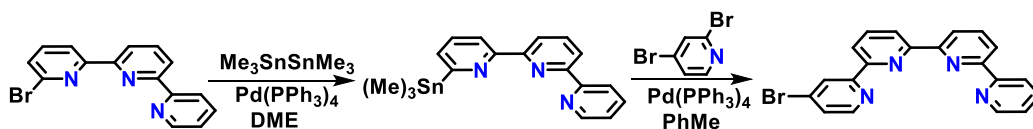
A mixture of 4-bromo-2,2':6',2'':6'',2'''-quaterpyridine (117 mg, 0.30 mmol), 4-methoxycarbonyl-phenylboronic acid (63 mg, 0.35 mmol), $\text{Pd}(\text{PPh}_3)_4$ (17.3 mg, 0.015 mmol) and Na_2CO_3 (159 mg, 1.5 mmol) in $\text{MeOH}/\text{H}_2\text{O}$ (10 mL, 10:1) was refluxed for 24 h under argon. After evaporating solvent, the residue was washed with water and isopropanol to give crude methyl 4-([2,2':6',2'':6'',2'''-quaterpyridin]-4-yl)benzoate, which was used without further purification. To the crude methyl 4-([2,2':6',2'':6'',2'''-quaterpyridin]-4-yl)benzoate in $\text{THF}/\text{MeOH}/\text{H}_2\text{O}$ (6 mL, 4:1:1) was added LiOH (3.0 mmol, 127 mg), then the mixture was refluxed for 12 h. After cooling down, the mixture was filtered and acidified with 1 M HCl . Upon removing organic solvent, white product (qpy-Ph-COOH) was precipitated out. The solid was filtered and washed with water. After drying under vacuum for 12h, qpy-Ph-COOH was obtained as a white solid (Figure S1). Yield: 87 mg (67%). $^1\text{H NMR}$ (400MHz, DMSO-d_6): δ 8.98 (s, 1H), 8.92-8.88 (m, 3H), 8.85 (d, $^3J_{(\text{H,H})} = 4.0$ Hz, 1H), 8.76 (d, $^3J_{(\text{H,H})} = 8.0$ Hz, 1H), 8.63 (d, $^3J_{(\text{H,H})} = 8.0$ Hz, 1H), 8.55 (d, $^3J_{(\text{H,H})} = 8.0$ Hz, 1H), 8.28-8.22 (m, 3H), 8.17-8.12 (m, 4H), 8.03 (d, $^3J_{(\text{H,H})} = 4.0$ Hz, 1H), 7.70 (t, $^3J_{(\text{H,H})} = 8.0$, 1H).

Synthesis of Coqpy-Ph-COOH.

A mixture of qpy-Ph-COOH (43 mg, 0.1 mmol) and $\text{CoCl}_2 \cdot 6\text{H}_2\text{O}$ (36 mg, 0.15 mmol) in MeOH (20 mL) was stirred at room temperature for 24 h. After evaporating solvent, the residue was washed with water and isopropanol to give $\text{Coqpy-Ph-COOHCl}_2 \cdot 2.5\text{H}_2\text{O}$ as a pale yellow solid (Figure S1). Yield: 50 mg (83 %). $\text{Coqpy-Ph-COOH} \cdot \text{Cl}_2 \cdot 2.5\text{H}_2\text{O}$: Anal. Calcd. (Found) for $\text{C}_{27}\text{H}_{18}\text{Cl}_2\text{CoN}_4\text{O}_2 \cdot 2.5\text{H}_2\text{O}$: C, 53.57 (53.68), H, 3.83 (3.66), N, 9.26

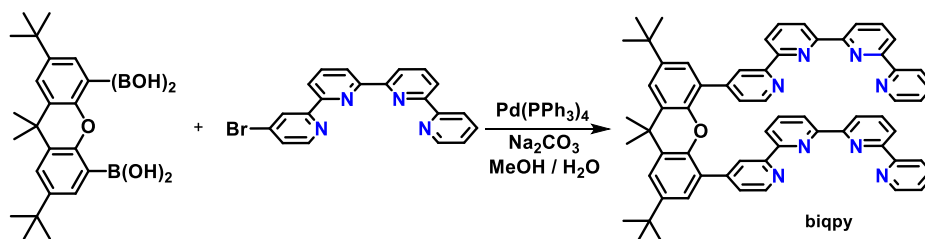
(9.15). ESI-MS in MeOH (Figure S2): m/z 244.7, [Coqpy-Ph-COOH]²⁺; 524.0, [Coqpy-Ph-COOH Cl]⁺.

Synthesis of 4-bromo-2,2':6',2'':6'',2'''-quaterpyridine.



A mixture of 6-bromo-2,2':6',2''-terpyridine (0.57 g, 1.80 mmol), hexamethyldistannane (0.60 g, 1.84 mmol) and Pd(PPh₃)₄ (0.10 g, 0.08 mmol) in dry DME (25 mL) was heated at 80 °C for 24 h. After evaporating the solvent, the residue was pumped under vacuum for 12 h. Then 2,4-dibromopyridine (1.76 g, 5.4 mmol), LiCl (0.16 g, 3.4 mmol), Pd(PPh₃)₄ (0.15 g, 0.12 mmol) and dry toluene (40 mL) was added and refluxed for 48 h under argon. After removing the solvent, the residue was purified by column chromatography on alumina using dichloromethane/petroleum ether (1:2) as eluent to afford 4-bromo-2,2':6',2'':6'',2'''-quaterpyridine as a white solid. Yield: 0.18 g (25%). ¹H NMR (400MHz, CDCl₃): δ 8.82 (d, J₁ = 1.4 Hz, 1H), 8.72-8.63 (m, 4H), 8.52-8.44 (m, 3H), 8.04-7.98 (m, 2H), 7.88 (td, J₁ = 7.7 Hz, J₂ = 1.2 Hz, 1H), 7.51 (dd, J₁ = 5.2 Hz, J₂ = 1.7 Hz, 1H), 7.36-7.33 (m, 1H). ¹³C NMR (100MHz, CDCl₃): δ 157.49, 156.15, 155.53, 155.32, 155.03, 153.89, 149.79, 149.12, 137.87, 137.87, 136.83, 133.85, 126.85, 124.49, 123.75, 121.60, 121.28, 121.14, 121.14, 121.07.

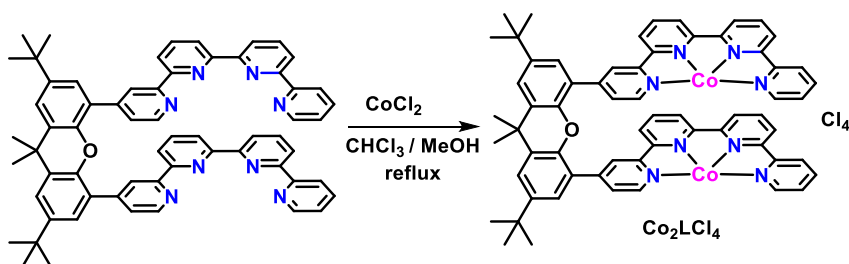
4,4''''-(2,7-di-tert-butyl-9,9-dimethyl-9H-xanthene-4,5-diyl)di-2,2':6',2'':6'',2'''-quaterpyridine (L).



4,4''''-(2,7-di-tert-butyl-9,9-dimethyl-9H-xanthene-4,5-diyl) di-2,2':6',2'':6'',2'''-quaterpyridine (biqpy) was synthesized by the coupling of 4-bromo-2,2':6',2'':6'',2'''-

quaterpyridine with 2,7-di-tert-butyl-9,9-dimethylxanthene-4,5-diboronic acid, using Pd(PPh₃)₄ as a catalyst. A mixture of 4-bromo-2,2':6,2'':6'',2'''-quaterpyridine (78 mg, 0.2 mmol), 2,7-di-tert-butyl-9,9-dimethylxanthene-4,5-diboronic acid (41 mg, 0.1 mmol), Pd(PPh₃)₄ (24 mg, 0.01 mmol) and Na₂CO₃ (106 mg, 1.0 mmol) in iPrOH/PhMe/H₂O (10 mL, 10:10:1) was refluxed for 16 h under argon. After evaporating solvent, the residue was purified by column chromatography on alumina using dichloromethane/petroleum ether (2:1) S6 / S30 as an eluent to afford 4,4''''-(2,7-di-tert-butyl-9,9-dimethyl-9H-xanthene-4,5-diyl) di2,2':6,2'':6'',2'''-quaterpyridine (L) as a white solid. Yield: 84 mg (80%). ¹H NMR (400MHz, CDCl₃): δ 8.54 (d, J = 4.2 Hz, 1H), 8.46 (s, 1H), 8.39 (d, J = 7.9 Hz, 1H), 8.36 (d, J = 7.8 Hz, 1H), 8.28 (d, J = 7.7 Hz, 1H), 8.24 (d, J = 5.0 Hz, 1H), 8.18 (d, J = 2.5 Hz, 1H), 8.16 (d, J = 2.5 Hz, 1H), 7.84 (t, J = 7.8 Hz, 1H), 7.70 (td, J = 7.8, J2 = 1.3, 1H), 7.66 (t, J = 7.8, 1H), 7.59 (d, J = 2.2 Hz, 1H), 7.30 (d, J = 2.2 Hz, 1H), 7.19-7.16 (m, 2H), 1.85 (s, 3H), 1.40 (s, 9H). ¹³C NMR (101 MHz, CDCl₃) δ 155.96, 155.22, 154.83, 154.55, 154.55, 154.40, 148.74, 148.20, 146.56, 146.01, 145.55, 137.18, 137.18, 136.47, 130.28, 127.16, 125.60, 124.28, 123.31, 123.03, 121.81, 120.99, 120.92, 120.73, 120.47, 120.40, 35.14, 34.65, 32.17, 31.52. ESI-MS in MeOH: m/z 939.6, [biqpy + H]⁺.

Synthesis of Co₂biqpyCl₄.



Treatment of biqpy with excess CoCl₂ in MeCN affords the binuclear compound Co₂(biqpy)Cl₄ in high yield. Electrospray ionization mass spectrometry (ESI-MS) exhibits peaks at m/z 364.0, 564.6 and 1,161.5, which are assigned to the triply-charged [Co₂(biqpy)Cl]³⁺, doubly-charged [Co₂(biqpy)Cl₂]²⁺ and singly-charged [Co₂(biqpy)Cl₃]⁺ ions, respectively. Three of the Cl⁻ ions in Co₂(biqpy)Cl₄ were easily replaced by ClO₄⁻ in

methanol, affording $[\text{Co}_2(\text{biqpy})\text{Cl}(\text{MeOH})(\text{H}_2\text{O})](\text{ClO}_4)_3$, which was structurally characterized by X-ray crystallography. Both Co1 and Co2 cobalt atoms are coordinated by four N atoms of biqpy in the equatorial plane, with a bridging Cl^- atom. The Co1–Cl–Co2 angle is 136.02° . The other axial position around Co1 (Co2) is occupied by a water (methanol) molecule. The ESI-MS of $[\text{Co}_2(\text{biqpy})\text{Cl}(\text{MeOH})(\text{H}_2\text{O})](\text{ClO}_4)_3$ in MeCN exhibits peaks at m/z 264.3 and 586.4, which are respectively assigned to the quadruplycharged $[\text{Co}_2\text{L}]^{4+}$ and doubly-charged $[\text{Co}_2(\text{biqpy})(\text{OH})(\text{ClO}_4)]^{2+}$, indicating that the $\mu\text{-Cl}$ atom between Co1 and Co2 is labile in solution.

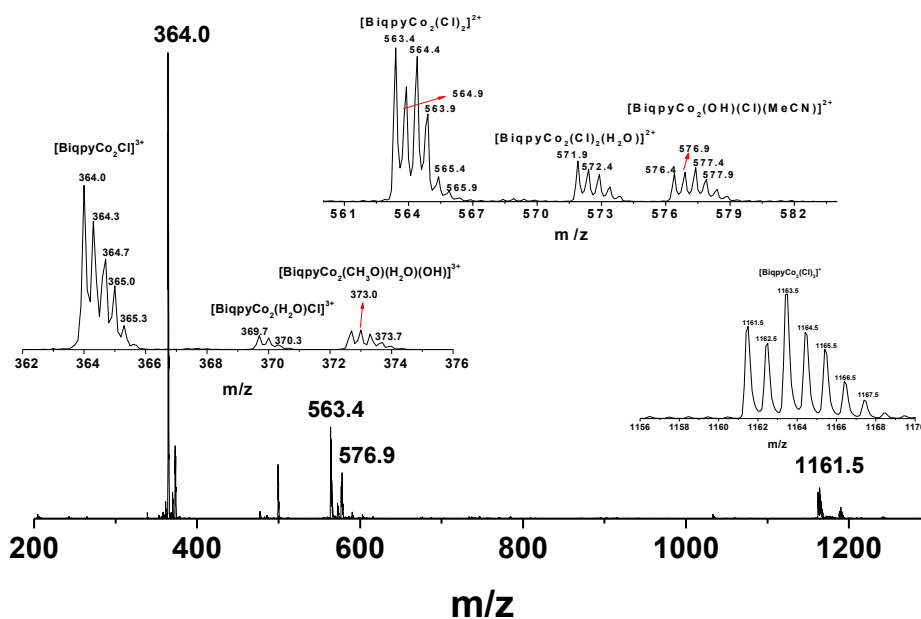


Fig. 6.1 ESI-Mass spectra of the Co_2LCl_4 in ACN.

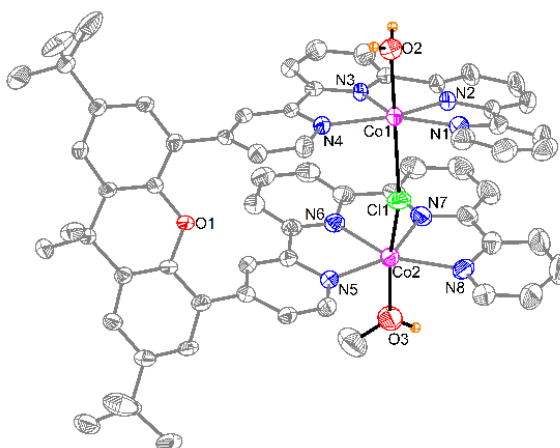


Fig. 6.2 Crystal structure of $[\text{Co}_2(\text{biqpy})\text{Cl}(\text{MeOH})(\text{H}_2\text{O})]^{3+}$. ORTEP drawing of the complex. Thermal ellipsoids are drawn at 50% probability. Hydrogen atoms (except O-H) and solvent molecules are omitted for clarity.

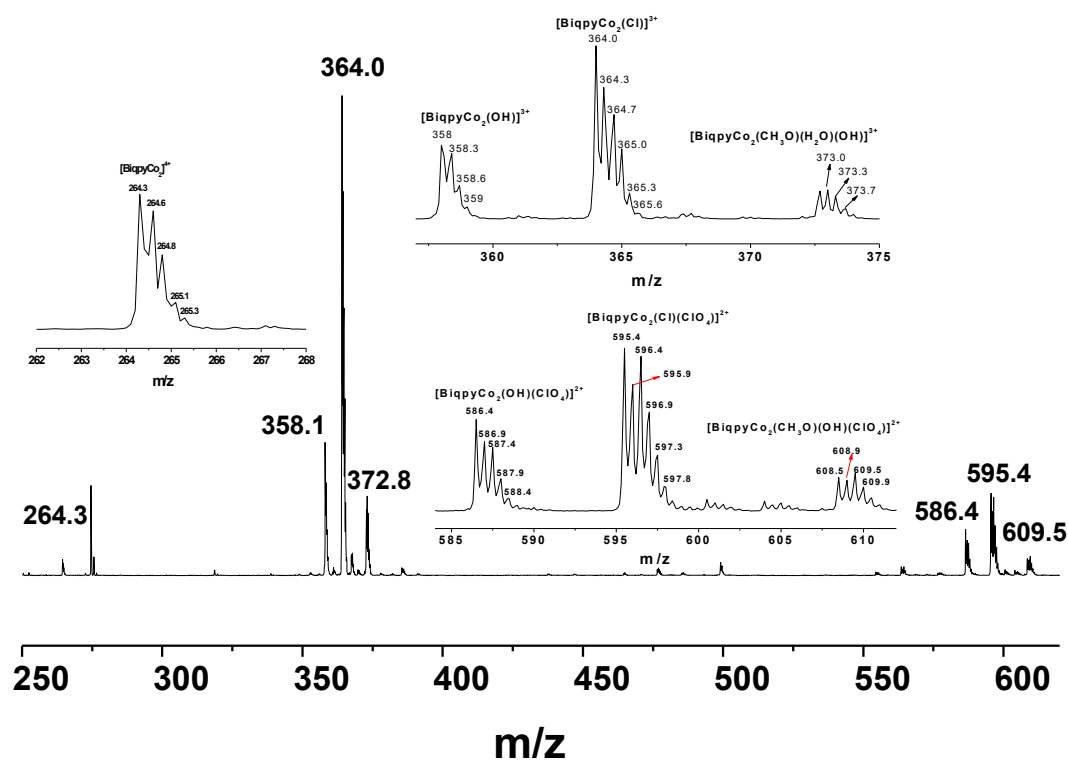


Fig. 6.3 ESI-MS of $[\text{Co}_2\text{LCl}(\text{MeOH})(\text{H}_2\text{O})](\text{ClO}_4)_3$.

Ru(phen)₃Cl₂. Ru(phen)₃Cl₂ used in this study was synthesized according to literature method using 1,10-phenanthroline instead of 2,2'-bipyridine (bpy). A mixture of RuCl₃·3H₂O (2.5 mmol, 0.66g) and 1,10-phenanthroline (12.5 mmol, 2.25 g) in 95% ethanol was refluxed for 72 h under argon. The dark orange-red solution was filtered and then evaporated to dryness to give Ru(phen)₃Cl₂ as an orange-red solid, which was recrystallized in hot water. Yield: 1.20 g (67%). Anal. Calcd. for C₃₆H₂₄Cl₂RuN₆·7H₂O: C, 51.55; H, 4.57; N, 10.02; found (C, 51.19; H, 4.24; N, 10.01).

g-C₃N₄. The g-C₃N₄ photocatalyst used in this study was synthesized according to literature method.¹³⁶ 10.0 g urea was calcined at 550°C for 2 h at a heating rate of 5°C min⁻¹ in alumina crucible with cover. The pale yellow g-C₃N₄ was characterized by XRD, SEM and IR.

6.2 Characterization Methods

6.2.1 UV-visible spectroscopy

UV-visible absorption measurements were done with an Agilent Technologies Cary 60 or an Analytic Jena Specord 600 UV/VIS spectrophotometer. Aliquots of the solution were poured into a quartz cell (1 cm length). Typical spectral region ranged from 200-800 nm and it was swept at a rate of 720 nm s^{-1} .

6.2.2 Solar simulator

The main figure-of-merit for a solar CO₂ reduction device is its performance under real sunlight. However, even real sunlight does not have the same intensity and spectral distribution everywhere on earth. To facilitate meaningful comparisons of device performances, the performance characteristics are usually quoted for the so-called AM 1.5G conditions. This stands for “air mass 1.5 global”, and refers to the spectral distribution and intensity of sunlight on a 37° south-facing tilted surface after it has traveled through 1.5 times the thickness of the earth’s atmosphere. The latter corresponds to a solar zenith angle of 48.19. The AM 1.5G spectrum includes both the direct and the diffuse contributions of the incident sunlight, and has a total integrated intensity of 1000 W/m². The most recent and widely used AM 1.5G reference spectrum is published by the American Society for Testing and Materials as the ASTM-G173-03 standard, and represents a reasonable average for the 48 contiguous states of the USA over a period of 1 year [ASTM G173-03(2012), Standard Tables for Reference Solar Spectral Irradiances: Direct Normal and Hemispherical on 37° Tilted Surface, ASTM International, West Conshohocken, PA, 2012, <https://www.astm.org/Standards/G173.htm>]. The corresponding international standard is IEC 60904-3 (3rd edition, 2016).

Since real AM 1.5G sunlight is not readily available at all times and at all locations, solar simulators are used. Making a reasonably good solar simulator is far from trivial. One cannot use halogen lamps since their maximum color temperature is limited to ~3200 K, which is much lower than the color temperature of the sun (5800 K). Xenon lamps are

widely accepted to give the best match to the solar spectrum. Newport LCS-100 solar simulator is usually used in photovoltaic cell research requiring a certified system for small illumination areas. The 38×38 mm simulators meet Class ABB as defined by ASTM, IEC and JIS standards. All electronics are built into the lamp housing and are factory preset to run the 100 W xenon bulb with integrated reflector at the proper current and voltage. For replacement assemblies, a “drop in” design eliminates the need for lamp alignment. An integrated attenuator allows partial sun irradiance.

In addition, optical filters are used to optimize the overall spectral shape and to remove (to some extent) the sharp lines in the emission spectrum of xenon. Schott long-pass filters (also known as edge filters) possess a steep absorption range. This property allows for a sharp separation between the blocking and transmission range. Moreover, the filters are practically insensitive to the angle of installation. In this thesis, both Schott GG420 and GG435 long pass filters are used.

6.2.3 Fluorescence spectroscopy

Emission quenching measurements were conducted with a Cary Eclipse fluorescence spectrophotometer (Agilent Technologies), with the excitation wavelength set at 420 nm ($[\text{Ru}(\text{phen})_3]^{2+}$) or 400 nm (mpg- C_3N_4) and the emission intensities used for the Stern-Volmer analysis were taken at 600 nm ($[\text{Ru}(\text{phen})_3]^{2+}$), 488 nm (mpg- C_3N_4), 543 nm (mpg- C_3N_4), that is, the emission maximum of PS.

6.2.4 Transient absorption spectroscopy

Transient absorption kinetic was measured with an Edinburgh Instruments LP920-KS laser flash photolysis spectrometer. The solutions were excited at 420 nm (5 ns pulse, 2 to 4 mW per pulse) *via* a Continuum SLOPO Plus OPO pumped by a frequency-tripled Continuum Surelite II- 10 Nd:YAG laser. Right-angle probe light was provided by an Osram XBO 450 W ozone free pulsed xenon lamp and then collected into a spectrograph. Excited state lifetime of Phen4 was determined by measuring kinetics of the ground state recovery at 390 nm, *i.e.* the absorption maximum of Phen4, thanks to a Hamamatsu R928

photomultiplier tube linked to a Tektronix TDS 3012C 100 MHz oscilloscope. Temperature of the sample port was set at 20°C by a Quantum Northwest TC125 Peltier effect controller. The Edinburgh Instruments L900 software ensured the control and the synchronization of the whole setup.

6.2.5 Frontier Infrared (FT-IR) spectroscopy

Infrared spectra were recorded on a PerkinElmer Spectrum BX FTIR spectrometer equipped with a Specac Omni Cell P/N 800 measurement cell. The Omni-Cell™ is a multidisciplinary support allowing the simple analysis in static mode and at ambient temperature of sample in transmission mode. This support accepts both rectangular windows for the analysis of liquids and round windows for analysis according to the technique "Mull", the windows for the analysis of liquid being available in removable or seals.

6.2.6 Nuclear magnetic resonance (NMR) spectroscopy

The ¹H NMR and ¹³C NMR spectra were recorded on a Bruker Avance III 400-MHz spectrometer and were referenced to the resonances of the solvent used.

6.2.7 Gas chromatography (GC) and Gas chromatography-Mass (GC-MS)

Gas chromatography analyses of gas evolved in the headspace during the electrolysis were performed with an Agilent Technologies 7820A GC system equipped with a thermal conductivity detector. H₂, CO and CH₄ production was quantitatively detected using a CP-CarboPlot P7 capillary column (25 m in length and 25 μm internal diameter). Temperature was held at 150°C for the detector and 35°C for the oven. The carrier gas was argon flowing at 7.95 mL/min at constant pressure of 0.6 bars. Injection was performed via a 250 μL gas-tight (Hamilton) syringe previously degassed with CO₂. Conditions allowed detection of H₂, O₂, N₂, CO, and CO₂. Calibration curves for H₂, CO and CH₄ were determined separately by injecting known quantities of pure gas.

GC-MS for detecting the labeled gas products were obtained by a ThermoFisher Scientific TRACE Ultra gas chromatograph equipped with a CP 7514 column (Agilent

Technologies) and coupled to a DSQ II mass spectrometer in positive ionization mode, using a TriPlus headspace autosampler.

The mass spectra for detecting the organic compounds were recorded on a Microtof-Q of Bruker Daltonics. Injection method was high resolution electrospray (ESI).

6.2.8 Ionic chromatography (IC)

Ionic chromatography (IC) was used for the detection and quantification of formate in aqueous and organic samples recovered from the reactor after decompression. The presence of other anions, such as acetate, fluoride, chloride, oxalate, etc. can also be determined using this technique. Ionic chromatography measurements were performed with a Thermo Scientific Dionex ICS-1100 system equipped with a Dionex ERS 500 electrolytically regenerated suppressor. All the samples were diluted 50 folds with ultra-pure water before analyzed through IC. Calibration curve for formate was determined separately by injecting known quantities of pure sample.

6.2.9 pH measurements

pH measurements were performed with Hanna pH210 and HI221 instruments and 6 mm microelectrodes (Fisher).

6.2.10 Cyclic voltammetry

Cyclic voltammograms were obtained in a three-electrode cell by use of a Metrohm Autolab potentiostats/galvanostat interfaced with Nova software. The working electrode was a 3 mm diameter glassy carbon disk carefully polished with 1 μm diamond paste (DP-PasteM) then thoroughly rinsed in acetone then absolute ethanol before use. The counterelectrode was a platinum wire and the reference electrode was an aqueous SCE electrode. All experiments were carried out either under argon or carbon dioxide atmosphere at 21°C, the double-wall jacketed cell being thermostated by circulation of water. The cell was sealed during measurements and the solution was saturated with argon or carbon dioxide between measurements. Ohmic drop was compensated through the positive feedback compensation method implemented in the instrument.

6.2.11 X-ray photoelectron spectroscopy (XPS)

The composition (contents in oxygen, nitrogen, carbon, and cobalt elements) of samples were determined by X-ray photoelectron spectroscopy (XPS) recorded on an ESCALAB 250 spectrometer (Thermo Sci.) accompanied by a microfocalized X-ray source ($K\alpha$ Al 1486.6 eV) and a double monochromator.

6.2.12 Inductively Coupled Plasma - Optical Emission Spectroscopy (ICP-OES)

Inductively coupled plasma-optical emission spectroscopy (ICP-OES) was obtained with an iCAP 6300 ICP-OES CID spectrometer (Thermo Sci.) to determine the concentration in Co in the different hybrid materials. A test was performed with a RACHID detector including a diode array, a peristaltic pump, and argon plasma (analyzes present at 50 rpm, 1150 W). Heterogeneous samples were preprocessed by acid digestion with concentrated nitric acid. In the present case, 2.0 mg of solid sample was introduced into 1.0 mL of concentrated nitric acid and heated on a hot plate. After cooling to room temperature, the reaction solution was filtered. Then the filtrate was diluted into a 10.0 mL volumetric flask of ultrapure water for testing.

6.2.13 Photochemical experiments setup

Each solution was prepared just before the experiment. The solvent was degassed with Ar for approximately 10 min, and then TEA and/or TFE was added. After keeping the solution approximately 5 more minutes under Ar atmosphere, it was poured with a syringe onto the solid porphyrin and photosensitizer previously placed under inert atmosphere. Then, the solution (3.5 mL) was transferred to a sealable fluorescence 1×1 cm quartz Suprasil cuvette (Hellma 117.100F-QS) equipped with a home-made glassware, leaving a headspace of approximately 23 mL (see Scheme 5.1). The cuvette was degassed previously through a vial filled with the solvent, TFE, and Et_3N (if present) for approximately 20 min with Ar, CO_2 or CO to prevent any evaporation. Then, the solution in the cuvette was irradiated perpendicularly with a Xenon lamp through an irradiation

window of 5 cm × 5 cm by using a Schott GG optical filter and a 2 cm long glass OS cell filled with water to cut off IR. Gas products were analyzed via GC and liquid products were analyzed via ¹H NMR, ¹³C NMR and IC. UV-vis analysis was made directly via the home-made glassware.

6.2.14 X-ray powder diffraction (XRD)

X-ray powder diffraction patterns were recorded by using a the PANALYTICAL X'PERT PRO diffractometer equipped with a Co tube and an X'celerator detector at room temperature.

6.2.15 Electrochemical and photoelectrochemical measurements

For photocurrent measurements of Coqpy@mpg-C₃N₄, 2 mg of each solid material was suspended into 250 μL of DMF. The obtained catalytic ink was then dropped on one face of a fluorine-doped tin oxide (FTO) glass electrode (150 μL for a 1 cm²) and allowed to dry under ambient conditions prior to use it as the working electrode. The Coqpy/mpgC₃N₄ sample was prepared by grinding mpg-C₃N₄ with Coqpy-PhCOOH. All electro- and photoelectrochemical experiments were performed in a glass cell with a quartz window in 0.1 M Na₂SO₄ electrolyte by using a conventional three-electrode system with a platinum wire as a counter electrode and a saturated calomel electrode (SCE) as reference (-0.241 V vs. NHE). Light illumination was provided by a 300 W xenon lamp (Oriel Inst.). The amperometric photocurrent was measured for each switch on/off event by using an Autolab PGSTAT 128N potentiostat (Metrohm) with no bias voltage under the UV-vis light irradiation with light chopping every 20 s.

Electrochemical impedance spectroscopy (EIS) plots were measured by using a PARSTAT 4000 potentiostat (Princeton Applied Res.) at the corresponding open circuit potential over the frequency ranging from 0.1 to 106 Hz in the dark.

6.2.16 Scanning Electron Microscope (SEM)

SEM images were taken on a a Zeiss MEB-FEG (Zeiss SUPRA 40) Scanning Electron Microscope with an continuously variable acceleration voltage from 100V to 30kV. The

scanning electron microscope equipped with a high efficiency In-Lens secondary electron detector in axial position and an NPGS lithography device allowing the fabrication of nanostructures.

6.2.17 X-ray Absorption Spectroscopy (XAS)

X-ray adsorption spectroscopy (XAS) measurements were recorded on beamline B18 at Diamond Light Source (UK) with ring energy of 3 GeV and a current of 300 mA. The monochromator used was Si(311) crystals operating in Quick EXAFS (QEXAFS) mode. Pellets of Coqpy@GA and CoqpyNH₂.Cl₂ were measured in transmission mode at the Co K (7709 eV) absorption edge at 298 K using a 36-element Ge detector. The Co foil was measured simultaneously. Calibration of the monochromator was carried out using the Co foil previously to the measurements. The acquired data were processed and analyzed using the Athena and Artemis programs, respectively, which implement the FEFF6 and IFEFFIT codes.

Notations

[Q]	quencher concentration
c	speed of light
C	total passed charge
E	potential
E^0	redox potential
E_{CB}	conduction band potential
E_g	bandgap energy
E_p	energy of photon
E_{VB}	valence band potential
F	Faradaic constant
h	Planck's constant
I	emission intensity with a quencher
I_0	emission intensity
k_q	apparent quenching rate constant
n	number of needed electrons for product evolution
t	reaction time
T	temperature
v	scan rate
w_P	work terms required to bring the product
w_R	work terms required to bring the reactant
γ	γ -radiation
ΔG^0	Gibbs free energy
ΔH^0	Standard enthalpy
ϵ_S	solvent dielectric constant
λ	photon wavelength
λ_{ex}	excited wavelength
ν	photon frequency
τ_0	excited-state lifetime
Φ	quantum yield

Terms and Abbreviations

IEO2017	International Energy Outlook 2017
9CNA	9-cyanoanthracene
AA	ascorbic acid
ACN	acetonitrile
ASA	amino salicylic acid
ATP	adenosine triphosphate
BIH	1,3-dimethyl-2-phenyl-2,3-dihydro-1H-benzo[d]imidazole
BNAH	1-benzyl-1,4-dihydronicotinamide
bpy	2, 2'-bipyridine
C ₂ H ₄	ethylene
C ₂ H ₅ OH	ethanol
C ₂ H ₆	ethane
C ₃ H ₇ OH	n-propanol
CAT	catalyst
CB	conduction band
CH ₃ OH	methanol
CH ₄	methane
CO	carbon monoxide
CO ₂	carbon dioxide
Coqpy	cobalt quaterpyridine
CS	catalytic selectivity
CV	cyclic voltammetry
cyclam	1, 4, 8, 11-tetraazacyclotetradecane
DFT	density functional theory
DIPEA	N, N-diisopropylethylamine
DMF	N, N'-dimethylformamide
EA	electron acceptor
EDTA	ethylenediamine tetraacetic acid
FE	faradaic efficiency
GC	gas chromatography
g-C ₃ N ₄	graphitic carbon nitride
H ₂ C ₂ O ₄	oxalic acid
HCHO	formaldehyde
HCOO ⁻	formate
HCOOH	formic acid
HOMO	highest occupied molecular orbital
IR	infrared
LMCT	ligand to metal charge transfer
LUMO	lowest unoccupied molecular orbital
MC	metallocorrole

MEDA	2-(dimethylamino)ethanethiol
MLCT	metal-to-ligand charge transfer
MS	mass spectrum
NHC	N-heterocyclic carbene
NHE	normal hydrogen electrode
NP	nanoparticle
PCAT	photocatalyst
PCET	proton-coupled electron transfer
PhOH	phenol
PP	purpurin
PS	photosensitizer
QD	quantum dot
qpy	2, 2': 6', 2'': 6'', 2'''-quaterpyridine
QY	quantum yield
RDS	rate determining step
SC	semiconductor
SCE	saturated calomel electrode
SD	sacrificial electron donor
TEA	triethylamine
TEOA	triethanolamine
TFE	2, 2, 2-trifluoroethanol
THF	tetrahydrofuran
TOF	turnover frequency
TON	turnover number
UV	ultra violet
UV-Vis	ultraviolet-visible
VB	valence band
WE	work electrode

Acknowledgements

My deep gratitude goes first to Prof. Marc Robert and Dr. Julien Bonin, who expertly guided me through my Ph.D. study and who shared the excitement of three years of discovery. Marc's early insights launched the greater part of this thesis, and Julien's mentoring and encouragement have been especially valuable. Their unwavering enthusiasm for science kept me constantly engaged with my research, and their personal generosity helped make my time at Paris enjoyable.

My appreciation also extends to all the professors, researchers, and engineers in Laboratoire d'Electrochimie Moléculaire for their kindly help and training. Thanks also go to the experimental assistance work in Lavoisier and Lamark building. Particular thanks go to Dr. Mathieu Branca and Dr. Claire Fave for their instruction and generous support during these years.

Also, I owe many thanks to my laboratory colleagues Prof. Elodie, Niklas, Orestes, Heng, Claudio, Etienne, Thomas, Kristian, Tamal, Thamires, Alexis, Geordie, Min, Lydia, Benjamin, Martin, Ruwen, Marie, Dorian, Fuhuan, Daniela, Nikolaos, Anandi, Julian, who have taught me a lot in this university, for leading me into a challenging yet fascinating field of academic research. The profit that I gained from them will be of ever lasting significance to my future research. What's more, I would like to present my thanks to my friends in LEM, Justine, Hussein, Esther, Daniel, Sihem and Telmo, from whom I get tremendous love and encouragement as well as technical instruction.

Above ground, I am indebted to my family members and friends, whose value to me only grows with age. They helped me and shared with me my worries, frustrations, and happiness. Choosing to start doctoral research is a decision worthy of my lifelong benefit. These three years full of challenges and rewards will be an important transformation in my life. I hope this paper will not be the end of academic thinking, and I hope that the previous sentence is not just hope.

Bibliography

1. R. L. Purchase and H. J. M. de Groot, *Interface Focus*, 2015, **5**.
2. M. D. Kärkäs, O. Verho, E. V. Johnston and B. Åkermark, *Chemical Reviews*, 2014, **114**, 11863-12001.
3. H. Dau, E. Fujita and L. Sun, *ChemSusChem*, 2017, **10**, 4228-4235.
4. E. S. Andreiadis, M. Chavarot-Kerlidou, M. Fontecave and V. Artero, *Photochemistry and Photobiology*, 2011, **87**, 946-964.
5. A. Polman, M. Knight, E. C. Garnett, B. Ehrler and W. C. Sinke, *Science*, 2016, **352**, 4424.
6. Z. W. Seh, J. Kibsgaard, C. F. Dickens, I. Chorkendorff, J. K. Nørskov and T. F. Jaramillo, *Science*, 2017, **355**, 4998.
7. A. Wang, J. Li and T. Zhang, *Nature Reviews Chemistry*, 2018, **2**, 65-81.
8. Y. Wang, J. Mao, X. Meng, L. Yu, D. Deng and X. Bao, *Chemical Reviews*, 2019, **119**, 1806-1854.
9. Y. Zhao, K. R. Yang, Z. Wang, X. Yan, S. Cao, Y. Ye, Q. Dong, X. Zhang, J. E. Thorne, L. Jin, K. L. Materna, A. Trimpalis, H. Bai, S. C. Fakra, X. Zhong, P. Wang, X. Pan, J. Guo, M. Flytzani-Stephanopoulos, G. W. Brudvig, V. S. Batista and D. Wang, *Proceedings of the National Academy of Sciences*, 2018, **115**, 2902.
10. E. Boutin, L. Merakeb, B. Ma, B. Boudy, M. Wang, J. Bonin, E. Anxolabéhère-Mallart and M. Robert, *Chemical Society Reviews*, 2020, 5772-5809.
11. X. Chen, S. Shen, L. Guo and S. S. Mao, *Chemical Reviews*, 2010, **110**, 6503-6570.
12. A. H. A. Tinnemans, T. P. M. Koster, D. H. M. W. Thewissen and A. Mackor, *Recueil des Travaux Chimiques des Pays-Bas*, 1984, **103**, 288-295.
13. K. Mochizuki, S. Manaka, I. Takeda and T. Kondo, *Inorganic Chemistry* 1996, **35**, 5132-5136.
14. E. Fujita, D. J. Szalda, C. Creutz and N. Sutin, *Journal of the American Chemical Society*, 1988, **110**, 4870-4871.
15. E. Fujita, C. Creutz, N. Sutin and B. S. Brunshwig, *Inorganic Chemistry*, 1993, **32**, 2657-2662.
16. T. Ogata, S. Yanagida, B. S. Brunshwig and E. Fujita, *Journal of the American Chemical Society*, 1995, **117**, 6708-6716.
17. T. Ogata, S. Yanagida, B. S. Brunshwig and E. Fujita, *Energy Conversion and Management*, 1995, **36**, 669-672.
18. E. Fujita, L. R. Furenlid and M. W. Renner, *Journal of the American Chemical Society*, 1997, **119**, 4549-4550.
19. M. Shinjiro, Y. Kiichi, P. Chyongjin and Y. Shozo, *Chemistry Letters*, 1991, **20**, 2099-2100.
20. S. Matsuoka, K. Yamamoto, T. Ogata, M. Kusaba, N. Nakashima, E. Fujita and S. Yanagida, *Journal of the American Chemical Society*, 1993, **115**, 601-609.
21. T. Ogata, Y. Yamamoto, Y. Wada, K. Murakoshi, M. Kusaba, N. Nakashima, A. Ishida, S. Takamuku and S. Yanagida, *The Journal of Physical Chemistry*, 1995,

-
- 99**, 11916-11922.
22. L. Chen, Z. Guo, X.-G. Wei, C. Gallenkamp, J. Bonin, E. Anxolabéhère-Mallart, K.-C. Lau, T.-C. Lau and M. Robert, *Journal of the American Chemical Society*, 2015, **137**, 10918-10921.
 23. J. Grodkowski, T. Dhanasekaran, P. Neta, P. Hambright, B. S. Brunshwig, K. Shinozaki and E. Fujita, *The Journal of Physical Chemistry A*, 2000, **104**, 11332-11339.
 24. D. Behar, T. Dhanasekaran, P. Neta, C. M. Hosten, D. Ejeh, P. Hambright and E. Fujita, *The Journal of Physical Chemistry A*, 1998, **102**, 2870-2877.
 25. T. Dhanasekaran, J. Grodkowski, P. Neta, P. Hambright and E. Fujita, *The Journal of Physical Chemistry A*, 1999, **103**, 7742-7748.
 26. J. Grodkowski, D. Behar, P. Neta and P. Hambright, *The Journal of Physical Chemistry A*, 1997, **101**, 248-254.
 27. J. Bonin, M. Chaussemier, M. Robert and M. Routier, *ChemCatChem*, 2014, **6**, 3200-3207.
 28. C. Costentin, G. Passard, M. Robert and J.-M. Savéant, *Journal of the American Chemical Society*, 2014, **136**, 11821-11829.
 29. J. Bonin, M. Robert and M. Routier, *Journal of the American Chemical Society*, 2014, **136**, 16768-16771.
 30. H. Rao, J. Bonin and M. Robert, *Chemical Communications*, 2017, **53**, 2830-2833.
 31. H. Rao, J. Bonin and M. Robert, *ChemSusChem*, 2017, **10**, 4447-4450.
 32. H. Rao, L. C. Schmidt, J. Bonin and M. Robert, *Nature*, 2017, **548**, 74.
 33. H. Rao, J. Bonin and M. Robert, *The Journal of Physical Chemistry C*, 2018, **122**, 13834-13839.
 34. J. Grodkowski, P. Neta, E. Fujita, A. Mahammed, L. Simkhovich and Z. Gross, *The Journal of Physical Chemistry A*, 2002, **106**, 4772-4778.
 35. P. G. Alsabeh, A. Rosas-Hernández, E. Barsch, H. Junge, R. Ludwig and M. Beller, *Catalysis Science & Technology*, 2016, **6**, 3623-3630.
 36. A. Rosas-Hernández, P. G. Alsabeh, E. Barsch, H. Junge, R. Ludwig and M. Beller, *Chemical Communications*, 2016, **52**, 8393-8396.
 37. A. Rosas-Hernández, C. Steinlechner, H. Junge and M. Beller, *Green Chemistry*, 2017, **19**, 2356-2360.
 38. H. Takeda, K. Ohashi, A. Sekine and O. Ishitani, *Journal of the American Chemical Society*, 2016, **138**, 4354-4357.
 39. J. Grodkowski and P. Neta, *The Journal of Physical Chemistry A*, 2000, **104**, 4475-4479.
 40. Y. Qin, L. Chen, G. Chen, Z. Guo, L. Wang, H. Fan, M. Robert and T.-C. Lau, *Chemical Communications*, 2020, **56**, 6249-6252.
 41. H. Rao, C.-H. Lim, J. Bonin, G. M. Miyake and M. Robert, *Journal of the American Chemical Society*, 2018, **140**, 17830-17834.
 42. E. Kimura, X. Bu, M. Shionoya, S. Wada and S. Maruyama, *Inorganic Chemistry*, 1992, **31**, 4542-4546.
 43. C. Herrero, A. Quaranta, S. El Ghachtouli, B. Vauzeilles, W. Leibl and A. Aukauloo, *Physical Chemistry Chemical Physics*, 2014, **16**, 12067-12072.

-
44. K. Nobuko, H. Yuichiro, H. Takuji, S. Hideki and K. Kazuyuki, *Bulletin of the Chemical Society of Japan*, 1999, **72**, 725-731.
 45. X. Wang, V. Goudy, G. Genesio, J. Maynadié, D. Meyer and M. Fontecave, *Chemical Communications*, 2017, **53**, 5040-5043.
 46. C.-Y. Zhu, Y.-Q. Zhang, R.-Z. Liao, W. Xia, J.-C. Hu, J. Wu, H. Liu and F. Wang, *Dalton Transactions*, 2018, **47**, 13142-13150.
 47. T. Ouyang, H.-H. Huang, J.-W. Wang, D.-C. Zhong and T.-B. Lu, *Angewandte Chemie International Edition*, 2017, **56**, 738-743.
 48. T. Ouyang, H.-J. Wang, H.-H. Huang, J.-W. Wang, S. Guo, W.-J. Liu, D.-C. Zhong and T.-B. Lu, *Angewandte Chemie International Edition*, 2018, **57**, 16480-16485.
 49. Z. Guo, G. Chen, C. Cometto, B. Ma, H. Zhao, T. Groizard, L. Chen, H. Fan, W.-L. Man, S.-M. Yiu, K.-C. Lau, T.-C. Lau and M. Robert, *Nature Catalysis*, 2019, **2**, 801-808.
 50. H. Dobbek, V. Svetlitchnyi, L. Gremer, R. Huber and O. Meyer, *Science*, 2001, **293**, 1281.
 51. A. D. Handoko, K. Li and J. Tang, *Current Opinion in Chemical Engineering*, 2013, **2**, 200-206.
 52. B. Zhang and L. Sun, *Chemical Society Reviews*, 2019.
 53. C. Cui, M. Heggen, W.-D. Zabka, W. Cui, J. Osterwalder, B. Probst and R. Alberto, *Nature Communications*, 2017, **8**, 1341.
 54. T. Jin, C. Liu and G. Li, *Chemical Communications*, 2014, **50**, 6221-6224.
 55. C. Liu, T. Jin, M. E. Louis, S. A. Pantovich, S. L. Skraba-Joiner, T. Rajh and G. Li, *Journal of Molecular Catalysis A: Chemical*, 2016, **423**, 293-299.
 56. G. Neri, M. Forster, J. J. Walsh, C. M. Robertson, T. J. Whittles, P. Farràs and A. J. Cowan, *Chemical Communications*, 2016, **52**, 14200-14203.
 57. C. D. Windle, E. Pastor, A. Reynal, A. C. Whitwood, Y. Vaynzof, J. R. Durrant, R. N. Perutz and E. Reisner, *Chemistry – A European Journal*, 2015, **21**, 3746-3754.
 58. K. E. Dalle, J. Warnan, J. J. Leung, B. Reuillard, I. S. Karmel and E. Reisner, *Chemical Reviews*, 2019, **119**, 2752-2875.
 59. X. Wang, I. Thiel, A. Fedorov, C. Copéret, V. Mougel and M. Fontecave, *Chemical Science*, 2017, **8**, 8204-8213.
 60. Y.-L. Zhao and J. F. Stoddart, *Accounts of Chemical Research*, 2009, **42**, 1161-1171.
 61. E. M. Pérez and N. Martín, *Chemical Society Reviews*, 2015, **44**, 6425-6433.
 62. H. L. Smith, R. L. Usala, E. W. McQueen and J. I. Goldsmith, *Langmuir*, 2010, **26**, 3342-3349.
 63. J. A. Mann and W. R. Dichtel, *ACS Nano*, 2013, **7**, 7193-7199.
 64. T. Wu, L. Zou, D. Han, F. Li, Q. Zhang and L. Niu, *Green Chemistry*, 2014, **16**, 2142-2146.
 65. S. Roy and E. Reisner, *Angewandte Chemie International Edition*, 2019, **58**, 12180-12184.
 66. A. D. Jannakoudakis, P. D. Jannakoudakis, E. Theodoridou and J. O. Besenhard, *Journal of Applied Electrochemistry*, 1990, **20**, 619-624.
 67. Y. Xing, L. Li, C. C. Chusuei and R. V. Hull, *Langmuir*, 2005, **21**, 4185-4190.

-
68. K. J. Ziegler, Z. Gu, H. Peng, E. L. Flor, R. H. Hauge and R. E. Smalley, *Journal of the American Chemical Society*, 2005, **127**, 1541-1547.
 69. S. Oh, J. R. Gallagher, J. T. Miller and Y. Surendranath, *Journal of the American Chemical Society*, 2016, **138**, 1820-1823.
 70. M. F. Kuehnel, K. L. Orchard, K. E. Dalle and E. Reisner, *Journal of the American Chemical Society*, 2017, **139**, 7217-7223.
 71. Z. Pan, P. Niu, M. Liu, G. Zhang, Z. Zhu and X. Wang, *ChemSusChem*, 2020, **13**, 888-892.
 72. C. J. Kaminsky, J. Wright and Y. Surendranath, *ACS Catalysis*, 2019, **9**, 3667-3671.
 73. J.-H. Jeoung and H. Dobbek, *Science*, 2007, **318**, 1461.
 74. A. M. Appel, J. E. Bercaw, A. B. Bocarsly, H. Dobbek, D. L. DuBois, M. Dupuis, J. G. Ferry, E. Fujita, R. Hille, P. J. A. Kenis, C. A. Kerfeld, R. H. Morris, C. H. F. Peden, A. R. Portis, S. W. Ragsdale, T. B. Rauchfuss, J. N. H. Reek, L. C. Seefeldt, R. K. Thauer and G. L. Waldrop, *Chemical Reviews*, 2013, **113**, 6621-6658.
 75. J.-W. Wang, D.-C. Zhong and T.-B. Lu, *Coordination Chemistry Reviews*, 2018, **377**, 225-236.
 76. A. Taheri, E. J. Thompson, J. C. Fettinger and L. A. Berben, *ACS Catalysis*, 2015, **5**, 7140-7151.
 77. E. C. Constable, S. M. Elder, M. J. Hannon, A. Martin, P. R. Raithby and D. A. Tocher, *Journal of the Chemical Society, Dalton Transactions*, 1996, 2423-2433.
 78. M. Bourrez, F. Molton, S. Chardon-Noblat and A. Deronzier, *Angewandte Chemie International Edition*, 2011, **50**, 9903-9906.
 79. C.-F. Leung, S.-M. Ng, C.-C. Ko, W.-L. Man, J. Wu, L. Chen and T.-C. Lau, *Energy & Environmental Science*, 2012, **5**, 7903-7907.
 80. Z. Guo, F. Yu, Y. Yang, C.-F. Leung, S.-M. Ng, C.-C. Ko, C. Cometto, T.-C. Lau and M. Robert, *ChemSusChem*, 2017, **10**, 4009-4013.
 81. M. Wang, L. Chen, T.-C. Lau and M. Robert, *Angewandte Chemie International Edition*, 2018, **57**, 7769-7773.
 82. Z. Guo, S. Cheng, C. Cometto, E. Anxolabéhère-Mallart, S.-M. Ng, C.-C. Ko, G. Liu, L. Chen, M. Robert and T.-C. Lau, *Journal of the American Chemical Society*, 2016, **138**, 9413-9416.
 83. C. Cometto, L. Chen, P.-K. Lo, Z. Guo, K.-C. Lau, E. Anxolabéhère-Mallart, C. Fave, T.-C. Lau and M. Robert, *ACS Catalysis*, 2018, **8**, 3411-3417.
 84. C. Cometto, R. Kuriki, L. Chen, K. Maeda, T.-C. Lau, O. Ishitani and M. Robert, *Journal of the American Chemical Society*, 2018, **140**, 7437-7440.
 85. E. Fujita, *Coordination Chemistry Reviews*, 1999, **185-186**, 373-384.
 86. A. Rosas-Hernández, H. Junge and M. Beller, *ChemCatChem*, 2015, **7**, 3316-3321.
 87. S. Sato, T. Morikawa, T. Kajino and O. Ishitani, *Angewandte Chemie International Edition*, 2013, **52**, 988-992.
 88. J. Agarwal, E. Fujita, H. F. Schaefer and J. T. Muckerman, *Journal of the American Chemical Society*, 2012, **134**, 5180-5186.
 89. S. L.-F. Chan, T. L. Lam, C. Yang, S.-C. Yan and N. M. Cheng, *Chemical Communications*, 2015, **51**, 7799-7801.
 90. V. S. Thoi, N. Kornienko, C. G. Margarit, P. Yang and C. J. Chang, *Journal of the*

-
- American Chemical Society*, 2013, **135**, 14413-14424.
91. P. L. Cheung, C. W. Machan, A. Y. S. Malkhasian, J. Agarwal and C. P. Kubiak, *Inorganic Chemistry*, 2016, **55**, 3192-3198.
92. W.-J. Liu, H.-H. Huang, T. Ouyang, L. Jiang, D.-C. Zhong, W. Zhang and T.-B. Lu, *Chemistry – A European Journal*, 2018, **24**, 4503-4508.
93. D. J. Boston, C. Xu, D. W. Armstrong and F. M. MacDonnell, *Journal of the American Chemical Society*, 2013, **135**, 16252-16255.
94. D. Mellmann, P. Sponholz, H. Junge and M. Beller, *Chemical Society Reviews*, 2016, **45**, 3954-3988.
95. H. Takeda, H. Koizumi, K. Okamoto and O. Ishitani, *Chemical Communications*, 2014, **50**, 1491-1493.
96. A. Paul, D. Connolly, M. Schulz, M. T. Pryce and J. G. Vos, *Inorganic Chemistry*, 2012, **51**, 1977-1979.
97. Y. Kuramochi, M. Kamiya and H. Ishida, *Inorganic Chemistry*, 2014, **53**, 3326-3332.
98. Y. Du, R. M. Pearson, C.-H. Lim, S. M. Sartor, M. D. Ryan, H. Yang, N. H. Damrauer and G. M. Miyake, *Chemistry*, 2017, **23**, 10962-10968.
99. Y. Fang and X. Wang, *Chemical Communications*, 2018, **54**, 5674-5687.
100. X. Wang, K. Maeda, A. Thomas, K. Takanabe, G. Xin, J. M. Carlsson, K. Domen and M. Antonietti, *Nature Materials*, 2009, **8**, 76-80.
101. K. Maeda, K. Sekizawa and O. Ishitani, *Chemical Communications*, 2013, **49**, 10127-10129.
102. C. Cometto, L. Chen, E. Anxolabéhère-Mallart, C. Fave, T.-C. Lau and M. Robert, *Organometallics*, 2019, **38**, 1280-1285.
103. D. Tasis, N. Tagmatarchis, A. Bianco and M. Prato, *Chemical Reviews*, 2006, **106**, 1105-1136.
104. P. Singh, S. Campidelli, S. Giordani, D. Bonifazi, A. Bianco and M. Prato, *Chemical Society Reviews*, 2009, **38**, 2214-2230.
105. M. F. L. De Volder, S. H. Tawfick, R. H. Baughman and A. J. Hart, *Science*, 2013, **339**, 535.
106. V. Georgakilas, M. Otyepka, A. B. Bourlinos, V. Chandra, N. Kim, K. C. Kemp, P. Hobza, R. Zboril and K. S. Kim, *Chemical Reviews*, 2012, **112**, 6156-6214.
107. B. Ma, G. Chen, C. Fave, L. Chen, R. Kuriki, K. Maeda, O. Ishitani, T.-C. Lau, J. Bonin and M. Robert, *Journal of the American Chemical Society*, 2020, **142**, 6188-6195.
108. K. Maeda, R. Kuriki, M. Zhang, X. Wang and O. Ishitani, *Journal of Materials Chemistry A*, 2014, **2**, 15146-15151.
109. R. Kuriki, M. Yamamoto, K. Higuchi, Y. Yamamoto, M. Akatsuka, D. Lu, S. Yagi, T. Yoshida, O. Ishitani and K. Maeda, *Angewandte Chemie International Edition*, 2017, **56**, 4867-4871.
110. T. S. Miller, A. B. Jorge, T. M. Suter, A. Sella, F. Corà and P. F. McMillan, *Physical Chemistry Chemical Physics*, 2017, **19**, 15613-15638.
111. K.-M. Lam, K.-Y. Wong, S.-M. Yang and C.-M. Che, *Journal of the Chemical Society, Dalton Transactions*, 1995, 1103-1107.

-
112. X. Wang, S. Blechert and M. Antonietti, *ACS Catalysis*, 2012, **2**, 1596-1606.
 113. P. Huang, J. Huang, S. A. Pantovich, A. D. Carl, T. G. Fenton, C. A. Caputo, R. L. Grimm, A. I. Frenkel and G. Li, *Journal of the American Chemical Society*, 2018, **140**, 16042-16047.
 114. R. Kuriki, C. S. K. Ranasinghe, Y. Yamazaki, A. Yamakata, O. Ishitani and K. Maeda, *The Journal of Physical Chemistry C*, 2018, **122**, 16795-16802.
 115. X. Wang, K. Maeda, X. Chen, K. Takanabe, K. Domen, Y. Hou, X. Fu and M. Antonietti, *Journal of the American Chemical Society*, 2009, **131**, 1680-1681.
 116. W. Yang, R. Godin, H. Kasap, B. Moss, Y. Dong, S. A. J. Hillman, L. Steier, E. Reisner and J. R. Durrant, *Journal of the American Chemical Society*, 2019, **141**, 11219-11229.
 117. Z. Song, Z. Li, L. Lin, Y. Zhang, T. Lin, L. Chen, Z. Cai, S. Lin, L. Guo, F. Fu and X. Wang, *Nanoscale*, 2017, **9**, 17737-17742.
 118. A. H. Castro Neto, F. Guinea, N. M. R. Peres, K. S. Novoselov and A. K. Geim, *Reviews of Modern Physics*, 2009, **81**, 109-162.
 119. A. A. Balandin, *Nature Materials*, 2011, **10**, 569-581.
 120. O. Akhavan and E. Ghaderi, *ACS Nano*, 2010, **4**, 5731-5736.
 121. D. Chen, H. Feng and J. Li, *Chemical Reviews*, 2012, **112**, 6027-6053.
 122. D. C. Marcano, D. V. Kosynkin, J. M. Berlin, A. Sinitskii, Z. Sun, A. Slesarev, L. B. Alemany, W. Lu and J. M. Tour, *ACS Nano*, 2010, **4**, 4806-4814.
 123. A. Bakandritsos, M. Pykal, P. Błoński, P. Jakubec, D. D. Chronopoulos, K. Poláková, V. Georgakilas, K. Čépe, O. Tomanec, V. Ranc, A. B. Bourlinos, R. Zbořil and M. Otyepka, *ACS Nano*, 2017, **11**, 2982-2991.
 124. D. Mosconi, M. Blanco, T. Gatti, L. Calvillo, M. Otyepka, A. Bakandritsos, E. Menna, S. Agnoli and G. Granozzi, *Carbon*, 2019, **143**, 318-328.
 125. M. Blanco, D. Mosconi, M. Otyepka, M. Medved', A. Bakandritsos, S. Agnoli and G. Granozzi, *Chemical Science*, 2019, **10**, 9438-9445.
 126. M. Blanco, D. Mosconi, C. Tubaro, A. Biffis, D. Badocco, P. Pastore, M. Otyepka, A. Bakandritsos, Z. Liu, W. Ren, S. Agnoli and G. Granozzi, *Green Chemistry*, 2019, **21**, 5238-5247.
 127. W. Henke, S. Kremer and D. Reinen, *Zeitschrift für anorganische und allgemeine Chemie*, 1982, **491**, 124-136.
 128. P. v. Leeuwen. and S. Keltie, *Catalysis Science & Technology*, 2016, **6**, 3647-3648.
 129. M. Blanco, P. Álvarez, C. Blanco, M. V. Jiménez, J. Fernández-Tornos, J. J. Pérez-Torrente, J. Blasco, G. Subías, V. Cuartero, L. A. Oro and R. Menéndez, *Carbon*, 2016, **96**, 66-74.
 130. J. Nieto, M. V. Jiménez, P. Álvarez, A. M. Pérez-Mas, Z. González, R. Pereira, B. Sánchez-Page, J. J. Pérez-Torrente, J. Blasco, G. Subias, M. a. Blanco and R. Menéndez, *ACS Applied Energy Materials*, 2019, **2**, 3283-3296.
 131. C. Freysoldt, P. Merz, M. Schmidt, S. Mohitkar, C. Felser, J. Neugebauer and M. Jansen, *Angewandte Chemie International Edition*, 2019, **58**, 1-1.
 132. C. G. Margarit, N. G. Asimow, C. Costentin and D. G. Nocera, *ACS Energy Letters*, 2019, 72-78.
 133. M. N. Jackson, S. Oh, C. J. Kaminsky, S. B. Chu, G. Zhang, J. T. Miller and Y.

-
- Surendranath, *Journal of the American Chemical Society*, 2018, **140**, 1004-1010.
134. G. Zhang, R. Zong, H.-W. Tseng and R. P. Thummel, *Inorganic Chemistry*, 2008, **47**, 990-998.
135. I.-S. H. Lee, E. H. Jeoung and M. M. Kreevoy, *Journal of the American Chemical Society*, 1997, **119**, 2722-2728.
136. S. Martha, A. Nashim and K. M. Parida, *Journal of Materials Chemistry A*, 2013, **1**, 7816-7824.